# MECHANICAL CHARACTERISTICS OF CONTINUOUS CARBON NANOTUBE AND CONTINUOUSLY REINFORCED CARBON NANOTUBE COMPOSITE

by

Yupeng Li

A dissertation submitted to the Faculty of the University of Delaware in partial fulfillment of the requirements for the degree of Doctor of Philosophy in Mechanical Engineering

Spring 2016

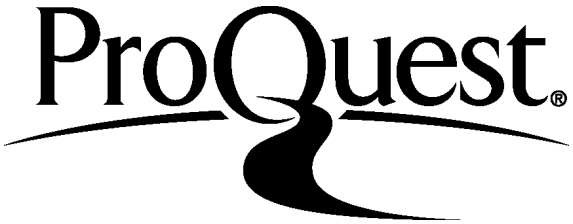

**MECHANICAL CHARACTERISTICS OF CONTINUOUS CARBON NANOTUBE AND CONTINUOUSLY REINFORCED CARBON NANOTUBE COMPOSITE**

by

Yupeng Li

Approved: _____
Suresh G. Advani, Ph.D.
Chair of the Department of Mechanical Engineering

Approved: _____
Babatunde A. Ogunnaike, Ph.D.
Dean of the College of Engineering

Approved: _____
Ann L. Ardis, Ph.D.
Senior Vice Provost for Graduate & Professional Education

I certify that I have read this dissertation and that in my opinion it meets the academic and professional standard required by the University as a dissertation for the degree of Doctor of Philosophy.

Signed: _____

Jonghwan Suhr, Ph.D.
Professor in charge of dissertation

I certify that I have read this dissertation and that in my opinion it meets the academic and professional standard required by the University as a dissertation for the degree of Doctor of Philosophy.

Signed: _____

Bingqing Wei, Ph.D.
Member of dissertation committee

I certify that I have read this dissertation and that in my opinion it meets the academic and professional standard required by the University as a dissertation for the degree of Doctor of Philosophy.

Signed: _____

Chaoying Ni, Ph.D.
Member of dissertation committee

I certify that I have read this dissertation and that in my opinion it meets the academic and professional standard required by the University as a dissertation for the degree of Doctor of Philosophy.

Signed: _____

Xin Lu, Ph.D.
Member of dissertation committee

## ACKNOWLEDGMENTS

I thank the National Science Foundation Award, the University of Delaware, and the Department of Mechanical Engineering for financial support.

I thank my advisors, Dr. Jonghwan Suhr and Dr. Bingqing Wei, for their instruction and guidance. They showed me the professional path to achieve academic success and trained me by scientific and precise research technique. Also, they gave me enough freedom on how to progress in the research work. All of these made my academic career developed comfortably and productively. Both Dr. Suhr and Dr. Wei have helped me in learning the skill of communication and their corrections in the papers and presentations have made me clear on the serious and strict research attitude. Dr. Suhr's morality and honesty in doing research have always guided me, while Dr. Wei's attitude of deep understanding the concept by exploring has always inspired me. With their help and instruction, I can develop my academic career and be able to research independently by myself.

I thank my dissertation committee, Dr. Chaoying Ni, and Dr. Xin Lu, for their support and contributions to this research and my graduate training. I thank the staff and members of the EML lab, especially Dr. Fei Deng for their time and effort in making available the microscopy images. And I thank all my group members for the discussion and support. I thank my parents for their selflessness, sacrifice and support through the years. They have been an inspiration to me in the past, right now and in the future.

## TABLE OF CONTENTS

Appendix

## LIST OF TABLES

## LIST OF FIGURES

## ABSTRACT

Due to the outstanding mechanical, thermal and electronic properties of carbon nanotubes (CNTs), CNT and CNT reinforced polymer composite are becoming more and more pervasive in engineering applications, especially in energy absorbing and damping materials. Therefore, the underlying mechanism of the intriguing mechanical properties of CNT arrays and CNT reinforced composites is an essential and fundamental science for the potential applications of CNT related materials.

It is fundamental and critical to investigate the mechanical properties of CNTs first, since the intrinsic properties and collective behavior of CNTs play an important role in the mechanical response of composite. The buckling behavior of vertically aligned carbon nanotubes (VACNT) was investigated. By taking van der Waals interactions into account, both experiments and modeling results confirm that VACNTs buckle in the bottom region with a high mode buckling, following wave damping effect. Then, the compressive behavior of VACNTs was quantified by strain energy density function. The effects of CNT structure/morphology, including diameter, cross section area, moment of inertia, defect degree and density, on mechanical properties were statistically investigated and compared with cellular materials, showing significant influence on determining the mechanical properties of VACNTs.

The focus of CNT polymer composites is on the application-oriented viscoelastic properties. The static viscoelastic characterization was conducted by creep and stress relaxation tests with stress/strain variation and quantified by nonlinear power-law model. The dynamic properties were characterized by dynamic mechanical analysis (DMA) with frequency variation. And CNTs show significant enhancement in elastic response and considerable influence on viscous response. In addition, the temperature effects were investigated and composites show better thermal stability. By using time-temperature superposition (TTS) and Williams–Landel–Ferry (WLF) fitting, the prediction scale of viscoelastic behavior in time/frequency range can be significant enlarged.

The viscoelastic responses are complicated by the intrinsic anisotropy of CNTs, so it is also essential to study their anisotropic properties. The compressive and viscoelastic characterization were performed on longitudinal, transverse and random composites and compared with PDMS. The results confirm the exceptional reinforcement of CNTs in longitudinal composites, which have lateral support from polymer matrix. And the increased damping effects of composites can be explained by the interfacial sliding and the energy dissipation between nanotubes and polymer matrix.

Furthermore, the fatigue tests of CNT polymer composites were performed to investigate mechanical robustness and long-term stability. From the stress-number of cycles (S-N) data in cyclic DMA tests, CNTs improved the fatigue life of composites

considerably, especially in high-cycle fatigue strength, caused by the hindering of crack propagation from CNTs, the interface debonding and the CNT reinforcement effects. Also, the microscopy images of fracture surfaces indicate different fatigue resistance and different fracture/crack mechanism between longitudinal and transverse composites.

# Chapter 1

# INTRODUCTION

## 1.1 General

Due to their unique structure and morphology [1, 2], carbon nanotubes (CNT) have been the most interesting and important novel material in various fields of research. Their unique structure allows superior electrical, mechanical and thermal properties [3]. After extensive investigations on this promising material, the remarkable physical and mechanical properties, such as unprecedented strength, resilience and low density, were reported widely, along with exceptional electrical and thermal properties.

The mechanical properties of individual carbon nanotubes have been characterized in both compression [4, 5] and tension [6], as well as the mechanical properties of polymer composites with addition of CNTs at low loadings [7-9]. The elastic modulus of CNT is found to be between 100 GPa and 1.3 TPa [10], which is comparable to that of diamond (~1.2TPa) [11]. The reported tensile strength of CNT ranges from 13 GPa to 150 GPa [10], which is shown to be much higher than that of high-strength steel (2 GPa). The outstanding resilience of CNT in sustaining large extent bending and deformation without damage is distinctively higher than classical metals and carbon fibers [11], showing a superlative ductility and recoverability. Furthermore, no fatigue failure of vertically aligned CNT (VACNT) was observed at high strain amplitudes up to half a million cycles [12]. In particular, the ‘soft tissue’ like viscoelastic behaviors of both CNT arrays and continuously reinforced CNT

polymer composites were also observed in earlier reports [13, 14]. The electric current carrying capability is estimated to be $1\times10^9$ amp/cm$^2$, whereas copper wires burn out at about $1\times10^6$ amp/cm$^2$. And their sharp tip structure makes them an ideal material for field emission [15]. The electrical resistance of VACNT arrays has been measured during compressive cyclic loadings, following the compressive strain responses in both longitudinal and transverse directions [16]. It was reported that the thermal conductivity of SWCNT is predicted to be 6000 W/mK at room temperature and SWCNTs are thermally stable up to 2800 ˚C and 750 ˚C, in vacuum and air, respectively [11].

With all the exciting properties mentioned above, it is conceivable that nanotubes will be an important material in future technology. Particularly, the viscoelastic property of CNTs and CNT polymeric composites shows strong potential of using such CNT architectures to build engineering nanostructures systems, such as energy storage devices, synthetic contact probes, cushions, tunable dampers, sensors and electromechanical devices in future applications [12, 17, 18]. Since the underlying intrinsic mechanical properties of CNTs and CNT reinforced composites is not fully understood, it is essential to investigate and understand the fundamental science of the mechanical characteristics of CNTs and CNT polymer composites. This knowledge will enable us to further fabricate and develop fundamentally new nanotube hierarchical structures so as to establish novel solutions to ultimately create nanotube based artificial engineering material.

## 1.2 Carbon Nanotubes

CNTs were first discovered by Iijima in 1991 [1]. They belong to the family of fullerenes and have the carbon structure formed by imagining expanding the famous fullerenes structure C60 in Figure 1.1a, which consists of 60 carbon atoms all linked together to form a hollow spherical ball structure.

According to the structure of CNTs, there are two main types available today, single-wall and multi-wall CNTs. A single-wall carbon nanotube (SWCNT) can be visualized as a hollow sealed cylinder formed by rolling a 2D sheet of carbon atoms arranged in a hexagonal form, shown in Figure 1.1b and Figure 1.2a. The diameter of the SWCNT has the range of several nanometer and length up to millimeters. A multiwall carbon nanotube (MWCNT) consists of concentric layers of cylinders around a common central hollow axil in Figure 1.1c and Figure 1.2b and the graphite layers have a 0.34nm interlayer distance. The outer diameter of MWCNTs ranges from 5nm to 30nm or more with several concentric layers [19].

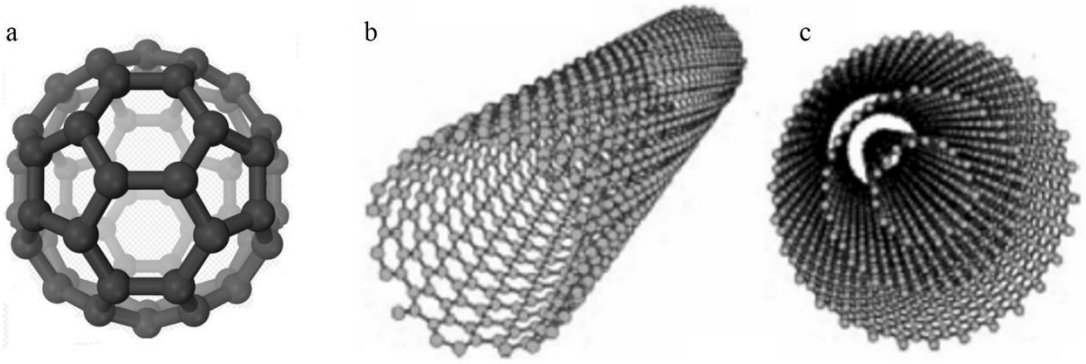


Figure 1.1 Schematic structure of fullerence molecule and CNTs. (a) Fullerene molecule, (b) Single-walled carbon nanotube and (c) Multi-walled carbon nanotube. [20]

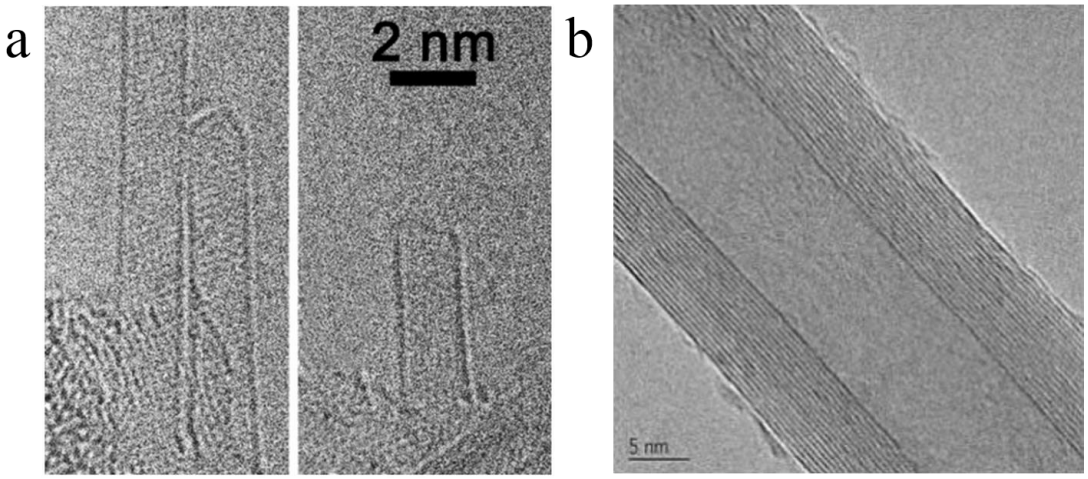

Figure 1.2 (a) High resolution TEM image of SWCNT bundle [21]. (b) High resolution TEM image of MWCNT, showing the graphite layers and concentric structure [22].

Carbon nanotubes can be fabricated in a variety of ways and the most common synthetic methods are based on arc-discharge method [19], laser ablation [23] and chemical vapor deposition (CVD) [24-26]. The arc-discharge is the catalyst-free method to have very straight structure and few defects and the laser ablation method can produce large scale of high purity CNTs, while the nanotubes made from CVD generally have very large quantities with relative cheap cost. So, the most common production method for MWCNT is undoubtedly chemical vapor deposition, considering the high volume and quantity of CNT production, though the CNTs have more defects and less purity.

Due to the graphitic layer structure, the mechanical properties of carbon nanotubes were expected to be analogical as graphite or superlative carbon source material. The elastic modulus of MWCNTs were first estimated by indirect measurement. For instants, the thermal vibration in TEM [27] measure shows the average value of 1.8 TPa and computational simulation calculated the elastic modulus of 1.5 TPa [28]. Direct measurement by atomic-force microscope (AFM) was

performed later gave an elastic modulus of 1.28 TPa for MWCNT and ~1 TPa for SWCNT [29]. The ultimate mechanical properties of CNTs were characterized on individual nanotube, however, the collective mechanical properties of CNT arrays show remarkable difference from individual nanotube and vary in wide range. For instance, Yu *et al.* [30, 31] were able to measure the tensile properties of CNT bundles and they found the modulus was 0.32 TPa~1 TPa because of intertube slippage. Salvetat *et al.* [32] measured the Young's modulus from 12 to 50 GPa of MWCNT due to high defect ratio. Also, compressive tests on the vertically aligned carbon nanotubes (VACNT) show much lower values of stiffness [4, 14, 33, 34] than the studies on individual nanotube, and there are reports with a wide range of elastic modulus of CNTs [10], as shown in Figure 1.3. So, the different structure/morphology of nanotubes, which are determined by fabrication conditions, could lead to the scattering mechanical properties of CNT and need further investigation.

Overall, the mechanical response of CNTs is critical and have dominated effects on the collective mechanical properties of CNT polymer composites. Therefore, before the study on CNT composite in terms of engineering application, it is indispensable and necessary to reveal and understand the mechanical properties of CNTs first, especially the collective behavior in nanotube arrays and the relationship between microstructure/morphology and the mechanical properties of CNT structures.

Experimental and theoretical results for nanotube axial Young's modulus

| Elastic modulus (TPa) | Method of measurement |
|---|---|
| *Experimental measurements* | |
| 1.26 (±20%) | TEM – thermal vibration of a beam [49] |
| 1.28 (±40%) | AFM – 1 end clamped [50] |
| 0.81 (±50%) | AFM – 2 ends clamped [51] |
| 0.1–1.0 (±30%) | TEM – electrostatic deflection [52] |
| 0.27–0.95 | Dual AFM cantilevers [53] |
| 0.91 (±20%) | TEM – direct tension [54] |
| | Method of calculation |
| *Theoretical calculations* | |
| 0.97 | Empirical lattice dynamics [45] |
| 1.0 (±15%) | *Ab initio* [47] |
| 1.05 (±5%) | Molecular structural mechanics [43] |
| 0.68 | Pin-jointed Truss model [55] |

Figure 1.3 Experimental and theoretical results for nanotube axial Young's modulus. [10]

## 1.3 Carbon Nanotube Composite

The preliminary research on CNTs reveals the outstanding mechanical properties of CNTs, including stiffness, strength and large aspect ratios, provides us the fundamental knowledge of the mechanical response of CNTs and consequently stimulates the development of nanotube-reinforce composites for both structural and functional applications, especially for their excellent strength and stiffness properties.

In general, the most common method for fabricating CNT polymer composites is based on solution processing. The process is divided into three stage: dispersing CNTs in either a solvent or polymer solution by agitation, mixing the nanotubes and polymer evenly, evaporation of the solvent to form composites [35]. And the critical issue of this method is the efficient dispersion of nanotubes in the relevant solvent, and

many studies reported the improvement of the dispersion by different solution [36-38]. Another fabrication method is melt process, which is suitable for insoluble polymer. The polymer is first melted into viscous liquid and the nanotubes will be dispersed into the melt by mixing. The bulk composites can be fabricated by specific mold then. The fabrication quality of composites is determined by optimization of the nanotube mixing degree [39]. If the polymer is insoluble and thermally unstable, the appropriate choice is the polymerization processing, which enable the grafting of polymer macromolecule onto the walls of CNTs through the mix of polymer solvent and nanotube directly. This method allows high nanotube loading and good miscibility with many polymer types, with the non-colvalent bonding between polymer and nanotube. Furthermore, the research on colvalent bonding between nanotubes and matrix was conducted by employing chemical functionalization of the CNTs and polymer grafting [40]. The covalent bonding provides an efficient improvement on mechanical properties due to the excellent interfacial stress transfer between nanotubes and polymer.

There are numerous studies on the mechanical properties of CNT reinforced polymer composites in the past decade. Shaffer *et al.* [41-43] were able to process CNT/polyvinyl-alcohol composite films with elastic modulus of 150 MPa and Qian *et al.* [42] characterized an increase in elastic modulus between 36~42% of MWNT/polystyrene composites. Tai *et al.* [44] have processed a CNT phenolic composites with enhancement in elastic modulus up to 50%. Ogasawara *et al.* [45] also reinforced a phenylethyl/MWCNT composites, and the resulting elastic modulus have around 10% increase with 3.3wt%, while strength reduced. Experiments [46] on

silicone-based elastomer reinforced with SWCNTs have also shown significant increase in elastic modulus and a reduction in strength.

However, due to the limited lengths of CNT and the random distribution, the enhancement effect on mechanical properties, such as stiffness and strength is far below what has been expected [47, 48]. Generally, the high strength structural composites require loads to be carried by continuous structure across the bulk dimensions and the stress should be distributed in the load direction, but the weak interaction in randomly discontinuous nanotube composites and the poor load transfer between short CNT and the matrix could be fundamental limiting factor in the CNT enhancement. So, it will be interesting and important to fabricate and characterize continuously reinforced CNT composites.

Recently, with the successful access to fabricating millimeter long CNTs, there are some studies on the mechanical properties of continuous CNTs and CNT polymeric composite in compression, such as the contact resistance of VACNT [49], the viscoelastic properties and fatigue resistance [12, 13], tribological properties [10], multifunctional VACNT brushes [50]. Especially, both nanotubes and nanotube reinforced composites exhibit nonlinear elasticity and viscoelasticity with hysteresis [13, 51]. The extraordinary soft-tissue like properties along with the outstanding fatigue resistance [12] suggest that properly engineered continuous CNT composite structures could mimic biological tissues. Although the preliminary research provides promising data, the underlying mechanism of such viscoelastic behavior is still unclear and there is no comprehensive and systematic investigation on the mechanical properties of the continuous CNT composites.

Thus, it is essential and crucial to investigate and understand the underlying compressive properties of CNT composites, especially viscoelastic properties. Note that the continuous CNT composite structures, like soft-tissue material have high anisotropic properties, which also requires further investigation. And the fatigue behavior of composites is another important factor for the mechanical robustness in terms of long time. So, with fully understanding of the mechanical properties of CNT reinforced composites, this research will establish the foundation for a new paradigm and contribute to the material innovation in engineering applications.

## 1.4 Research Motivation and Outline

Considering the above scopes for CNT and CNT composite research, several aspects of CNTs and CNT composites are proposed in this dissertation, right from CNT synthesis and CNT polymer fabrication to their mechanical and viscoelastic properties and to engineering applications.

The work is presented in five chapters as described below.

In chapter 2, the buckling behavior of CNT arrays in compression is considered along with the collective behavior of CNTs. Compressive behavior under different strain, interaction between nanotubes will be examined and comparison between experiments and finite element modeling will be analyzed.

In chapter 3, the structure/morphology-mechanical properties relationship is considered. The structural/morphological properties and mechanical properties will be characterized and the effects of structural/morphological properties on material constants will be statistically investigated by quantitative modeling.

In chapter 4, the viscoelastic property of CNT composites is considered. Static and dynamic viscoelastic properties of the CNT composite will be characterized in order to better understand the viscoelastic properties. Creep, stress relaxation and DMA test results will be quantitatively analyzed with viscoelastic models and temperature effects will also be considered.

In chapter 5, the anisotropy of CNT polymer composites is considered. The mechanical properties of longitudinal, transverse and random CNT composites and PDMS will be characterized and compared. And linear viscoelastic models will be used to analyze the viscoelastic material constants for different samples and compared by statistical analysis.

In chapter 6, the fatigue behavior of CNT composites is considered. The cyclic compression tests will be performed and the stress-number of cycles curves will be examined and analyzed according to the fatigue failure mechanism with fracture surface SEM images.

Lastly, concluding remarks and scopes for further improvements are discussed in chapter 7.

# Chapter 2

# BUCKLING BEHAVIOR OF VACNT ARRAYS

## 2.1 Background

With the outstanding fatigue, resilience and good damping effect, ultra long VACNTs and continuous CNT composites show promising potential as engineered nanotube architectures in future applications, such as artificial skin type materials, energy absorbing materials and aircraft or wind turbine coatings. In these applications, the CNT arrays deform and recover together under compression, so the collective compressive behavior of CNTs has influence in the compressive properties, and understanding of these collective compressive behavior becomes critically important.

There are numerous studies on the compressive properties of VACNTs, showing large amount of evidence on the buckling of VACNTs. It was firstly reported [12] that VACNT blocks exhibited a viscoelastic behavior similar to soft-tissue, and a sharp stiffness increase in critical densification strain along with local buckling of VACNTs. The compression of VACNT films [14] indicated that VACNTs exhibited foam-like viscoelastic behavior with local zigzag buckling waves and strong resilience. Similarly, local periodic buckling regions and stiffness of VACNTs under nano-indentation were reported [52] in a low-cyclic compression. Also, local buckling behavior in the bottom region of VACNT turf [53] and VACNT arrays [33, 54] with many short buckling waves were observed in compression. The periodic buckling waves were observed during electrical conductivity characterization of a VACNT block [16]. And the stress-strain curve analysis of dense VACNT brushes also

indicates progressive propagating buckling behavior [55]. Moreover, an in situ compression test [34] revealed the progressive propagation of periodic buckling of VACNT bundles from bottom to top, and another in situ compression experiment [56] also indicated the large scale structural buckling and collapse of long VACNTs.

These local buckling behaviors of VACNT were observed in many experiments and could have huge influence on compressive properties. So, it is necessary and fundamental to understand this unique local buckling behavior. Most researches [14, 33, 34, 53, 55-58] have employed the classical Euler's column buckling model [59] with the formula: $P = \frac{\pi^2 EI}{4L^2}$, to give the prediction of buckling. Moreover, there are analytical models [60-63], numerical simulations [57, 64], and experimental studies [65-67] on buckling and post-buckling behavior of individual CNT under an axial compression.

However, the observed local buckling behavior is different from classical Euler column buckling, because the compressive behavior of VACNT arrays is collective behavior and the interactions among nanotubes could influence significantly on the buckling response. The van der Waals interaction within bundles cannot be ignored due to the small distance between them, and will lead to a collective CNT buckling rather than an individual buckling. Due to the van der Waals interactions, CNTs are constrained to some extent in the radial direction along the length, which can be considered as lateral support. Consequently, VACNTs have lateral support effects from neighboring nanotubes and the buckling behavior may be different from individual Euler column buckling. Therefore, the van der Waals interactions between neighboring VACNTs cause CNT buckles collectively as bundles and give rise to local buckling waves. There are many studies on the van der Waals interactions

between parallel [68-70], cross linked [71] CNTs, and the interaction potential between CNTs [72], but no detailed studies have been reported on the effects of the van der Waals interactions on the collective buckling behavior of VACNTs.

Thus, we have investigated and unraveled the buckling response of VACNTs with the van der Waals interactions as lateral supports by coupling experiments and modeling in first step. This study is the first time to interpret the unique local buckling behavior of VACNTs by considering van der Waals interaction and to understand the propagation of local buckling with a wave damping effect.

## 2.2 Material and Methods

### 2.2.1 Structural and morphological characterization of VACNT arrays

The microstructure and morphology of the VACNT arrays were characterized by scanning electron microscope (SEM) (Auriga 60) and transmission electron microscope (TEM) (JEOL 2010). The CNT alignment and distribution were obtained through SEM characterization on large CNT bundles, and the intrinsic structure of individual CNT was obtained through high resolution TEM images. To have further information on the defect degree of the VACNTs, which would undoubtedly affect the mechanical properties, the Raman spectroscopy with 633nm excitation was employed.

### 2.2.2 Uniaxial compression

To study the buckling response of CNT at higher aspect ratios, uniform compression test was performed using ElectroPuls E3000 Instron machine. Since the VACNTs were grown on silicon substrate, the nanotube sample together with the substrate was placed in bottom compressive fixture, having the substrate contact

firmly with the bottom surface in the fixture. Compressive strains were applied along the axial direction of the VACNT samples under displacements control. Note the resolution of the Instron for displacement is 1 μm. All the tests were performed with quasi-static loading rate of 100 μm/min and the applied strain increased step by step from 4.7% to 80%. For each strain step, the actuator kept the strain for 1 min and then released the strain, allowing the specimen to recover. The compressed VACNT arrays after recovery were monitored through SEM characterization and the buckling region was imaged for each strain step, respectively.

### 2.2.3 Van der Waals interaction between VACNTs

In order to investigate the VACNTs compression behavior, the van der Waals force between VACNTs has to be considered first. To model van der Waals interaction, the Lennard-Jones pair potential [73] is adopted as:

$$\varphi_{LJ} = -\frac{A}{d^6} + \frac{B}{d^{12}} \tag{2.10}$$

where d is the distance between the interacting atoms, A and B are attractive and repulsive constant.

The van der Waals force between two carbon atoms is derived from the above potential [68]:

$$F(d) = -\frac{\partial V_{LJ}}{\partial d} = \pi^2\sigma^2\sqrt{R}\left(\frac{35A}{64d^{4.5}} - \frac{46189B}{131072d^{10.5}}\right) \tag{2.11}$$

The positive value represents attractive force, while the negative value represents repulsive force.

As only the infinitesimal buckling of VACNT is considered, the force can be estimated by the Taylor expansion to the first and second terms, the higher terms can be neglected due to high order infinitesimal [68]:

$$F(d) \approx F(d_0) + \frac{\partial F(d_0)}{\partial d}(d - d_0)$$
$$= \pi^2\sigma^2\sqrt{R}\left(\frac{35A}{64d_0^{4.5}} - \frac{46189B}{131072d_0^{10.5}}\right) + \pi^2\sigma^2\sqrt{R}\left(\frac{315A}{128d_0^{5.5}} - \frac{969969B}{262144d_0^{11.5}}\right)(d - d_0) \quad (2.12)$$

Thus, the equivalent spring constant per unit length is:

$$K = \pi^2\sigma^2\sqrt{R}\left(\frac{315A}{128d_0^{5.5}} - \frac{969969B}{262144d_0^{11.5}}\right) \quad (2.13)$$

The parameters are taken as A=15evÅ$^6$ B=25000evÅ$^{12}$. To calculate the buckling response of VACNTs with van der Waals interaction, the equivalent spring constant is used to represent van der Waals lateral support. In Figure 2.1, the normalized equivalent stiffness of van der Waals interaction between two CNTs decreases dramatically from 1 to almost zero as the distance between two CNT outer layers ranges from 2nm to 10nm. The mathematical results show that van der Waals interaction as lateral support is only effective when CNTs are very close to each other. Since the average distance between CNTs within bundle is around 2~3nm according to TEM characterization, the van der Waals interaction should be taken into account for buckling analysis.

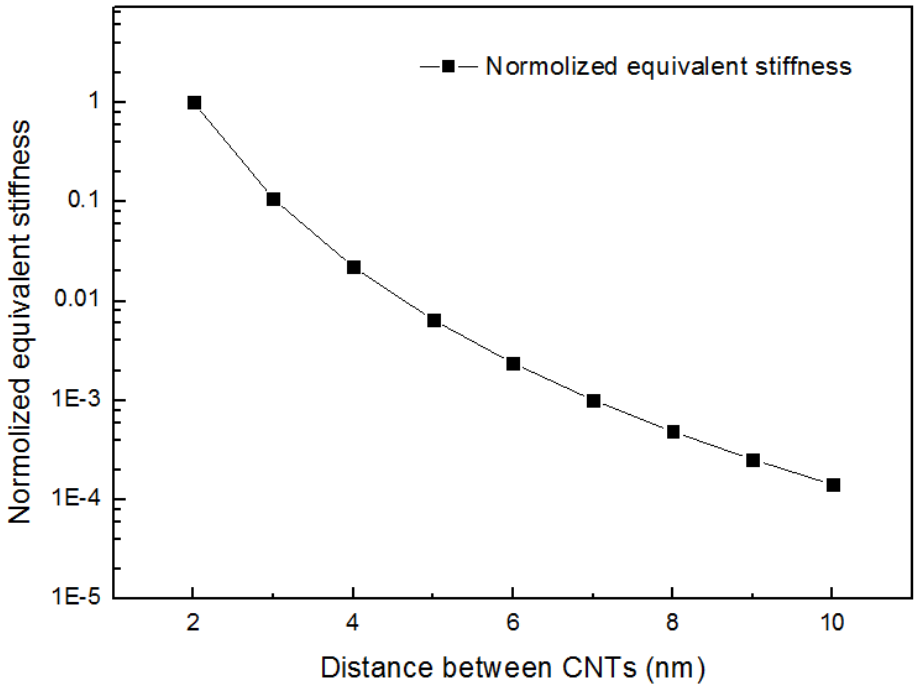


Figure 2.1 Normalized equivalent stiffness of van der Waals interaction verses the vertical distance between CNTs. The equivalent stiffness at 2nm is around 2.26MPa as standard equivalent stiffness.

### 2.2.4 Finite element modeling

In order to evaluate the buckling behavior of VACNTs with van der Waals interaction at high aspect ratio, a model was developed by using finite element (FE) method. The critical buckling stress and mode were computed first. Then, the FE results were processed and the VACNT deformation shapes were extracted to evaluate the buckling response of VACNTs with van der Waals interaction.

Finite element simulation was performed using the commercial finite element code ABAQUS (Dassault Systemes, 2009). To simplify FE model, the representative volume element (RVE) for VACNT arrays was employed. In this RVE approach, the VACNT array was assumed to be homogeneously distributed and dimensions of

VACNTs are uniform and the behaviors among VACNTs are identical due to geometrical symmetry. Lastly, the VACNTs contain the periodic unit cell in radial directions. The van der Waals interactions between VACNTs are represented by the surrounding medium support and only surrounding VACNTs within two nearest layers (5nm) were taken into account because of negligible van der Waals force in further distance according to section 2.2.3. With all of these assumptions, a VACNT with surrounding supportive medium model was developed with properly applied boundary and interfacial conditions. The individual VACNT is assumed to have a unique cross-section and has perfect bond to the surrounding medium. The VACNT is assumed to be 0.63mm in length, 7nm in outer diameter and 5nm in inner diameter according to the TEM observation. The dimension of medium is 0.12*0.12*0.63mm with the VACNT in the center, so the VACNT can be considered to have infinite medium support due to large ratio between medium dimension and VACNT diameter, which is consistent with the assumption in lateral support model [74]. The material properties are taken as $E_{CNT}$=400GPa, v=0.3 [10].

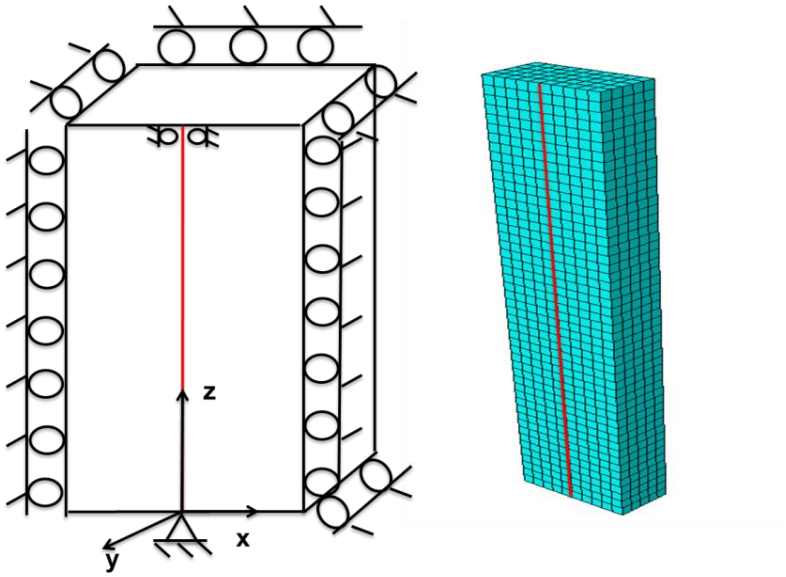


Figure 2.2 Schematic of boundary conditions and mesh of VACNT model with medium support in mid-cut view.

To be consistent with experiments, the VACNT in FE model is hinged in the bottom due to adhesive contact with substrate and constrained in radial direction at the top; all surrounding medium surfaces are fixed in radial directions because of geometrical symmetry. The rest parts of FE model are free. The load is compressive concentrated force applied on the top point of VACNT. In this model, 3D 2-node beam elements were used for VACNT, 3D 8-node hexagon elements were used for support medium. In order to save computational resource, the VACNT is meshed with 200 elements, the supporting medium part is meshed with 200 elements in longitudinal direction and with around 240 elements in cross-section to ensure the continuity and avoid large aspect ratio elements. The analysis method is linear buckling method, which can calculate the critical buckling stress, mode and the deformation shape of the VACNT.

## 2.3 Result and Discussions

### 2.3.1 Structural and morphological properties of VACNT arrays

Figure 2.3 shows structural and morphological characterization results of commercial available VACNTs. The CVD grown MWCNTs are vertically aligned and have a uniform length around 0.63mm. Figure 2.3a confirms the vertically aligned distribution of MWCNTs. The MWCNTs are aggregated together as bundles (Figure 2.3b-c) and have several nanometers average distance between adjacent CNTs (Figure 2.3d), indicating the CNTs are very close to each other within bundles and the effect of van der Waals interactions between them could be critical during compression. The outer diameter of these MWCNTs ranges from 7nm to 10nm, while the inner diameter ranges from 5nm to 8nm, and the number of graphitic layers of each nanotube is found to be around 3 (Figure 2.3d). The aspect ratio of VACNTs is estimated to be nearly $6 \times 10^4$, which is extremely high. The characterization results provide clearly the nanostructural and morphological features of VACNTs for experiments and modeling.

To have further information on the defect degree of the VACNTs, which could also affect the stability and buckling behavior of CNTs, Raman spectroscopy with 633nm excitation was employed. We conducted the Raman spectroscopy measurement with 5 different VACNT samples and different characterization positions along longitudinal direction of each sample. The Raman spectrum shows D-, G-, and 2D band at 1323.5 cm-1, 1594.1 cm-1, and 2638.1 cm¬-1 in Figure 2.4, respectively. In the Raman spectra of VACNTs, the average ratio of $I_D/I_G$ peaks is around 0.78 before compression and 0.77 after compression and the standard deviation is less than 5%, indicating that the intrinsic properties of VACNTs do not change much during the compression process. The Raman spectrum result indicates the

existence of disorder and defects in the graphitic structure of the VACNTs [75], which could lead to relatively weak resistance to an applied force and contributes to the instability of CNTs and propagation of buckling behavior during compression process.

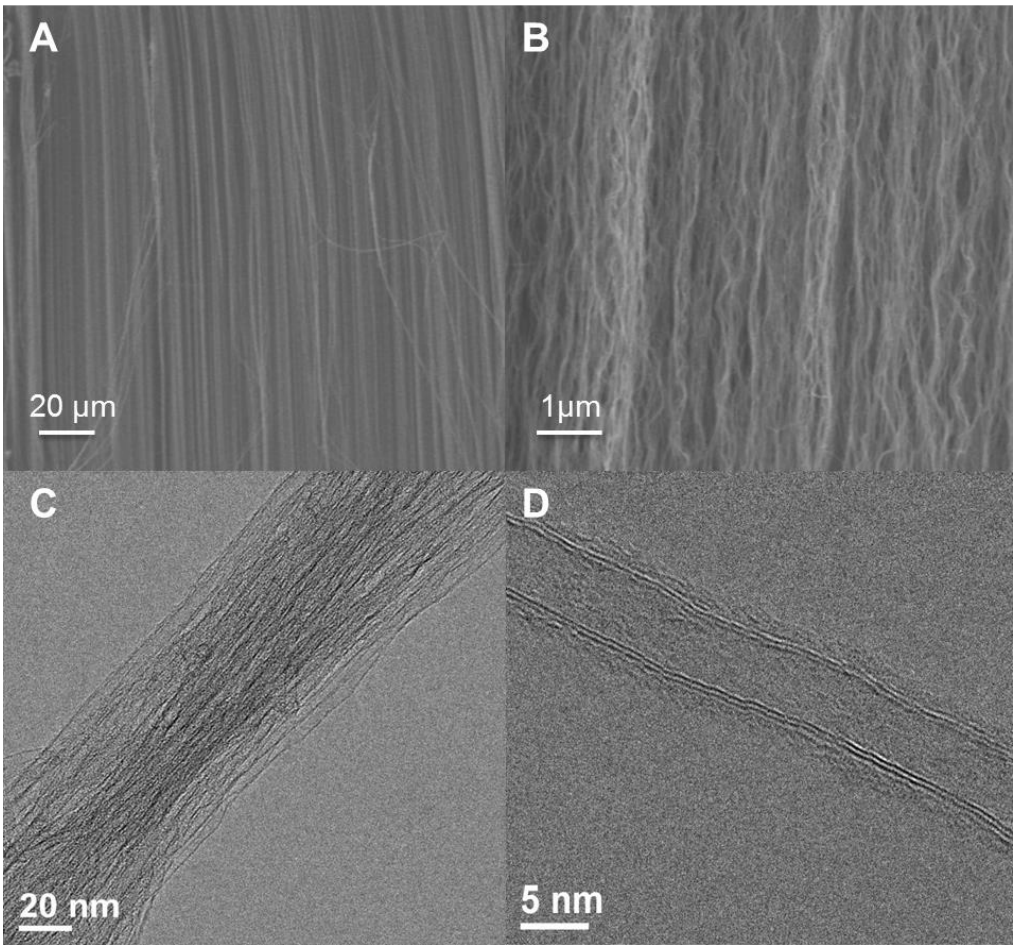


Figure 2.3 Structural and morphological characterization of VACNTs. (a). SEM image of VACNT arrays before testing, showing the nanotube's vertically aligned distribution. (b). SEM image of VACNT bundles, showing that the VACNTs are aggregated together as bundles and have an alignment distribution in the longitudinal direction. (c). TEM image of VACNTs with higher magnification, showing that the VACNTs within one bundle almost contact with adjacent nanotubes. (d). TEM image of the structure of an individual MWCNT, showing that the outer diameter is ~7nm, inner diameter is ~5nm, and number of graphitic layer is ~3.

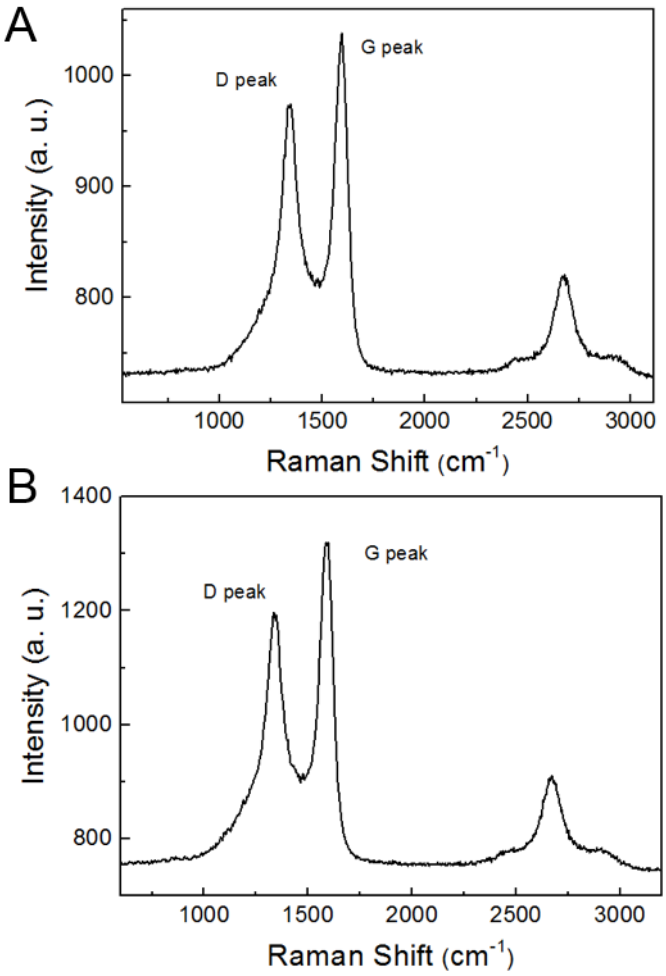


Figure 2.4 Raman spectrum characterization of VACNTs (633 nm laser excitation wavelength). (a). Representative Raman spectrum of VACNTs before compression. (b). Representative Raman spectrum of VACNTs after compression.

### 2.3.2 Buckling behavior of VACNT arrays in compression

With all necessary structural and morphological properties of VACNTs, we utilized a strain increase compression test to investigate the buckling behavior of

VACNTs. The SEM images in Figure 2.5 indicate that the VACNTs exhibit local buckling behavior which develops progressively as strain increases. Note that the buckling behavior develops from the bottom of the VACNT arrays. It could be attributed to the unbalanced friction between the bottom of the VACNTs and the silicon substrate, leading to a higher instability of VACNTs and also the smaller diameter of CNT in the bottom as the effective catalyst size get shrunk in diffusing process to substrate [76]. As seen in Figure 2.5a~d, the buckling waves develop progressively upward with new waves propagating above the buckled region as strain increases. Interestingly, the wavelength of the new buckling waves appears to be constant with the old ones. This buckling propagation and developing mechanism has not been studied in detail yet. And it could be explained in accordance with a wave damping effect [59], which was observed in previous experiments and modeling results, especially in a shell buckling [77-81]. Generally, a cylinder shell under a uniform axial compression will have many axis-symmetrical buckling waves in longitudinal direction due to surrounding constrain force from its continuous shell structure, and the amplitudes of buckling waves will gradually decrease upwards, eventually go to zero. Due to the van der Waals interactions from neighboring nanotubes, CNTs are constrained in the radial direction along length and consequently have lateral support effect. Very important analogous to the shell buckling, the VACNT buckling with van der Waals lateral support also have many short buckling waves, which represents a high mode buckling, and the amplitudes of buckling waves will decrease gradually under the wave damping effect. The detailed buckling propagation and developing process are shown in the representative stress-strain curve in Figure 2.5f with corresponding buckling conditions in each strain level (Figure

2.5a~d). The stress-strain curve can be divided into widely reported three-regions according to the buckling developing process: elastic region (0~5%), plateau region (5~60%), and densification region (70~85%). When strain is in the elastic region (<~5%), the CNTs have only elastic deformation and there are no buckled waves. When the strain increases and exceeds the critical buckling strain, the buckling waves start to propagate from the bottom and the elastic modulus decreases correspondingly, indicating the critical buckling condition in Figure 2.5a. With buckling developing, the bottom parts of CNTs deflect rapidly and then CNTs buckle at the first crests of the half buckling wave nearest to the bottom substrate. After the first half-wave is deformed, the second buckling half-wave sequentially begins to grow rapidly and so on. In this way, the buckling waves will progressively develop one by one upwards with the strain increase, shown in Figure 2.5b~d, and the stress strain curve shows almost a constant elastic modulus since it only needs a little more stress to force new buckling waves during this bucking propagation process. Among these buckling waves, the half-wave lengths are almost identical because the initial buckling conditions, such as CNT structure and Young's modulus, aspect ratio, and van der Waals interaction, have determined the length of all waves under critical buckling condition. Meanwhile, the amplitudes of buckling waves will gradually decrease down to zero upwards in the buckling region and the rest parts of CNTs will still retain straight, following the wave damping effect.

In Figure 2.5f, when the strain is in densification region (>~70%), elastic modulus will increase dramatically because the buckled nanotubes become tightly packed and folded, and their density increases significantly. Figure 2.5e gives the corresponding buckling response in the densification region, showing almost uniform

buckling half-waves along the longitudinal direction, which covers more than half length of VACNTs. The gradually decreasing amplitudes in the top waves and the periodic developed half waves in the middle and bottom regions follow wave damping effect when strain keeps increasing up to a higher level. The observed half-wave lengths from SEM images are around 9 μm at the top and middle region, and 6~8 μm at the bottom region. This slight increase in wavelength indicates that the waves are heavily folded at the bottom and have weak recovery when the applied force is released. The difference in wavelength between the top and bottom region is also reported in Cao et al.'s work [14]. Overall, at a large strain, the decrease of the buckling wave amplitudes and the periodic propagating waves still follow the wave damping effect.

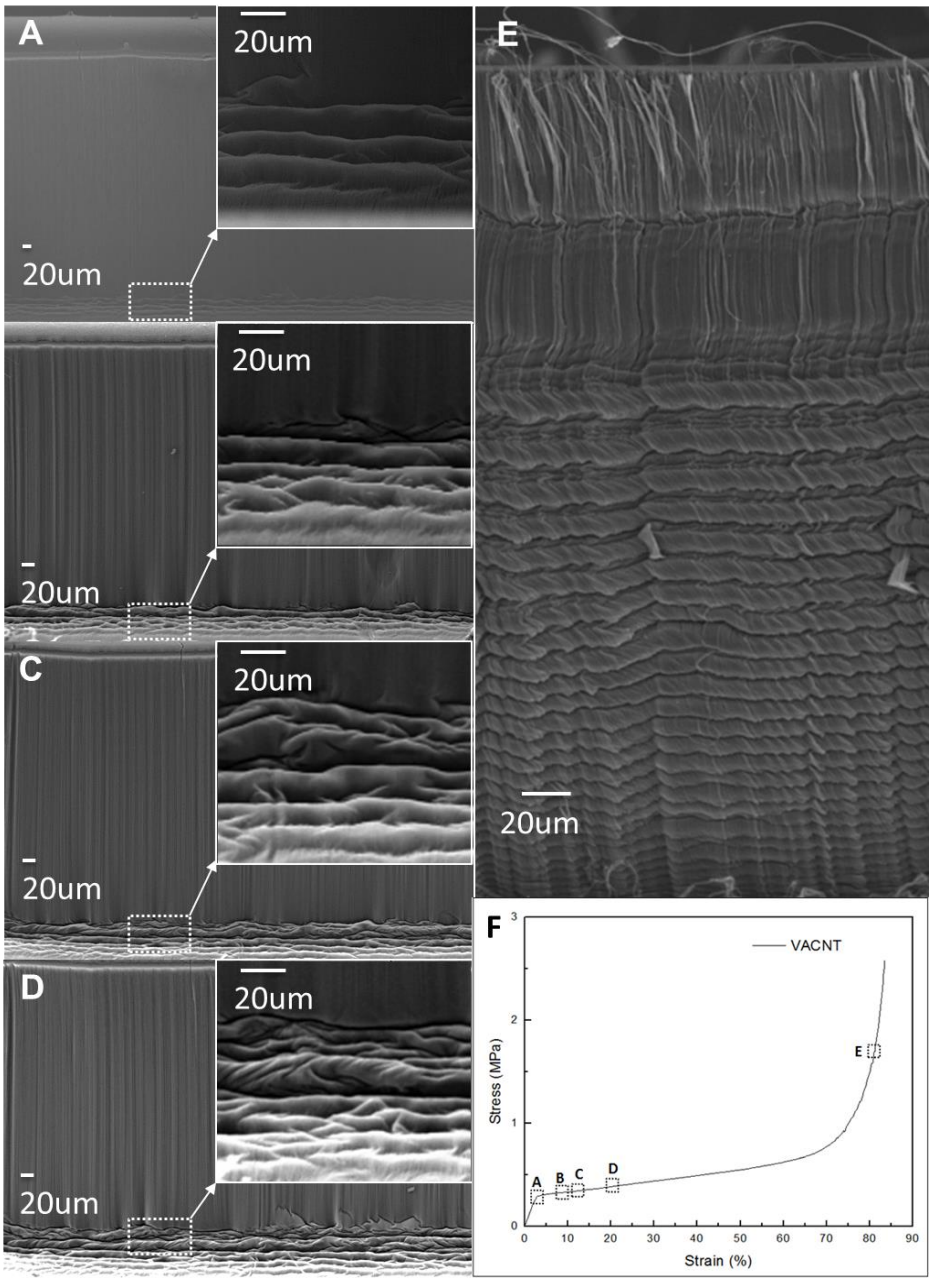


Figure 2.5 SEM characterization of VACNT buckling response in compression. (a-d). SEM images of VACNT arrays after compression in the strain range from 4.7% to 20%. (a.4.7%, b. 9.5%, c. 12.6%, and d. 20%). All VACNTs show the local buckling waves in the bottom region. The local buckling waves developed upwards as strain increase. (e). SEM of buckling waves of VACNTs under large strain ~80%, showing large buckled region over the nanotubes. (f). Representative stress-strain curve of VACNT under compression with corresponding buckling condition of a~e, respectively.

### 2.3.3 Van der Waals interaction modeling between CNTs

In order to explain the high mode buckling behavior of VACNTs observed in experiments, we developed analytical CNT models to take into account the van der Waals interaction between neighboring nanotubes, and then developed finite element model accordingly. For the CNT model, the interaction between inter-tubes within a MWCNT is neglected, which simplifies MWCNT to the equivalent CNT column. Therefore, the CNT is assumed to be a prismatic hollow continuous column with a ring cross-section. The van der Waals interaction between CNTs was modeled with the Lennard-Jones pair potential [73] and the interaction force between two parallel nanotubes [82] was deducted in 2.2.3:

With the supporting effect of van der Waals interaction, the corresponding lateral support is represented by converting the van der Waals interaction to elastic modulus of supporting medium accordingly [83]:

$$\sigma_{cr} = E_{CNT}(\frac{m\pi r}{L})^2/4 + \frac{K}{\pi}\cdot(\frac{L}{m\pi r})^2 \tag{2.14}$$

m is the number of half waves, L and r indicate length and radius of CNT, K is the equivalent spring constant, representing the van der Waals interaction between CNTs.

With the above equations, a finite element CNT buckling model with lateral support was developed by converting the van der Waals interaction into a supporting medium and the simulation results are shown in Figure 2.6. In Figure 2.6a, the critical buckling mode keeps 1st mode (whole column Euler buckling) when the aspect ratio is under ~60. After that, the critical buckling mode will become a high mode and the

mode number will gradually increase with aspect ratio. When the aspect ratio exceeds ~6000, the critical buckling mode starts to keep constant around 30th mode and the buckling region decreases from almost whole nanotube to nanotube ends. According to FEA analysis, with lateral support, the buckling mode of VACNTs will quickly increase to a high mode after the aspect ratio of 60 and have nearly proportional correlation with aspect ratio, but when the aspect ratio is over ~6000, the local buckling behavior occurs and buckling mode will start oscillate around number 30. Figure 2.6b shows simulation result of critical buckling condition of VACNT in experiment condition (aspect ratio of $6 \times 10^4$) with the van der Waals lateral support, where CNT buckles in the bottom region with many half waves (~30th buckling mode), indicating the observed buckling response in SEM images. The amplitudes of buckling waves are large in the bottom and gradually decrease to zero upwards, suggesting a wave damping effect. The half wave number of the FE result is around 15 at one end, which is higher than the experimental observation number 8. Among these half waves, the wave lengths are almost identical around 2.2 μm, while the experiment showed 6~8 μm. The differences between wave lengths and numbers might be caused by neglecting the multi-layer van der Waals interaction within the CNT, which could support the CNT considerably [84, 85]. Particularly, the CNTs in our experiments have only 2~3 graphitic-layer structure and will have great instability in compression, which might be overestimated in FE simulation due to its solid beam assumption. Also, the assumptions in the L-J potential and the converting between van der Waals interaction and stiffness of supporting medium may contribute to the difference between FE and experimental results. In addition, there might be some differences between the actual VACNT structural properties and the SEM&TEM characterization,

and the mechanical properties between FE simulation values and actual CNT properties. But both FE simulation and experimental observation indicate that high mode buckling behavior would happen in the bottom region of VACNTs with many short buckling waves. And the propagation and developing mechanism of such buckling behavior follow the wave damping effect.

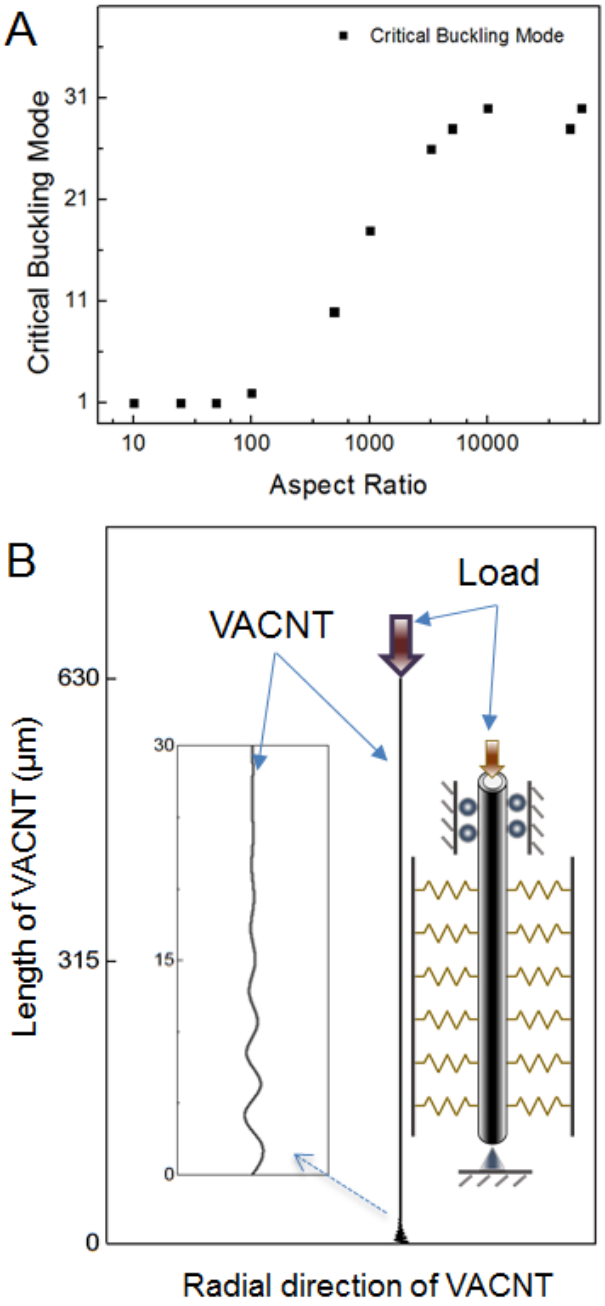


Figure 2.6 Critical buckling condition of VACNT by FE simulation. (a) Critical buckling mode dependence on aspect ratio. (b) The schematic of individual VACNT buckling with van der Waals interaction as lateral support at aspect ratio of $6\times10^4$, showing local buckling behavior like experimental observation with many short half waves in the bottom of the nanotube.

## 2.4 Conclusions

In summary, the unique buckling behavior of VACNT arrays under compression was characterized experimentally and interpreted properly by employing the van der Waals interaction between VACNTs as the lateral support. Since van der Waals interaction can constrain a VACNT in the radial direction, the buckling of VACNTs becomes a high mode buckling with many half buckling waves. The propagation and developing mechanism of VACNT buckling follow the wave damping effect. Furthermore, the study on such buckling behavior of VACNTs will significantly improve the understanding of collective mechanical properties of VACNT arrays and VACNT composites in compression, which could contribute to the use of engineered nanotube architectures in the building of synthetic biomaterials.

# Chapter 3

# COMPRESSIVE CHARACTERISTICS OF VACNT ARRAYS

## 3.1 Background

In chapter 2, compressive behavior of VACNT arrays was considered and investigated, especially the buckling behavior during compression was analyzed and interpreted by collective CNT response via van der Waals interaction. And it was possible to predict the CNT compressive behavior by buckling analysis and wave damping effect. However, considering the wide variation of nanotube structure and morphology, the intrinsic properties of CNT may be different and it is hard to determine the bulk material properties of VACNT arrays only using buckling analysis, so a more detailed and deep study on the structural and morphological effects on mechanical property of CNTs is necessary and interesting.

Recent studies have reported a wide range of mechanical properties. Under quasi-static monotonic compression, the VACNTs exhibit intriguing mechanical behaviours with almost full recovery from large strains [12, 86], while the other studies show the VACNTs will have permanent deformation in moderate strain condition [33, 52, 53, 56, 87]. Also, some nano-indentation compressive tests on the VACNT arrays show much lower values of stiffness [4, 33, 34, 86] than the studies on single CNT [88], and there seems to exist the reports with a wide range of elastic modulus of CNTs [10, 53, 89, 90]. Generally, the scatter of the mechanical properties of CNTs results from the inconsistent microstructure and morphologies, largely determined by a fabrication condition. The different CVD fabrication condition,

especially the fixed catalyst CVD and floating catalyst CVD methods could lead to considerable difference in nanotube properties [25, 91, 92], including the diameter and quality of individual CNTs [93, 94], as well as their bulk properties as forest, like alignment, waviness and density [54, 91]. Furthermore, it was reported that the CNT microstructure, such as diameter and the number of graphitic layers, has mainly determined the modulus and strength of CNT arrays [4, 16, 53, 86, 95]. And density and porosity would affect the modulus and strength to some extent [54, 96]. Also, the defect degree of nanotubes, which can be characterized by Raman spectroscopy [97, 98], can have an impact on the compressive properties. Therefore, the wide range of mechanical properties reported for VACNTs could be caused by their structural and morphological properties, which are determined by the growth method.

However, the quantitative analysis and modelling on the VACNT compressive properties are still lacking. More importantly, there still lacks a statistical dependence analysis on the relation between structural and morphological properties and the mechanical properties. So, in our study, ethylene/Al and ethylene/hydrogen was used as fixed catalyst CVD technique, while the xylene/ferrocene was used as floating CVD technique and the micro structure and bulk properties of fabricated VACNTs, such as diameter, cross section area, second moment of area and defect degree ($I_D/I_G$ ratio) and density, were characterized respectively. Then, the compressive stress-strain curves were obtain by quasi-static compression with a strain energy density function [99] to determine the material constants mathematically. Furthermore, a statistical analysis was used to study the relationship between the material constants and structure/morphology of the VACNT arrays. And the relationship was strengthen by some theoretical physical models and analogy to cellular material models.

## 3.2 Materials and Methods

### 3.2.1 Synthesis of VACNTs

The first kind of VACNTs were purchased from Nanostructured & Amorphous Materials, Inc., which are commercially available and synthesized with ethylene/Al CVD method [100]. It refers to 'E-CNT' (Ethylene based VACNT) in this study. We also used xylene/ferrocene CVD fabrication technique [12] to synthesize VACNT arrays, which is referred to 'X-CNT' (Xylene/ferrocene based VACNT). As shown in Figure 3.1, Ferrocene was used as the catalyst precursor and xylene was used as carbon source. A solution of xylene/ferrocene (0.06 g/mL) was injected into the CVD furnace by a syringe pump at a constant feeding rate of 0.6 mL/min. The reaction temperature was 850 ℃ with carrier gas, Argon/Hydrogen with rate of 800 sccm/150 sccm. The final thickness of VACNT in silicon substrate is about 1mm. After fabrication, the CNT blocks were peeled off from silicon substrate and cut into cubic shape by steel blade. Another VACNT arrays were fabricated with ethylene/hydrogen CVD growth method [54], referring to 'EH-CNT' (Ethylene/hydrogen based VACNT). The carbon source is ethylene and carrier gas is Argon. The gas flow rate is Ar:H2:C2H4 = 200:55:35 sccm. The Al/Fe was deposited on the SiO2/Si wafer with desire size and the CNT will grow above the Al/Fe catalyst. The reaction time is around 2h.

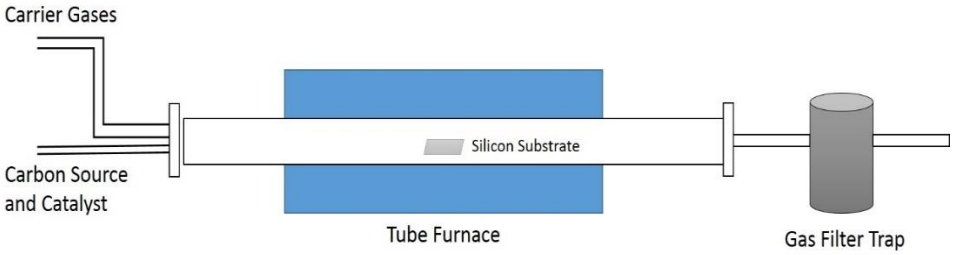


Figure 3.1 Schematic of Chemical Vapor Deposition (CVD) set-up for VACNT arrays fabrication.

### 3.2.2 Structural and morphological characterization

The microstructure and morphology of the three different kinds of the VACNT arrays were characterized by scanning electron microscope (SEM, Auriga 60) and transmission electron microscope (TEM, JEOL 2010), to get the outer/inner diameters of individual CNTs and the number of graphitic layers of CNTs statistically. The SEM and TEM images were took along the longitudinal direction of VACNTs. The average CNT diameters and number of layers were obtained with over 50 individual MWCNTs in different TEM images. And the cross section area and second moment of area were calculated by the average outer/inner diameters of nanotubes. SEM qualitatively illustrates the aligned distribution and morphology of VACNTs along the longitudinal CNT direction.

To have further information on the defect degree of the VACNTs, which would undoubtedly affect the mechanical properties, the Raman spectroscopy with 633nm excitation was employed on 5 VACNT samples for each type and 5 different characterization positions along longitudinal direction from top to bottom. The $I_D/I_G$ ratio has been used to correlate the structural purity of graphitic materials to the disordered graphite [97] by X-ray diffraction. The weight of VACNT blocks was measured by a micro-balance and then the volume was estimated through optical

microscope, determining the bulk density of each kind of CNT arrays. Also, for each CNT types, 6~8 VACNT blocks was measured in order to have the average bulk density.

### 3.2.3 Stress-strain characterization in quasi-static compressions

To study the stress-strain behaviors of VACNT arrays under compressions, quasi-static compressive testing was performed using Instron ElectroPuls E3000 machine at room temperature. A VACNT array in about 1mm × 1mm × 1mm cubic shape were mounted on the center of bottom compressive fixture and contacted firmly with the bottom fixture. Prior to testing, a pre-load was applied to the specimens to establish uniform contact condition between the VACNT specimens and fixture. This pre-load condition can ensure full contact between CNT blocks and fixtures and the validity and stability for further compression. Then, uniform compression was applied in longitudinal direction onto the samples up to a desirable strain using displacement control. All the tests were performed at loading rate of 100 μm/min in a quasi-static condition.

Then compressive stress-strain response was recorded only for the loading process and after the loading process, the compressive load will be released. Waiting around one hour for CNT recovery, a small pre-load was applied again and the plastic deformation of VACNTs can be obtained by the ratio between recovery length and original length of CNT arrays. For all stress-strain test, 6 to 8 VACNT samples were tested for each CNT type. The average elastic moduli from stress-strain response were obtained by the tangential modulus of linear curve fitting for stress-strain curves in initial region (0-5%), plateau region (~10-50%) and densification region (~75%-maximum applied strain). And the critical buckling strain and densification strain,

which divide three regions, can be determined by the intersection strain of linear fitting curves.

### 3.2.4 Strain energy density function modeling

In order to quantify the stress-strain response and determine material constants of the three kinds of VACNT arrays, strain energy density (SED) function modeling [99, 101-103] was employed to match with the experimentally obtained stress-strain responses. Since we conducted the longitudinal compression of VACNTs, we only consider the material constant in longitudinal direction in order to simplify our modelling. In compression, the transverse interaction between nanotubes is van der Waals force, which is order of magnitude lower than the resistant force of CNT in longitudinal direction. During compression, the deformation is mainly caused by the buckling of nanotubes in longitudinal direction and the transverse deformation of bulk CNT arrays is tiny and the bulk nanotube blocks can almost keep their original shape in our test and some previous studies [53, 95, 104]. So the transverse effects are assumed to be negligible in our model and the corresponding transverse material parameters in our strain energy density function are assumed to be zero. Among several models, we employed a modified SED developed by Attard et al [99], which was found to agree very well with our experimental results and also was known to work with a good stability under large strain conditions for a wide range of materials. In this model, the strain energy density is assumed to be decomposed into two components, $U_{incomp}$ and $U_{comp}$, which are associated with incompressibility of volume constant distortion, and compressibility or specific volume change, respectively.

Where $A_n$, $B_n$ and $\Lambda_n$ are material constants and can be derived from SED modeling by curve fitting to experimental data; r and s are termination points of the

summation; λi are the principal relative stretches in the orthogonal direction and J (=$\lambda_1$ $\lambda_2$ $\lambda_3$) is the relative ratio of volume change.

$$U = U_{incomp} + U_{comp} \tag{3.10}$$

$$U_{incomp} = \sum_{n=1}^{r} \left\{ \frac{A_n}{2n} (\lambda_1^{2n} + \lambda_2^{2n} + \lambda_3^{2n} - 3) + \frac{B_n}{2n} (\lambda_1^{-2n} + \lambda_2^{-2n} + \lambda_3^{-2n} - 3) \right\}$$
$$U_{comp} = \sum_{n=1}^{s} \frac{\Lambda_n}{2n} \ln(J)^{2n} - \sum_{n=1}^{r} (A_n - B_n) \ln(J) \tag{3.11}$$

If the material is considered to be Hookean at infinitesimal strain, the material constants are related to the shear modulus G, bulk modulus K and the Lam é constant Λ (corresponding to volume dilation) by

$$G = \sum_{n=1}^{r} \{n(A_n + B_n)\}, \Lambda = \Lambda_1, K = \Lambda_1 + \frac{2}{3} \sum_{n=1}^{r} \{n(A_n + B_n)\} \tag{3.12}$$

A seven parameter strain energy density function was used for the VACNT compressive experiments (r=3 and s=1) according to the level of nonlinearity in stress-strain curves. Statistical analyses (normal probability test and analysis of variance [ANOVA] tests) were performed in order to understand the dependence of the structural and morphological features on the mechanical properties.

## 3.3 Result and discussion

### 3.3.1 Structural and morphological characterization

Figure 3.2a-c show the characterization results of E-CNTs. The SEM characterization confirms the vertically aligned distribution of E-CNTs (Figure 3.2a) and the bundle of individual MWCNTs (Figure 3.2b). The outer diameter of these MWCNTs is 7nm ±1nm, while the inner diameter is 5nm ±1nm, and the number of graphitic layers of each nanotube is found to be range from 2 to 3 as seen in Figure 3.2c. According to Raman spectrum characterization, the average $I_D/I_G$ ratio of E-CNTs is 1.36 with 5.16% standard deviation, which indicates a higher defect degree of CNTs. And the average density of E-CNT samples is 0.039 g/cm$^3$. Figure 3.2d-f show the characterization results of EH-CNTs. The SEM images indicate the vertical alignment of EH-CNTs and the bundles with more waviness compared to E-CNTs. The outer and inner diameters of the nanotubes are 23nm ±2nm and 7nm ±1nm, respectively. The average number of graphitic layers of the nanotube is found to be around 22. The average $I_D/I_G$ ratio from the Raman spectrum analysis is characterized by around 1.23 with 2.2% standard deviation. And the average density of EH-CNT samples is 0.045 g/cm$^3$. Similar to other two VACNT arrays, the X-CNTs are also vertically aligned and bundled together (Figure 3.2g-i), while the neighbouring CNTs are closer to each other when compared to the others. It was observed that the outer diameter of the X-CNTs is 25nm ±2nm, while the inner diameter is 9 ±1nm. The number of graphitic layers of the X-CNTs is found to be around 20. Figure 3.2i can indicate that EH-CNTs and X-CNTs have a similar diameter and wall-thickness. The graphitic layers are nearly parallel to the tube axis leading to a formation of more straight, considering the outer layers with a slight rippling of EH-CNTs. For the $I_D/I_G$

ratio, the X-CNTs have a value of around 0.79 with 4.02% standard deviation, which is much less than the other two VACNTs indicating less defect degree with the X-CNTs. And the average density of X-CNT samples has the highest value of 0.056 $g/cm^3$. Overall, three different CVD methods result in significant difference among CNT micro and bulk properties, and as discussed later, these properties could play important roles in mechanical response of CNT array under compression.

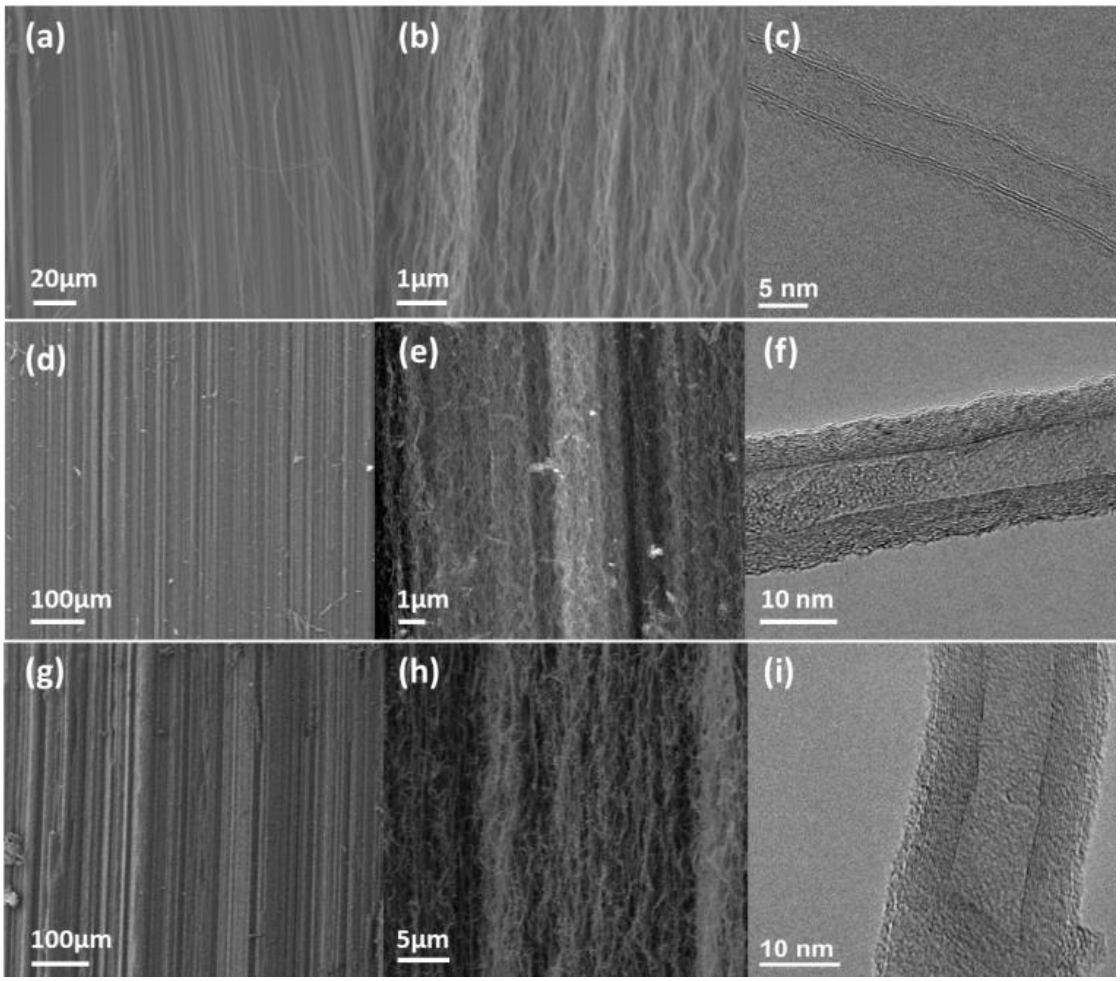


Figure 3.2 Structural and morphological characterization of the three different kinds of VACNT arrays from (a-c) E-CNTs, (d-f) EH-CNTs and (g-i) X-CNT. (a, b) SEM images of E-CNTs arrays before compression show vertically aligned distribution and CNT bundles with less waviness. (c) TEM image of E-CNTs. (d, e) SEM images of EH-CNT arrays before compression show vertically aligned distribution and dense waviness of CNTs in bundles. (f) TEM image of EH-CNTs. (g, h) SEM images of X-CNTs show alignment distribution and dense waviness along nanotubes. (i) TEM image of X-CNTs.

### 3.3.2 Stress-strain characterization in quasi-static compressions

Figure 3.3 compares the stress-strain behavior of the three different VACNT arrays in quasi-static compression. All VACNTs samples exhibit a typical stress-strain response, which can be divided into three distinct regions, displaying an initial elastic region (<5%) at low strain level, a plateau in the middle wide strain range (10~50%) with a reduced modulus, and a final densification region (>70%) with a drastic increase in elastic modulus in Figure 3.3b for E-CNT, just like the previous observation in section 2.3.2. This compressive stress-strain response is often observed in cellular or foam materials in compression.

Generally, in the elastic region (<~5%), only elastic deformation happens and there is no buckling of nanotubes. When the strain increases and exceeds the critical buckling strain, the bottom parts of CNTs deflect rapidly due to the instability and then CNTs buckle at the first crests of the half buckling wave nearest to the bottom substrate. With buckling developing, CNTs buckle at the top of buckled nanotubes and develop upwards gradually with applied loading. In this way, the buckling waves will progressively develop one by one upwards with the strain increase, as shown in Figure 3.3d for E-CNTs as an example of nanotube buckling process, the bottom of nanotubes have already buckled and deformed while the top nanotubes start to become buckle progressively. And there are many similar observations for the buckling propagation and developing of nanotubes during compression [53, 86, 91, 95, 104]. If the strain increases further, the new buckling wave will propagate above the old ones and the buckled region will grow up progressively. During this bucking propagation process, the stress strain curve shows almost a reduced elastic modulus since it only needs a little more stress to force new buckling waves. When the strain is in densification region (>~70%), elastic modulus will increase dramatically because the

buckled waves become tightly packed and heavily folded, and their density increases significantly. The behavior of CNTs was changed from buckling to packing and folding in this region. The right SEM image in Figure 3.3d gives the corresponding buckling response in the densification region, showing almost uniformly buckling half-waves along the longitudinal direction and the heavily folded nanotubes over half length of VACNTs. These heavily dense nanotubes will have much higher stiffness than plateau region.

The plastic deformation of the three kinds of VACNTs is shown in Figure 3.3c. The plastic deformation of E-CNTs is linearly dependent on strain and reaches up to 60% when strain is 60% and the EH-CNTs only have less than 1% plastic deformation in the same strain range, while the X-CNTs have moderate 20% plastic deformation after 80% strain. The difference in plastic deformation suggests the E-CNTs have much less resilience and recoverability as compared with X-CNT and EH-CNT. Considering the microstructure, such as small diameter and few number of graphitic layers (Figure 3.2c), the E-CNTs are expected to deform easily and to be hard to recover back, while the larger diameter and thicker wall-structure will help the EH-CNT and X-CNTs recover back from large strain compression. Theoretically, the larger bending stiffness of individual CNT within arrays could lead to better recovery response and resilience. The difference between X-CNT and EH-CNT might be the result of density, because higher density without enough porosity for deformation will lead to structural collapse during large strain compression and reduce recoverability of CNT forest.

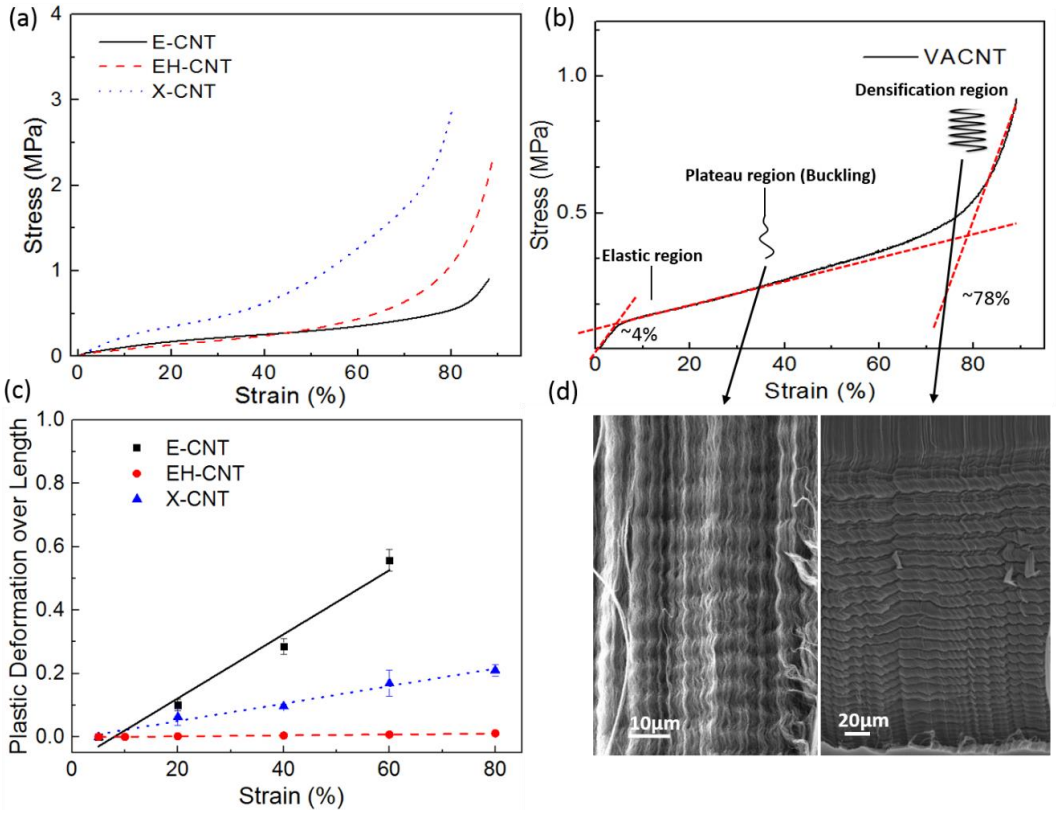


Figure 3.3 Compressive mechanical properties of the three different kinds of VACNT arrays (E-CNT, EH-CNT and X-CNT), including stress-strain response and plastic deformation. (a) Representative stress-strain curves of different VACNTs under compression with the strain range from 0% to ~90%. (b) Representative stress strain curve for three region with nanotube buckling propagation and developing. (c) Plastic deformation of three different kinds of VACNTs with strain range from 0% to ~80%, showing linear relation between the plastic deformation and strain. (d) SEM images for nanotube buckling behavior in plateau region (left) and densification region (right).

Table 3.1 Characterization results on stress-strain response of three different VACNTs, including critical buckling strain, critical densification strain and elastic moduli in three distinct regions with statistical analysis.

| Carbon Nanotubes | Critical Buckling Strain (%) | Critical Densification Strain (%) | Elastic Modulus in initial elastic region (MPa) | Elastic Modulus in plateau region (MPa) | Elastic Modulus in densification region (MPa) |
|---|---|---|---|---|---|
| E-CNTs | 4.33±0.97 | 78.36±4.34 | 6.06±1.23 | 0.43±0.04 | 7.56±1.65 |
| EH-CNTs | 3.47±0.57 | 74.62±3.01 | 0.59±0.07 | 0.52±0.05 | 17.41±1.51 |
| X-CNTs | 5.29±0.48 | 79.17±4.69 | 2.89±0.62 | 1.33±0.16 | 27.86±5.34 |

With the stress-strain curves as seen in Figure 3.3a and the three regions in Figure 3.3b, the critical buckling strain, the critical densification strain and the elastic moduli in three distinct regions of E-CNT, EH-CNT, and X-CNT are summarized in Table 3.1. The critical buckling strains of three VACNTs range from 3.47% to 5.29%, indicating a short initial elastic region of VACNT compression. In plateau region, the decrease in elastic modulus is observed, which is caused by the buckling behavior of nanotubes as described above, and the E-CNT and EH-CNTs have comparable value around 0.48MPa, while the X-CNTs have much higher value of 1.33MPa, suggesting that during buckling developing process, the CNT intrinsic structure and density could affect the collective buckling behavior of VACNTs. In the densification region, the critical densification strains of three VACNTs are relatively close to each other around the value of 76% and the mean moduli have the value of 7.56MPa, 17.41MPa and 27.68MPa, respectively, which is almost a linear increase between different nanotubes. Among them, X-CNTs show the highest elastic moduli than the other two, suggesting that strong individual CNT structure and high density may play a very

important role in large strain compression when nanotubes start to contact with each other and the behavior of CNTs changes from buckling to packing and folding.

### 3.3.3 Strain energy density function modeling characterization

The stress-strain response can successfully characterize the compressive behavior of VACNTs in three regions with their elastic moduli. However, it is still hard to compare and quantify the intrinsic material properties of VACNTs from their compressive response. So, in order to quantify the compressive behavior and determine material constants from stress-strain curves, SED function modeling was employed with the hyper-elastic constitutive equations in equation (3.12), and the mechanical properties were characterized by using least squares regression of the experimental data. The representative SED curve fitting is shown in Figure 3.4a. All fitting curves are consistent with the experimental data. Especially, in the plateau and densification region, the experimental data and the SED model prediction of all VACNTs have a good agreement with each other, indicating that the seven SED model can successfully quantify the stress-strain response of VACNT in compression.

The mechanical properties, which were derived from the SED model, include shear modulus, Lam é constant, and bulk modulus. The shear modulus in longitudinal direction ($G_{12}$ or $G_{13}$) of X-CNTs has the highest mean value of 1.1MPa, while the E-CNTs and EH-CNTs have mean value around 0.55MPa and 0.82MPa, respectively. It is found that shear modulus is also in quasi-linear increase and this is in consistency with the elastic modulus in densification region (Table 3.1), in terms of the relationship between elastic modulus and VACNTs category. The correlation coefficient between shear modulus and elastic modulus in densification region is over 0.99, showing that they are strongly related with each other. The similar behaviour

between shear and elastic modulus can be explained if we simply consider the general relationship of $G = \frac{E}{2(1+v)}$, which shows the proportional relation between shear and elastic modulus if the Poisson ratio is assumed to be a constant value. Therefore, the SED model shows that the shear properties of nanotubes during compression are similar as the elastic properties in densification region, and the dependence between these two factors might also be determined by the model itself, where the densification region could have significant influence on the sum of $A_n$ and $B_n$ and consequently on the shear modulus.

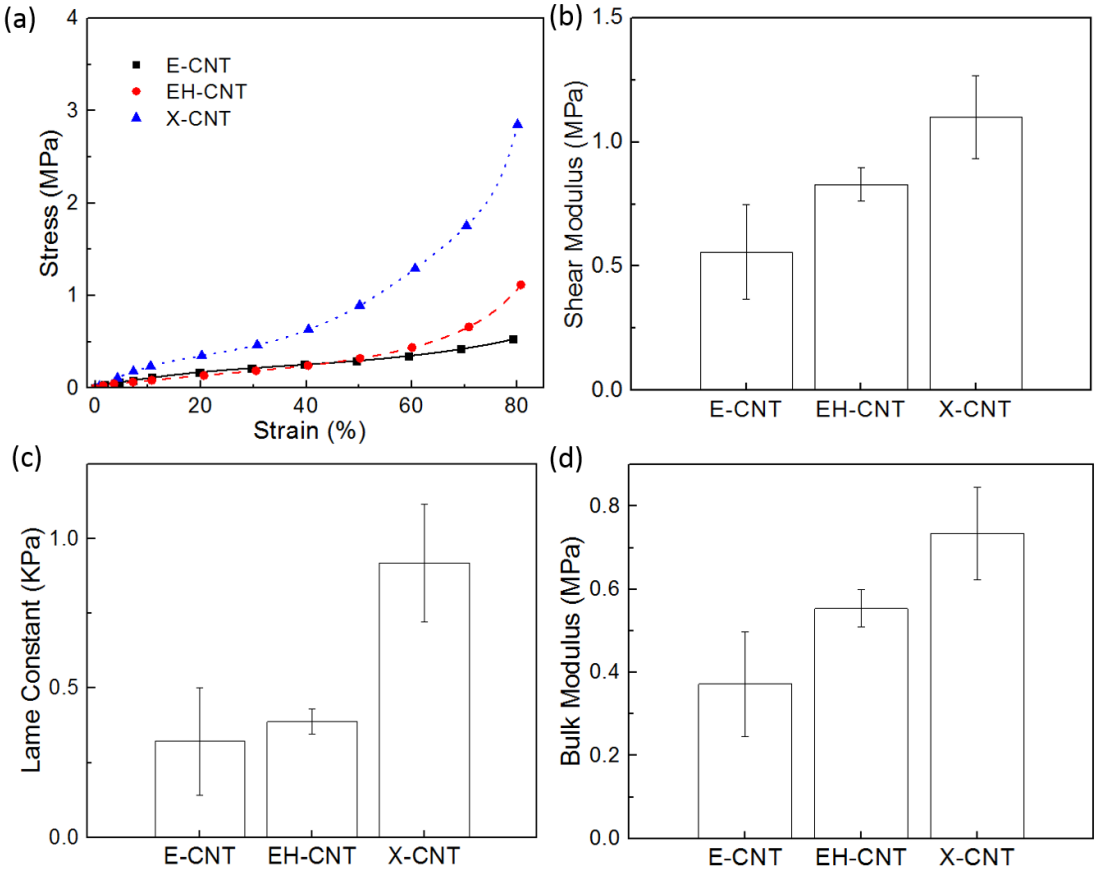


Figure 3.4 SED function characterization on stress-strain curves of the three different VACNT arrays. (a) The experimental data of the three kinds of VACNT arrays and corresponding fitting curves by SED function. (b) Shear modulus, (c) Lam é constant and (d) Bulk modulus of the three kinds of VACNTs by SED function modeling.

For Lamé constants, E-CNTs, EH-CNTs and X-CNTs have the value of 0.32KPa, 0.38KPa and 0.91KPa in Figure 3.4, respectively. All of the three VACNT arrays show very low value. Since the SED is modelled for the collective behaviour of CNT arrays, the Lamé constant is corresponding to the bulk volume dilation of CNT blocks. And the relative low value of Lamé constant indicates that the VACNT arrays are easily to shrink in volume and the resistance to compression is rather weak in our case. Physically, the volume shrink is related to the buckling of nanotube in longitudinal direction, where CNT arrays have a wide horizontal plateau region with buckling propagation and developing. In this region, it only need rather low stress to force nanotubes to buckle and therefore the volume of bulk CNT block will shrink significantly in longitudinal direction, leading to a low Lamé constant value. In terms of the value of Lamé constants and elastic modulus in plateau region, the statistical correlation result shows that they have almost the same tendency among CNT types with a correlation coefficient over 0.99, suggesting that the Lamé constants from SED model might have been determined by the elastic properties in the wide plateau region with nanotube buckling developing process. Among three VACNTs, the X-CNTs show much higher Lamé constant than the other two VACNTs, while the similar behavior was observed in plateau modulus in stress-strain curves, indicating that X-CNT samples have stronger resistance to applied load and are harder to buckle under compression. Since the absolute value of the Lamé constant is three orders of magnitude less than the value of shear modulus, the bulk modulus is dominated by the shear modulus according to equation (3.12) and has almost the same behavior as shear modulus. The X-CNTs has the highest bulk modulus of 0.73MPa, EH-CNT has the value of 0.55MPa, and E-CNTs has the value of 0.37MPa.

### 3.3.4 Structural and morphological properties effects on mechanical properties of VACNT arrays

In VACNT arrays, the structural and morphological properties are coupled together and vary simultaneously among different kinds of VACNTs. Consequently, the mechanical properties are affected by the co-effects of structural and morphological parameters. So, in order to investigate the relative importance and relative influence of different structural and morphological properties on mechanical properties, we employed the statistical analysis method, including linear dependent probability (p-value) and the correlation coefficient (corr). For individual CNT properties, we tested cross sectional area (A), which is related to the applied force (E*A) deforming CNTs, and the second moment of area (I), which is related to the bending moment of CNTs (E*I). And for bulk CNT properties, we tested bulk CNT density and defect degree ($I_D/I_G$). In this section, the relationship between these four parameters and material constants (shear modulus and Lamé constant) was tested by p-value and correlation coefficient method. Technically, statistical methods can help us find out the relative stronger correlation among these parameters, corresponding to the relative higher influence on mechanical properties.

From the statistical analysis in Figure 3.5, material constants such as shear modulus and Lamé constant were investigated by comparing with the effects of cross section, second moment of area, defect degree and density. Among the structural and morphological properties, density shows the most dependence with the shear modulus with minimum p-value of 0.108 and corr with the value of 0.986. Since the shear modulus are strongly related to the elastic modulus in densification region (Table 3.1), the similar statistical results between density and densification elastic modulus were obtained with p-value of 0.096 and a corr of 0.989. This statistical result suggests that

the density has more important influence on the mechanical behavior of VACNT arrays, especially in large strain condition. As discussed in Sec 3.3.2, the large increase in compressive elastic modulus of VACNT arrays can be related to the nanotube packing and folding behavior in densification region. In large strain condition, the collapse of the nanotube forest happens throughout the material and buckled nanotubes touch and press against one other as shown before in Figure 3.3d. When this happens, the stress-strain curve rises sharply and the corresponding E or G would simply be proportional to the relative density of bulk samples, if we assume the bulk elastic modulus is the collective response from each individual CNT by $E = \sum E_{CNT}$, just like a bundle of springs in parallel with stiffness $E_{CNT}$. If individual elastic modulus is assumed to be identical, the collective elastic modulus or shear modulus would be determined by the relative density by $E = \sum E_{CNT} \propto N \cdot E_{CNT} \propto \rho_*/\rho_{CNT} \propto \rho_*$.So, higher density will lead to more tight and compact packing of nanotubes, and the shear behavior and elastic behavior are dominated by nanotube density in the large strain range. This claim is also reported in honeycomb material study for the longitudinal direction compression [105] with the formula $\frac{E_3^*}{E_s} = \frac{\rho^*}{\rho_s}$ . And, the similar relation is also reported in cellular material experiments [106], local density and stiffness relation [104] and theoretical studies on CNT bundles within mats and fibers [96].

Note that, the second moment of area also has high dependent relation with shear modulus with p-value of 0.158 and high corr of 0.970. Compared with cross section area effects, the collective shear or elastic modulus are more affected by bending instead of elastic deformation in terms of individual CNT microstructure. And the correlation between CNT diameter and shear modulus is much less than the

moment of inertia (p value is 0.258 and corr is 0.918). This means the individual CNT properties associated with the bending stiffness could also play an important role in VACNT compression, especially in the large strain deformation. Physically, the deformation and buckling of CNT bundles are mainly based on the bending of individual CNTs within the bundles, so the moment of inertia (I) of the hollow nanotube is imperative to become an important influence factor, not only in the plateau buckling process but also in densification folding and packing process. Analogy with cellular material, the studies on foam material [105] also have the proportional relation between elastic modulus (E) and moment of inertia (I) $\frac{E^*}{E_s} \propto \frac{I}{l^4}$, where l is the average distance between fibres and can be considered as a density factor, which is consistent with our observation on the shear modulus and moment of inertia. There are studies stated the enhancement effect by CNT diameter increase [54] and the proportional relation between four power of diameter and stiffness [91], which could be an additional evidence for moment of inertia-shear/elastic modulus relation, as the moment of inertia  is determined by the four power of diameter.

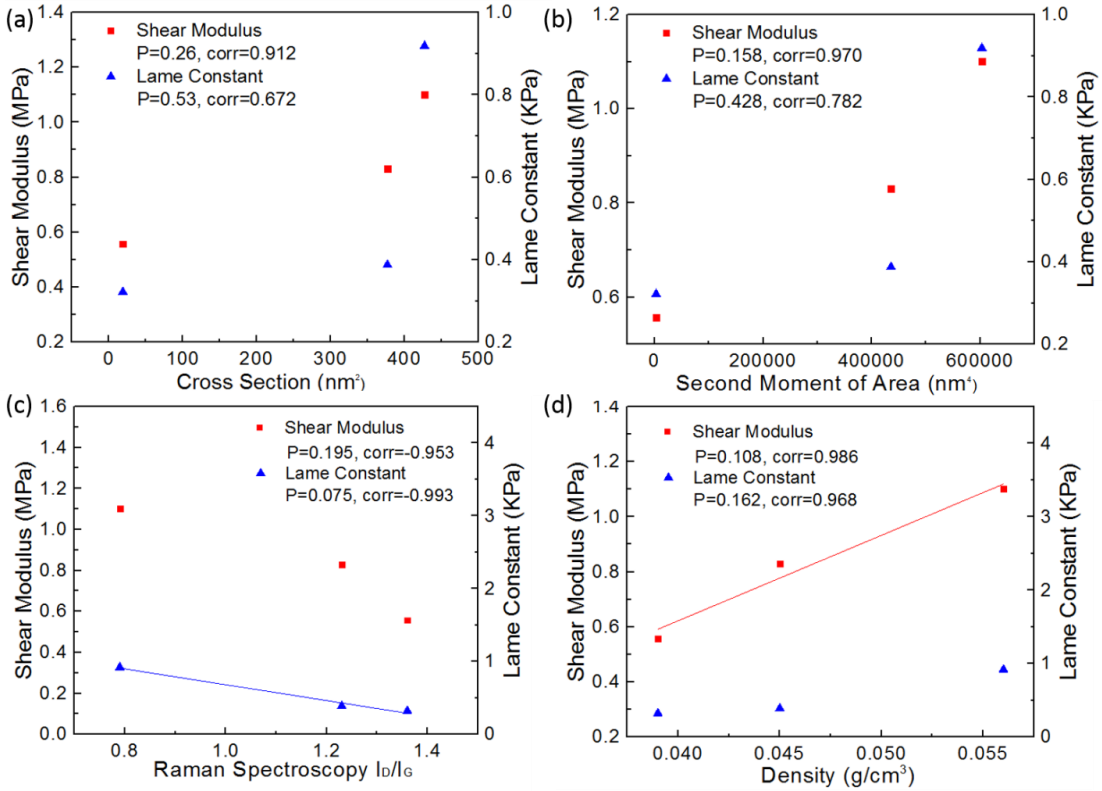


Figure 3.5 Statistical analysis on the relationship between mechanical properties and structural and morphological properties. The probability (p) and correlation coefficient (corr) between mechanical properties (shear modulus and Lamé constant) and (a) cross section, (b) second moment of area, (c) Raman spectroscopy $I_D/I_G$ and (d) density.

For the Lamé constant, it has the most dependent relation with $I_D/I_G$ for defect degree, with p-value of 0.075 and corr of -0.993 (negative relation), showing much higher dependent relation than all other factors. And the statistical results on plateau modulus (Table 3.1) are also affected most by defect ratio with p-value of 0.082 and corr of -0.992. Since the Lamé constant is related with volume shrink ratio in plateau region, the buckling and bending of the nanotubes become dominating factor in this process. The higher degree of crystalline order leads to a stronger nanotube wall-structure and better organized graphitic-layers, and may increase the actual elastic modulus (E) and the bending stiffness (E*I) of VACNT arrays, which is critical for

nanotube buckling and bending in plateau region. Physically, a higher stress is needed to deform the VACNT arrays with less defects and stronger nanotube-wall structure in longitudinal direction during the propagation of local buckling. In addition, previous studies on Raman spectrum of CNTs showed the corresponding correlation between wave shift and the stiffness of CNT structure [107, 108], indicating the microstructure change of nanotubes from stress-induced Raman band shifts. Meanwhile, the density still has considerable effects on the Lamé constant with the p-value of 0.162 and corr of 0.968, suggesting that the tighter and denser CNT arrays will also have a higher volume dilation ratio and elastic modulus. Like the densification region, the denser CNT arrays can provide more nanotubes and bigger contact cross-section area when buckling and deformation happen in plateau region, so it can have the similar proportional relation $E \propto \rho_* \; or \; \Lambda \propto \rho_*$ like shear modulus.

### 3.4 Conclusions

Through this study, the structural and morphological effects on mechanical properties of VACNT arrays under compression were characterized by our experiments and analyzed by employing the SED model and statistical method. The structure and morphology of different VACNTs were characterized. The stress-strain behavior of VACNT arrays has been quantified by hyper-elastic model. Subsequently, the material constants determined by both stress-strain curves and SED function were statistically compared and analyzed against structural and morphological properties. The statistical results show that the effects of structure and morphology of VACNTs on the mechanical properties are significant in compression. Among them, density, defect degree and moment of inertia have significant influence on the intrinsic mechanical properties of VACNTs and would determine the collective mechanical

response of VACNT arrays. More important, these findings elucidate the approach to improve and enhance the compressive mechanical properties of CNT and CNT-base materials, by controlling the structural and morphological properties.

# Chapter 4

# VISCOELASTIC CHARACTERISTICS OF CNT REINFORCED POLYMER COMPOSITE

## 4.1 Background

### 4.1.1 VACNT polymer composites

In the previous chapters, we investigated the collective mechanical behavior of CNT under compression and the bulk material constants of VACNT arrays. With the understanding of the collective compressive response of VACNT arrays, including local buckling behavior and compressive properties, we started research on nanotube-reinforce composites in this chapter, which can be utilized as biologically inspired artificial materials and soft tissue engineering applications, by taking advantage of the knowledge on compressive mechanical properties of CNTs in our previous studies.

The exploitation on CNT reinforced polymer composites have been extensively researched [10, 35, 107, 109-112] for their excellent strength and stiffness. It is believed that the nanotube could be an ideal reinforcement fiber material in composites due to the exceptional mechanical, electrical and thermal properties of CNTs [35, 110]. Over the past decades, some studies [35, 113, 114] on CNT-reinforced polymer composites have shown moderate improvement of mechanical properties, however, the reinforcing effect is still far from what has been expected. This is generally attributed to the length limitation and random distribution of CNTs [115]. Because the short length of nanotubes and weak van der Waals interactions

among the interfaces, the load transfer from the matrix to nanotubes could be significant hindered and the large-scale mechanical properties will be reduced inevitably.

Recently, the successful growth of VACNTs offers new opportunities for fabricating continuous nanotube reinforced composites by integrating CNT structures into polymer matrix. Some studies on the continuous VACNT polymer composites were carried out, and the reinforcement effect is impressive with significant increase in elastic modulus [13] as well as damping capability [116]. The study on composites with continuous CNT/CF show that CNT can improve not only the shear modulus and flexural rigidity, but also the energy dissipation and damping properties of composites [51]. The results of reticulate CNT architectures within composites show order of magnitude improvement in strength [117]. And the significant increase in damping ratio was reported in a shear test on CNT epoxy composite [118]. Among these studies, the CNT polymer composites show nonlinear elasticity and instability by local nanotube buckling in the monotonic compression [13], and hysteresis and viscoelasticity with remarkable damping effect during dynamic mechanical analysis [13, 115], indicating the soft-tissue like properties. Interestingly, the VACNT arrays also exhibit hysteretic behavior in cyclic loading [86] and time-dependent viscoelastic response in creep or stress relaxation tests [87, 90, 119].

Therefore, it is very important and interesting to unveil the viscoelastic properties of continuous CNT polymer composite under compression. What is more, the quantitative study by modeling on the viscoelastic property characterization is still lacking. Here, our objective is to design and fabricate a continuous CNT-based composite and to understand the viscoelastic properties with quantitative modeling

approach. As planned, we fabricated the VACNT polymer composite by using direct infiltration technique and measured the compressive properties and static/dynamic viscoelastic properties by monotonic compression, creep, stress relaxation and DMA. The characterization results show that the CNT reinforced composites exhibit a significant increase in compressive stiffness and exceptional reinforcement on structural rigidity and damping property with outstanding energy dissipation capacity.

### 4.1.2 Viscoelasticity

A viscoelastic material, like it sounds, is a material that has a combination of elastic and viscous behavior [120-122], which is often seen in polymer material. Its response to an imposed loading condition is not only dependent on stress or strain level, but also the rate the condition is applied and the amount of time it is applied [120-122]. The time dependent response is the viscous behavior and is similar to a damper while the instant response is elastic behavior and is dependent on the magnitude of the load and is similar to a spring. So, the viscoelastic behavior can be generally described as a spring-damper system in Figure 4.1a-b and more complicated system in Figure 4.1c-d. On the molecular level, the elastic deformation is generally the stretching or compressing of the chemical bonds in the polymeric chain, while viscous deformation corresponds to the chemical bonds sliding across one another and rearranging themselves [121, 122].

In order to characterize the viscoelasticity of a material, static and dynamic loading conditions must be examined. The static loading conditions are either an imposed stress held constant over time while strain is measured (creep), or an imposed strain held constant while stress is measured (stress relaxation). The simplest models

for the creep and stress relaxation response of a viscoelastic material can be seen in Figure 4.1c-d with a spring and damper in parallel (Kelvin-Voigt model) or a spring and damper in series (Maxwell model), respectively [120, 122].

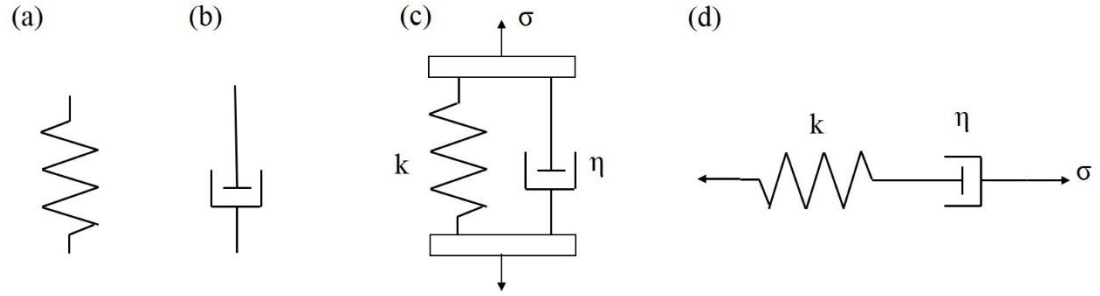


Figure 4.1 Schematic systems for viscoelasticity. (a) Spring. (b) Damper. (c) Kelvin–Voigt model. (d) Maxwell model.

The method used to determine the viscoelastic response under dynamic loading conditions is called Dynamic Mechanical Analysis (DMA) shown in Figure 4.2. DMA has a cyclic sinusoidal loading and can varies temperature or frequency in the process. DMA testing is a good way to characterize the viscoelastic response as well as the molecular mechanisms and transitions of a material undergoing rheological changes. DMA testing measures the complex modulus, storage modulus, loss modulus, and tanδ value which are all interrelated with the viscoelasticity in dynamic process.

The complex modulus measured through the sinusoidal cyclic loading and unloading process during DMA is the amplitude of the stress over the amplitude of the strain seen in Figure 4.2. The complex modulus is made up of the storage and loss moduli, and it takes the form: $E^*=E'+E''i$. Where E* is the complex modulus, E′ is the storage modulus which represents the elastically stored energy, and E″ is the loss modulus which represents the energy absorbed and dissipated as heat. The ratio of dissipated energy to elastically stored energy is represented by the loss factor tanδ=

$E''/E'$. Each of these quantities can change with variations in morphology or frequency and is therefore temperature and frequency dependent in a viscoelastic material.

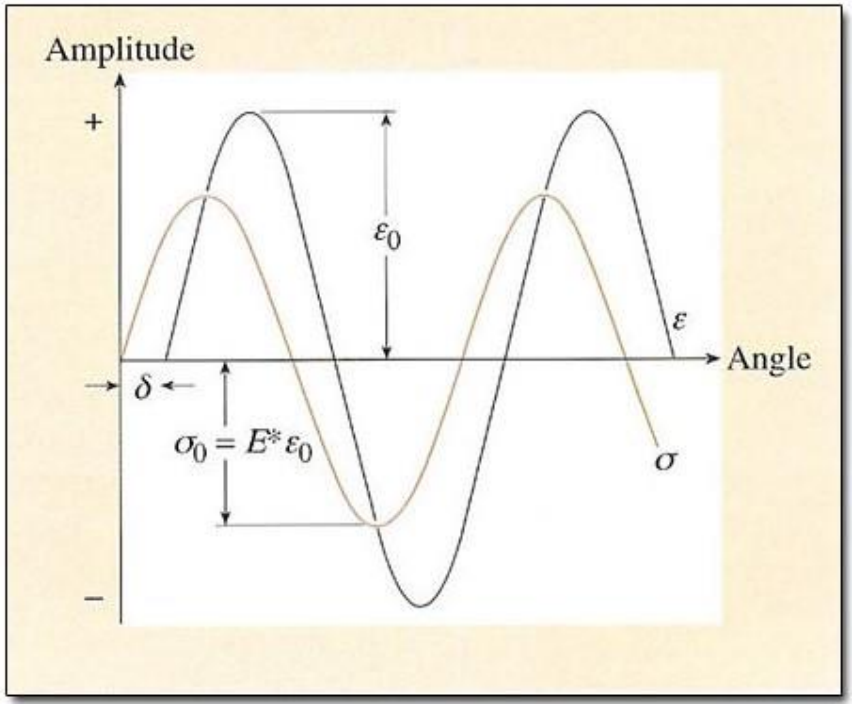


Figure 4.2 Typical sinusoidal response during DMA testing.[123]

### 4.1.3 Time Temperature Superposition

The theory of time temperature superposition (TTS) is a method used in the analysis of viscoelastic materials that allows data taken over a small time frame or frequency range with a number of temperatures, to be shifted on a log scale and to be able to predict data at much larger frequency or time scales [120-122].

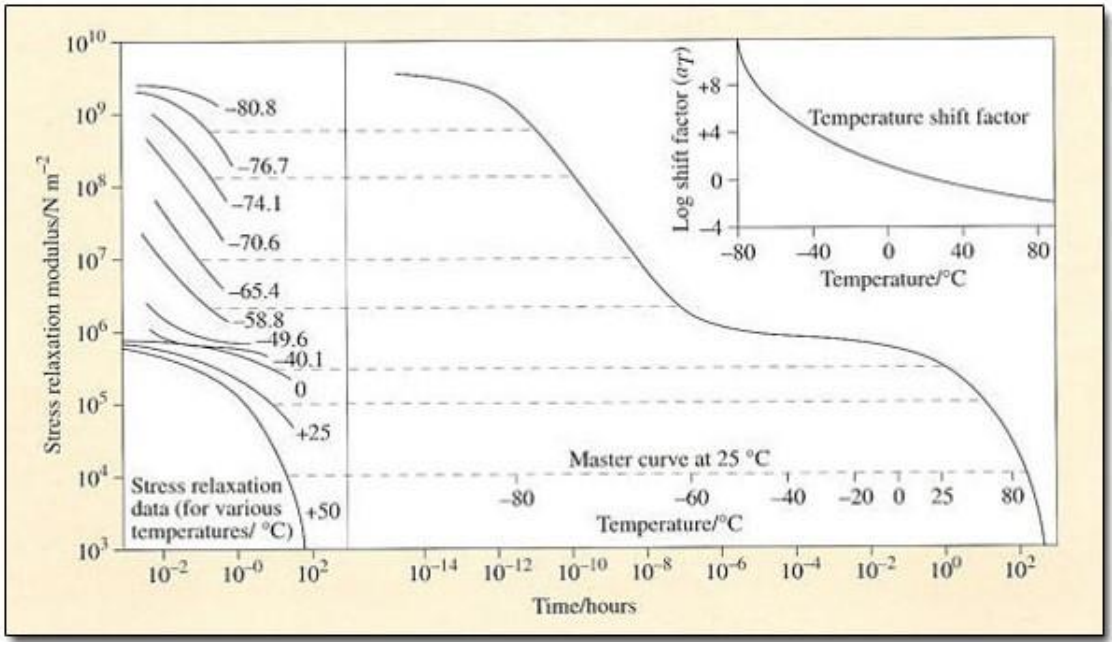


Figure 4.3 Example of Time-Temperature Superposition master curve. [124]

Looking at Figure 4.3, it can be seen that data taken at different temperatures but all for 3 decades of time can be shifted horizontally due to the superposition principal to cover 8 decades of time. This can be used to get months of creep data with just hours of testing, or DMA frequency data well out of reach of an experimental setup. This is an empirical model that shifts experimental data horizontally to match up with data at a reference temperature. The data at the reference temperature is set as base and therefore the entire master curve created is an approximation of the response at the reference temperature. John ferry did a lot of work developing this method [122], and helped determine the Williams-Landel-Ferry (WLF) equation:

$$\log \alpha_t = \frac{-C_1(T - T_0)}{C_2 + (T - T_0)} \tag{4.10}$$

This equation uses the empirically determined shift factors to solve for $C_1$ and $C_2$. With $C_1$ and $C_2$, the shift factors can be determined for any reference temperature, and the

viscoelastic curves can be shifted to a reference temperature of the user's choosing. TTS is a powerful analytical tool; however it cannot be used for any material. According to Ferry [122], there are three criteria that must be satisfied in order for TTS to be applicable: 1. The adjacent curves must be able to line up and superimpose each other; 2. The same shift values must hold true across all viscoelastic properties; 3. The temperature dependence of the shift factors must have a reasonable form, such as WLF equation closely. With the understanding of these static and dynamic viscoelastic properties of the CNT polymer composites over wide ranges of time, temperature, and frequency, it will provide insight into the energy absorption capabilities in a composite structure.

## 4.2 Methods and Materials

### 4.2.1 Continuous CNT-PDMS composite fabrication

The CNT-PDMS composite was made by direct infiltration. As shown in Figure 4.4, the PDMS (a mixture of resin and hardener at a volume ratio of 10:1) was put in vacuum chamber first to get rid of air bubbles. The VACNT array sample was set on a stage connected to vacuum pump, and the droplets of PDMS were delivered into the VACNT top surface one by one, and each droplet was sucked into the VACNT arrays within several to tens of minutes. The infiltration became slower as more PDMS droplets were delivered until saturation. After the infiltration process was completed, the sample was put in a vacuum chamber to further get rid of air bubbles within the PDMS. Then the composite sample was placed in an oven at $100^0$C overnight to allow full curing.

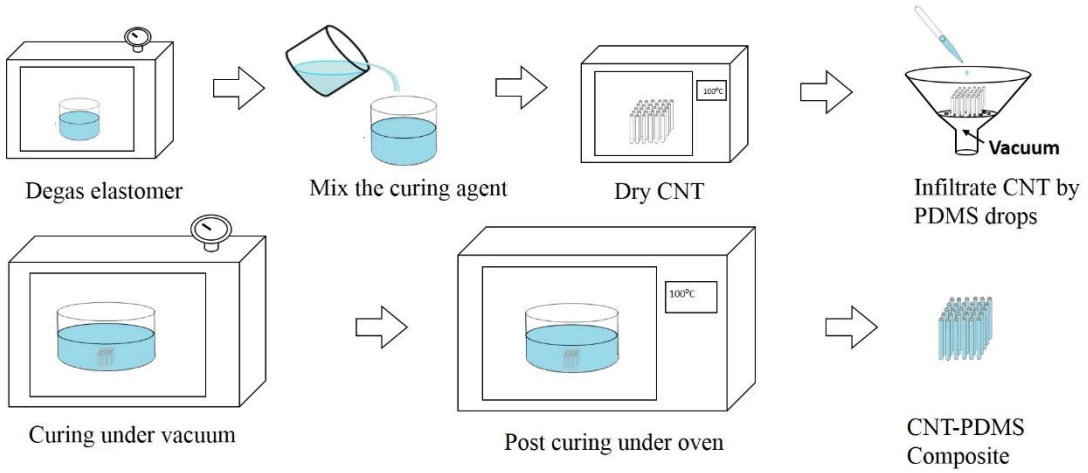


Figure 4.4 Schematic of CNT-PDMS fabrication process, including degasing, mixing solvent, infiltrating CNTs by PDMS droplets, curing and post curing.

The resultant composites consist of VACNTs as filler and the PDMS as matrix in a cubic block shape (~1.5×1.5×1.5mm$^3$) as shown in Figure 4.5a. The weight content of CNT in composite was measured by micro-balance for the weight of CNT arrays and composites, respectively, and also confirmed by thermogravimetry (TGA). Figure 4.6 shows TGA curves for neat PDMS, MWNTs and CNT-PDMS composites in air. According to weight ratio and TGA result, the mass loading of CNTs in composites was around 10.1wt%, showing a high content of CNTs. Assuming the density of MWCNT is 2.2g/cm$^3$ [110], the estimated volume fraction of nanotube was around 4.9%, comparable with the calculated volume fraction by SEM images in Figure 4.7. Based on SEM observation in Figure 4.7, the average outer diameter (2r) of CNT is around 22nm and the inter-tube distance (D) is around ~100nm. Assuming the nanotubes are uniformly distributed and have same length (L), the volume ratio of CNT in the bundle is $f_{CNT} = \pi r^2 L / \pi(\frac{D}{2})^2 L \approx 4.8\%$ and the porosity of filling air is around 95.2%

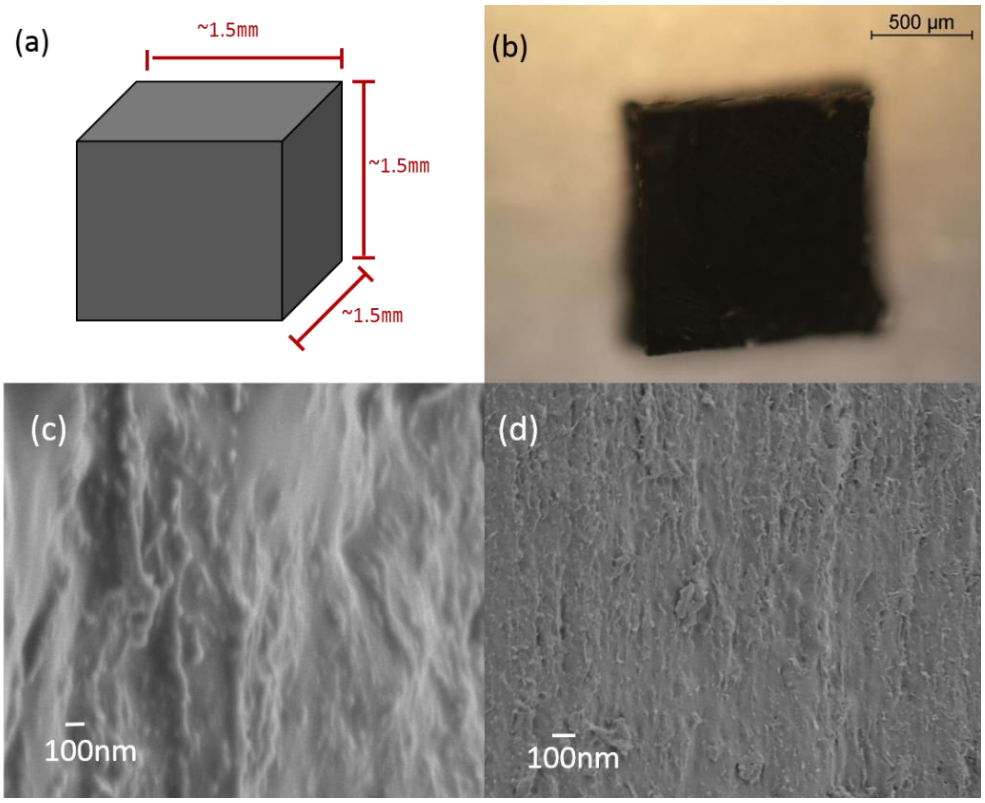


Figure 4.5 Fabricated CNT-PDMS composite sample characterization. (a) Schematic of cubic composite samples. (b) Optical images of composite sample. (c) High resolution image showing the full infiltration of PDMS into VACNT arrays. (d) SEM image show the alignment distribution of CNTs within composites after infiltration.

In order to confirm the infiltration degree, the void fraction in composite was also estimated by employing the formula:

$$V_{void} = 1 - \frac{W_{CNT}/\rho_{CNT} + (W_{comp} - W_{CNT})/\rho_{PDMS}}{W_{comp}/\rho_{comp}} \tag{4.11}$$

The value of void fraction is around 3.17%, showing that the infiltration degree is acceptable with almost full infiltration. Also, the SEM images on the intersecting surface of composites are shown in Figure 4.5c-d. The observations suggest that the initial high porosity among nanotubes is completely infiltrated by the polymer matrix and the nanotubes keep their original alignment distribution. Some polymer does not enter the

central internal cavity within the nanotubes, due to the typically capillary structure produced by CVD process.

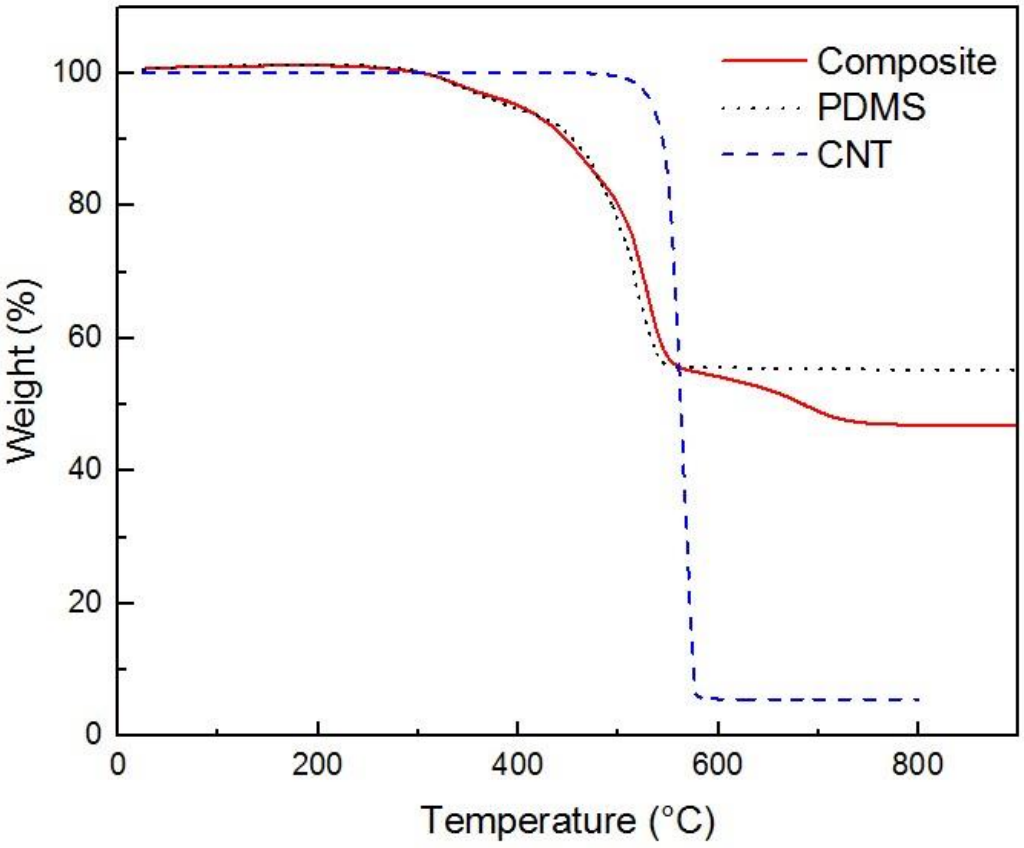


Figure 4.6 TGA curves for neat PDMS and CNT and a composite of CNT/PDMS, no change in temperature of decomposition of PDMS and CNT-PDMS composistes was observed.

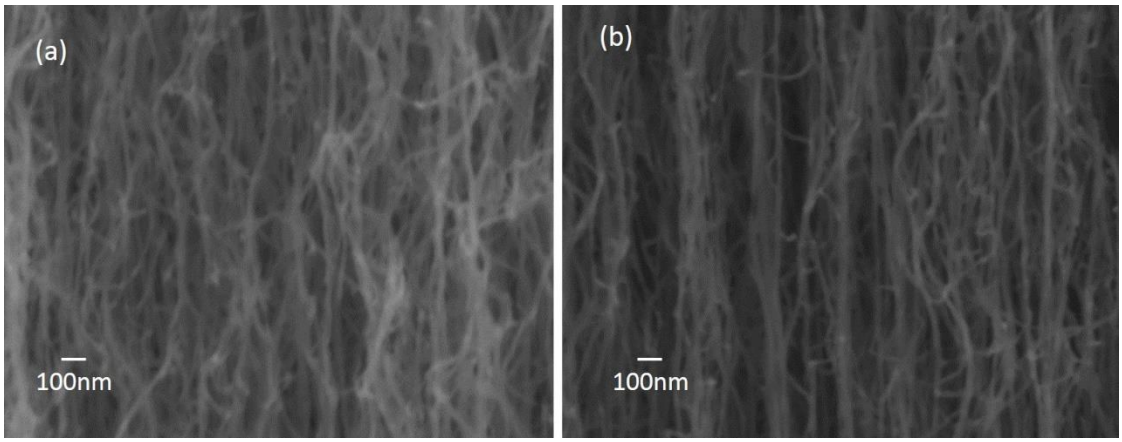

Figure 4.7 SEM images for VACNT arrays, show nanotube diameter and distance between adjunct nanotubes.

### 4.2.2 Static viscoelastic property characterization

#### 4.2.2.1 Creep and Stress Relaxation

To investigate the static viscoelastic properties of CNT-PDMS composites, creep and stress relaxation tests were performed with wide stress/strain range. Creep tests were performed at a constant load and room temperature, and the stress was held for 30 minutes and the deflection data was recorded by TA-Q800. PDMS was tested with the load of 0.12 MPa, 0.3 MPa, 0.7 MPa, 2.9 MPA and 5.0 MPa, respectively, while the CNT-PDMS composites was tested with the load of 0.5 MPa, 0.9 MPa, 1.5 MPa, 3.0 MPa and 5.0MPa. The tested loads were selected according to the corresponding strain range from 5% to 50%, and the stress levels placed on both materials are in the non-linear viscoelastic range. Similarly, stress relaxation tests were performed at a constant strain and room temperature, and was held for 30 minutes and the deflection data was recorded by TA-Q800. PDMS and CNT-PDMS composite were tested with the strain from 5% to 50% to

elucidate the non-linear viscoelastic behavior of both materials, where the strain levels placed on both materials are in the non-linear viscoelastic region.

#### 4.2.2.2 Temperature variation

For temperature effects on static viscoelastic properties, both creep and stress relaxation were conducted in small stress/strain range with temperature variation in order to satisfy the WLF assumptions. Creep tests were performed at a constant small load and identical temperature for each test and then temperatures were varied in different tests for time-temperature superposition (TTS). The temperature ranges between 30 ℃ and 55 ℃ for PDMS and composite. PDMS was loaded to 0.12 MPa within 2s while the CNT-PDMS composites was loaded to 0.5 MPa within 2s. The high ramp rates minimized creep taking place during loading, and the stress levels placed on both materials are in the linear viscoelastic range. The stress was held constant for 30 minutes and the deflection data was recorded by TA-Q800. Stress relaxation tests were performed at a constant low strain and identical temperature for each test and temperatures were varied in order to obtain data for TTS. The temperature ranges between 30 ℃ and 55 ℃ for PDMS and composites. PDMS and CNT-PDMS composites were both compressed to a strain of 5% within 2s. Once again the high ramp rates minimized relaxation taking place during loading, and the strain levels placed on both materials are in the linear viscoelastic range. The strain was held constant for 30 minutes and the force data were recorded.

### 4.2.3 Dynamic viscoelastic property characterization

For each test, frequency variation tests were performed with identical temperature. And temperatures changed from 30 ℃ to 90 ℃ among tests in order to use TTS to obtain DMA data over a wider range of frequency outside the capabilities of the machine. For each test, the sample was placed in the compressive fixture with pre-load and the environmental furnace was used to reach the required temperature. Then the sample was compressed to the mean strain value of 3% and started DMA test with strain amplitude of 0.5%, giving an oscillating strain range of 2.5% – 3.5%, which kept the strain in the linear viscoelastic region for both the PDMS and CNT-PDMS composites A frequency sweep over a range from 0.1 Hz to 10 Hz was employed that had a frequency ramp rate of 1 octave/min. Three samples of each material were tested at each temperature to determine an average response and reduce possible error from sample variation.

## 4.3 Results and Discussion

### 4.3.1 Creep and stress relaxation

#### 4.3.1.1 Stress/strain variation

The creep and stress relaxation testing results of PDMS and CNT-PDMS composites are seen in Figure 4.8. The creep results show corresponding strain of PDMS and CNT-PDMS composites in different stress level, while stress relaxation tests show corresponding stress of PDMS and composites in different strain level. The stress/strain levels were selected according to a wide strain range from 5% to 50% in order to elucidate the viscoelastic behavior of both materials in large scale creep and stress relaxation, especially in the non-linear viscoelastic region. Both strain/stress-

time response of PDMS and composites could be divided into a short initial stage with sharp increase in strain (creep) or decrease in stress (stress relaxation), and a wide plateau stage in which the strain/stress rate is almost zero. All samples show higher increase in strain (creep) or decrease in stress (stress relaxation) when higher step stress/strain levels were applied. These progressive decrease in stress and increase in strain suggest the typical time-dependent behavior of viscoelastic materials.

For linear viscoelastic behavior, the relaxation/creep rate does not depend on the strain/stress level, and instead can be characterized by a constant value. On the other hand, the nonlinear viscoelastic behavior is strongly depend on the strain/stress level, therefore the viscoelastic parameters change with time and stress/strain. Until now, there are many developed theories for the analysis of nonlinear viscoelasticity [119, 121, 125]. Due to the complexity of these nonlinear theoretical formulations, empirical approaches are often used to describe the main features of the creep and stress relaxation behavior of viscoelastic materials.

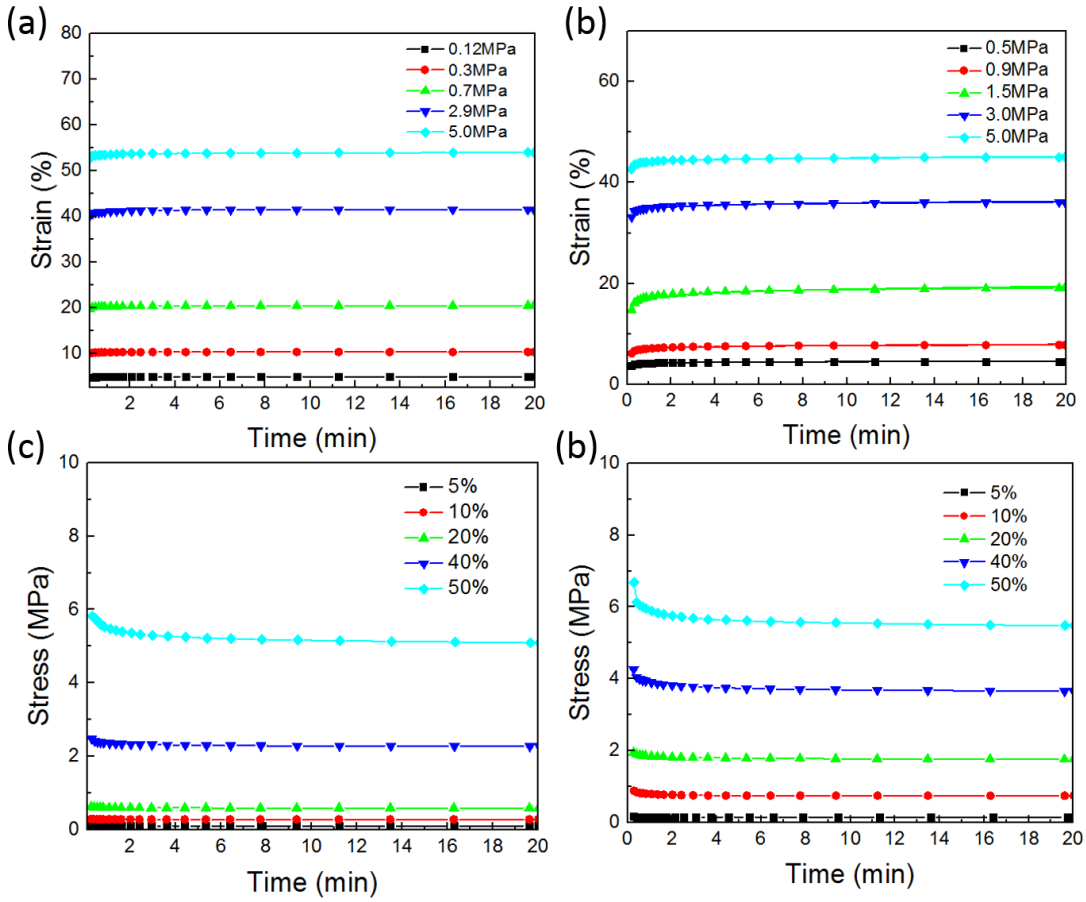


Figure 4.8 Viscoelastic behavior of PDMS and CNT-PDMS composites in large stress/strain scale. Strain plots over time in experiments (scatters) and power-law curve fitting (lines) for creep: (a) PDMS and (b) CNT-PDMS composites. Stress plots over time in experiments (scatters) and power-law curve fitting (lines) for stress relaxation: (c) PDMS and (d) CNT-PDMS composites.

To make the analysis more accurate and effective, we employed the simple and classical viscoelastic model: power-law model [121] for creep and stress relaxation tests. For materials whose creep/stress relaxation response may be described by a separable time-independent and time depend strain/stress, the following expression has often been found to yield a good description of creep/stress relaxation of viscoelastic materials at constant stress/strain:

$$\varepsilon(t) = \mathrm{r}\, t^{n} \tag{4.12}$$

$$\sigma(t) = \mathrm{r}\, t^{m} \tag{4.13}$$

Where ε(t), σ(t) are the strain and stress, respectively, as functions of time and t may be taken to represent a dimensionless time ratio $t/t_0$, where $t_0$ is the unit time; r is the power-law coefficient and n and m are dimensionless power-law exponents that indicate the rates of creep and stress relaxation respectively.

Figure 4.8 show power-law fitting results: the scatters represent the experimental data and solid lines represent the power-law curve fitting. The good match between experimental and theoretical model confirms that the power-law provides a good description of the nonlinear behavior of both PDMS and CNT-PDMS composites. And the corresponding value of r and n and m were shown in next sections, respectively.

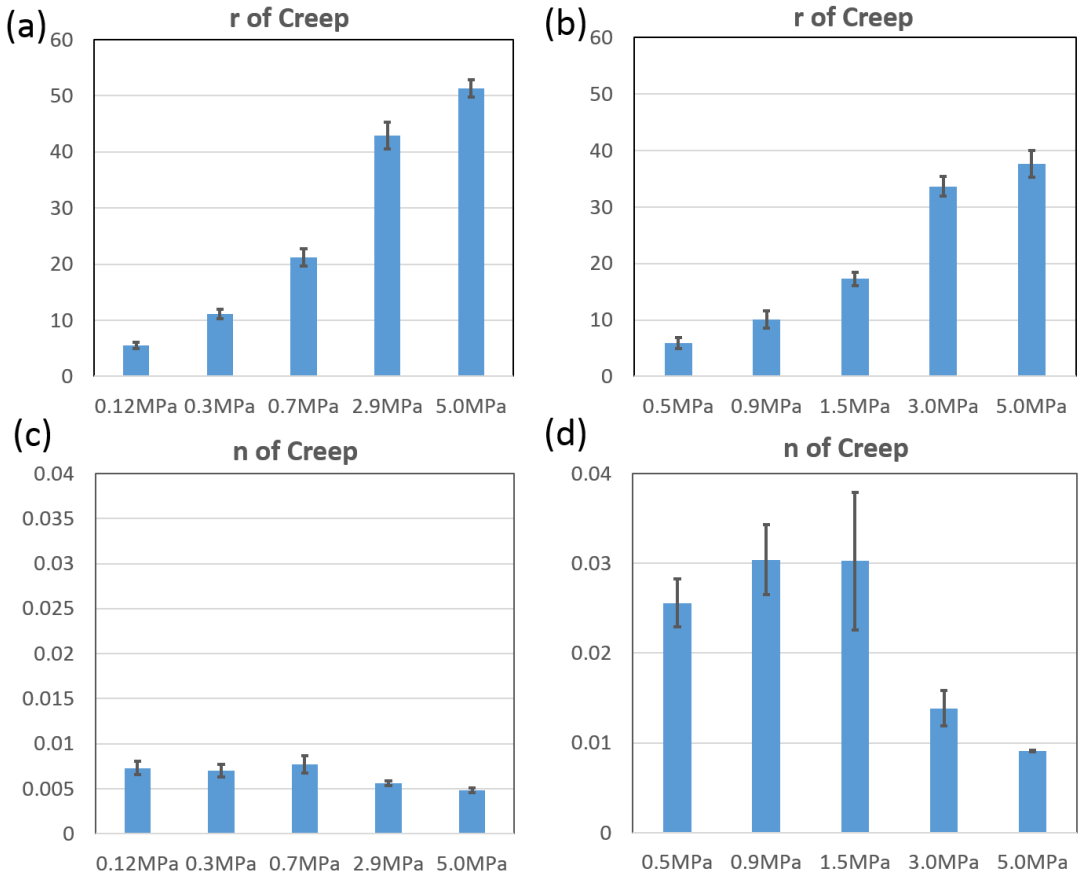


Figure 4.9 Creep exponent n and creep coefficient r for PDMS and CNT-PDMS composites. (a) r value for PDMS creep test. (b) r value for CNT-PDMS creep test. (c) n value for PDMS creep test. (d) n value for CNT-PDMS composite creep test.

At low stress values in Figure 4.9a, PDMS shows low r value around 5, and then r increases up to 50 with applied stress increase, suggesting that the strain level will increase with applied stress. And the similar trend was observed in CNT-PDMS composites, with a start value of 5 and final value of 38. The comparable r values between PDMS and CNT-PDMS composites are because the applied stress for each test was selected according to step strain level from 5% to 50% in order to investigate the nonlinear viscoelastic behavior. For the creep exponent of PDMS, n varies around the value of 0.007 below a critical stress level of 0.7MPa, and shows a relative constant

viscoelastic behavior. In this region (0.12~0.7 MPa), the quasi-horizontal distribution of n suggests an almost linear viscoelastic behavior of PDMS, which does not depend on the applied stress. After that, the creep exponent decreases dramatically to 0.005 in high stress level (5.0MPa), suggesting that the PDMS deforms and maintains the step strain faster and has less viscous response at large stress condition. The sharp decrease in the high stress level region suggests that the PDMS can maintain its linear viscoelastic properties in low stress level (<0.7MPa) and above this level, the viscoelastic properties become nonlinear.

The viscoelastic response of CNT-PDMS composites was also investigated by the creep exponent n in Figure 4.9d, the results show the composite has an initial n value of 0.025 at 0.5MPa and 0.03 in medium stress region and then a decreased value of 0.009 at 5.0MPa, suggesting that the viscoelasticity of composite drastically varies along with applied stress. Compared with PDMS, the CNT filling has a significant effects on the viscous behavior of composite with much higher n values, for example, n values are over 0.025 in low stress level and 0.009 in high stress level for composites, while the n values of PDMS are only around 0.007 in low stress level and 0.005 in high stress level. The continuous CNTs in full infiltrated composite were strong supported by neighboring polymer matrix, therefore the ultimate mechanical properties of CNT could be utilized with considerable increase in elastic modulus and also in viscoelastic creep rates. Furthermore, the existence of CNT not only significantly increases viscous creep rates for step stress, but also change the nonlinear viscoelastic response among different stress levels.

To further investigate the static viscoelastic properties of CNT reinforced composites, the stress relaxation tests were conducted and the results were summarized in Figure 4.10, with r value for stress level and m value for relaxation exponent. The r value

starts with low value around 0.2 and then dramatically increases up to 6.2 with the strain range from 5% to 50%, suggesting that the relaxed equilibrium stress will increase as applied strain increases and they have nearly linear relationship. And similar r data was observed in CNT-PDMS composites, with much higher initial r value of 0.5 and final value of 7.9 at 50% strain. As seen from Figure 4.10a-b, the absolute r value of composite is much higher than PDMS and the statistical Student's t-tests show significant difference between r values of composites and PDMS in all strain levels, respectively, indicating an effective CNT reinforcement in terms of material stiffness, epically in low stain region. When strain increases up to 40%, the reinforcement effect of CNT decreases with less difference in r values between two materials.

For the stress relaxation exponent of PDMS, m value in different strain level can be divided into two regions: an initial region in low strain range (<20%) with m value around -0.007, and a significantly decreased region of m value down to -0.024 in high strain range (>40%). This distribution is different from the creep exponent behavior of PDMS in Figure 4.9, where the viscous response of PDMS becomes significant in high stress level. The stress relaxation exponent m of CNT reinforced composites varies between -0.028 and -0.04 in the strain range from 5% to 50%, but still can be roughly divided into low strain level region (<20%) and high strain level region (>40%). In low strain region, the m varies around -0.03 and have approximate reciprocal relationship with the corresponding creep exponent n, while in high strain range, the relaxation exponent decreases down to –0.037 with obvious viscous relaxation response. Analogous to the PDMS, the relaxation component has nearly reciprocal relationship with the corresponding creep component n. Compared with PDMS, the CNT reinforced composite has significantly increased m value in low strain level, which is a strong evidence that the

CNT filling has a significant effects on the viscous response of CNT-PDMS composite by increasing relaxation rate.

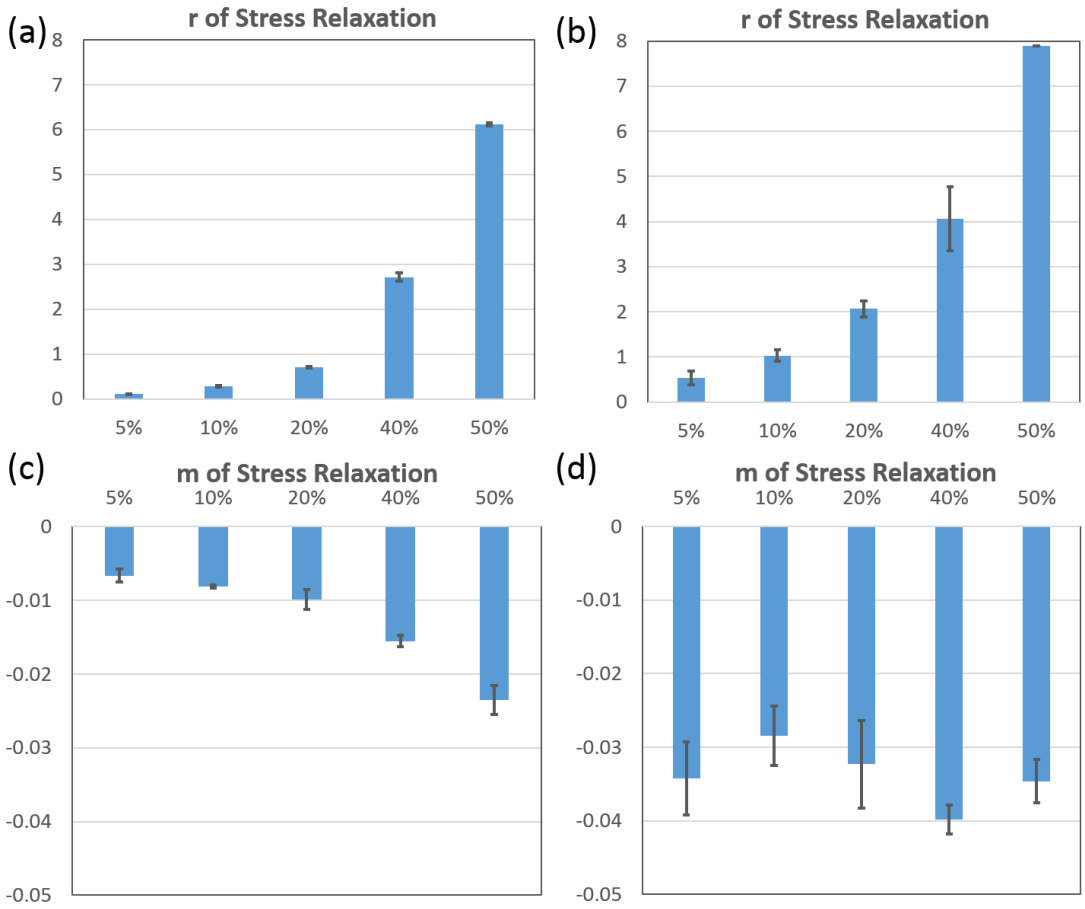


Figure 4.10 Stress relaxation exponent m and creep coefficient r for PDMS and CNT-PDMS composites. (a) r value for PDMS stress relaxationtest. (b) r value for CNT-PDMS stress relaxation test. (c) m value for PDMS stress relaxation test. (d) m value for CNT-PDMS composite stress relaxation test. Student's t-test was empolyed in the r value difference between PDMS and CNT-PDMS composites. "#" indicates two tested groups are NOT significantly different in student T-tests ($P_{critical}$=0.05).

#### 4.3.1.2 Temperature variation

In order to understand the temperature effect on viscoelastic properties of CNT reinforced composites, we conducted the creep and stress relaxation tests on PDMS and

CNT-PDMS composite with temperature variation. With the static viscoelastic response of, time temperature superposition (TTS) was employed to describe the response of a few half hour tests and shift the data to gather an estimated response for a number of months. The temperature of 55 ℃ test was used as the base temperature and all other results were shifted to fit with it due to the rubber plateau effect.

According to the definition, creep compliance is a measure of the creep response in a material and the stress relaxation modulus is the inverse of the creep. The definition of creep compliance and relaxation modulus are:

$$D = \frac{\varepsilon(t)}{\sigma_0} \tag{4.14}$$

$$E = \frac{\sigma(t)}{\varepsilon_0} \tag{4.15}$$

where $\varepsilon(t)$ is the strain as a function of time while the stress is held at a constant level of $\sigma_0$, and $\sigma(t)$ is the stress as a function of time while the strain is held at a constant level of $\varepsilon_0$. For perfectly linear viscoelastic materials, the relation between creep compliance and relaxation modulus is $E(t)= 1/D(t)$.

It is easily observed in Figure 4.11a-b that the PDMS has much higher creep compliance than the composites, and PDMS has the value ranging from 0.43 to 0.46 over $1\times10^6$ seconds, while the composite has a compliance ranging from 0.03 to 0.036 over $1\times10^6$ seconds. This is to be expected since the creep compliance is essentially the reciprocal of the elastic modulus, while the high elastic modulus (~1TPa) of continuous CNT can be taken full advantage of with lateral support by surrounding matrix. Physically, the creep behavior in composites is caused by both matrix and the CNTs, including the molecular chain shifting position of polymer matrix under imposed load and the interaction between CNTs and matrix interface, like buckling and deformation of CNTs and interfacial slippage.

In the log-log figure, the creep behavior follows the power low $\varepsilon(t) = \mathrm{r}t^n$ very well with almost linear relationship between time and creep compliance. This indicates the creep response is similar and keeps almost constant creep exponent as temperature ranges from 30 ℃ to 55 ℃. Note that the creep compliance decreases as temperature increases, which means that the material becomes stiffer. The observed phenomenon on stiffness increase is called "rubbery plateau effect" for polymer material [126]. Generally, in high temperature region (much higher than Tg), the polymer material will be within the rubbery plateau and hereby the modulus of polymer keep constant in a narrow domain or slightly increase with temperature increase, indicating that the material is somehow stiffening. After this stiffening region, the modulus will decrease again. This region is referred to rubber plateau region, which are often observed in lots of rubber and polymer materials [126-130] in high temperature range. The creep behavior of CNT-reinforced composites also have very good agreement with power law prediction and the creep compliance decreases with temperature, indicating the temperature range is in the rubbery plateau region. However, the scattering of creep compliance of composites among temperatures is much less and the creep compliance between 35 ℃ and 55 ℃ has almost identical values, suggesting that the thermal stability of CNT reduces the temperature influence and therefore provide a temperature stable properties for the composite material.

The results for the relaxation modulus after TTS fitting are seen in Figure 4.11c-d, and they are approximately the inverse of the creep compliance. In our test, the relaxation modulus of the PDMS varies from 2.26 MPa to 2.46 MPa, while the relaxation moduli of composites are between 14.7 MPa and 18.5 MPa, showing much higher values than that of the PDMS. This behavior is similar as the creep compliance due to the inverse relation and gives another strong evidence of efficient CNT enhancement. As temperature

increases from 30 ℃ to 55 ℃, the relaxation modulus of PDMS increases slightly, suggesting the polymer's rubber plateau effects at high temperature region. And in log plot, the relation between relaxation modulus and time has very good linear relation, following the simple non-linear power law relation. As expected, CNT-PDMS composite shows much better thermal stability than PDMS, especially between 35 ℃ and 55 ℃ with less than 2% difference, which is consistent with the temperature stable behavior observed in creep test. This confirms that the thermal stability of CNT can effectively increase the robustness of composites under temperature variation.

WLF fitting was employed to determine the constants C1 and C2 for PDMS and CNT-PDMS composite in creep and stress relaxation to make further prediction for creep and stress relaxation behavior in large time scale. For PDMS in creep, C1 = 5.01 and C2 = 49.5 with R-square of 0.985, and for stress relaxation C1 = 6.11 and C2 = 55.2 with R-square of 0.991. The WLF fits showed good agreements with experimental data in Figure 4.12a-b, respectively. Same as PDMS, CNT-PDMS composite has similar behavior during temperature variation in creep and stress relaxation. For composite in creep, C1 = 0.211 and C2 = 26.6 with R-square of 0.994, and for stress relaxation C1 = 0.148 and C2 = 26.8 with R-square of 0.995. The WLF fits also showed good agreements with experimental data in Figure 4.12c-d, respectively. Compared with PDMS, the shift factors of composites are order of magnitude less for each experimental temperature data point and only have a little increase in 30 ℃. In addition, between 35 ℃ and 55 ℃, both creep and stress relaxation shift factors are almost identical, suggesting that the composites have the same viscoelastic behavior with thermal stability in these regions.

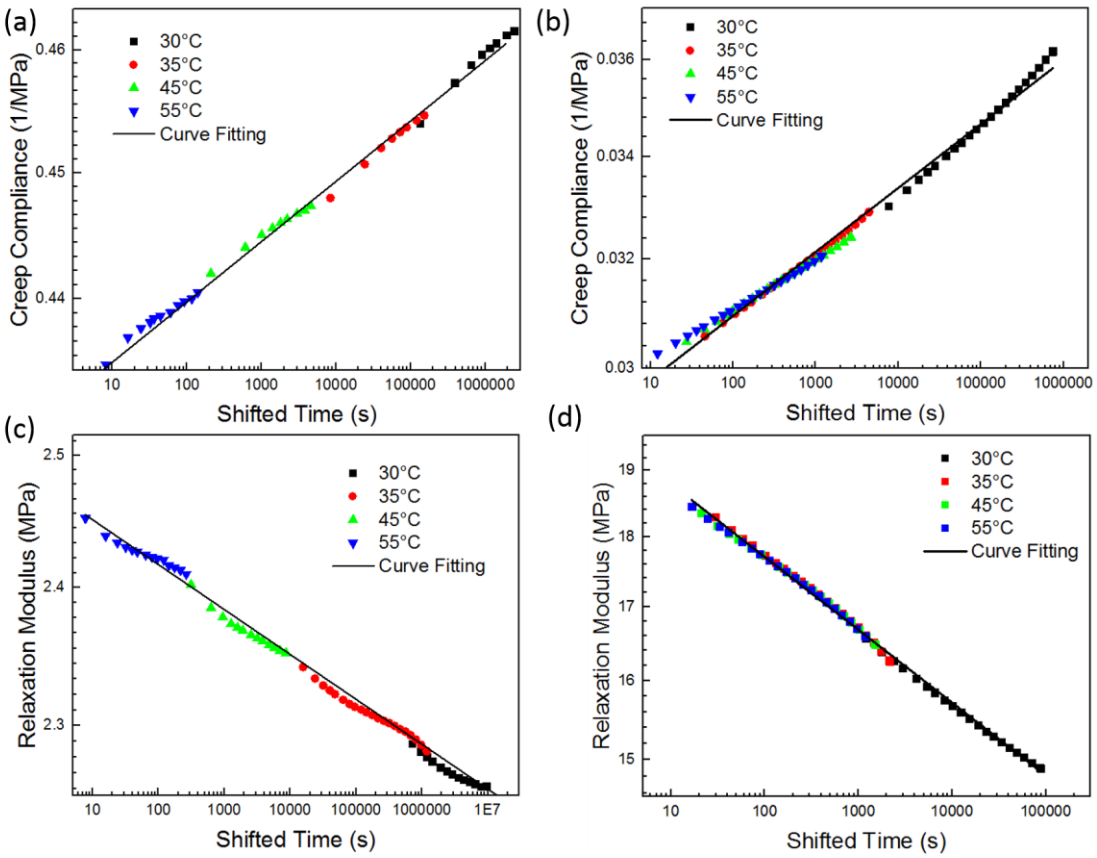


Figure 4.11 Creep compliance and relaxation modulus plots over time under temperature variation. (a) Creep compliance for PDMS; (b) Creep compliance for CNT-PDMS composite. (c) Relaxation modulus for PDMS. (d) Relaxation modulus for CNT-PDMS composite.

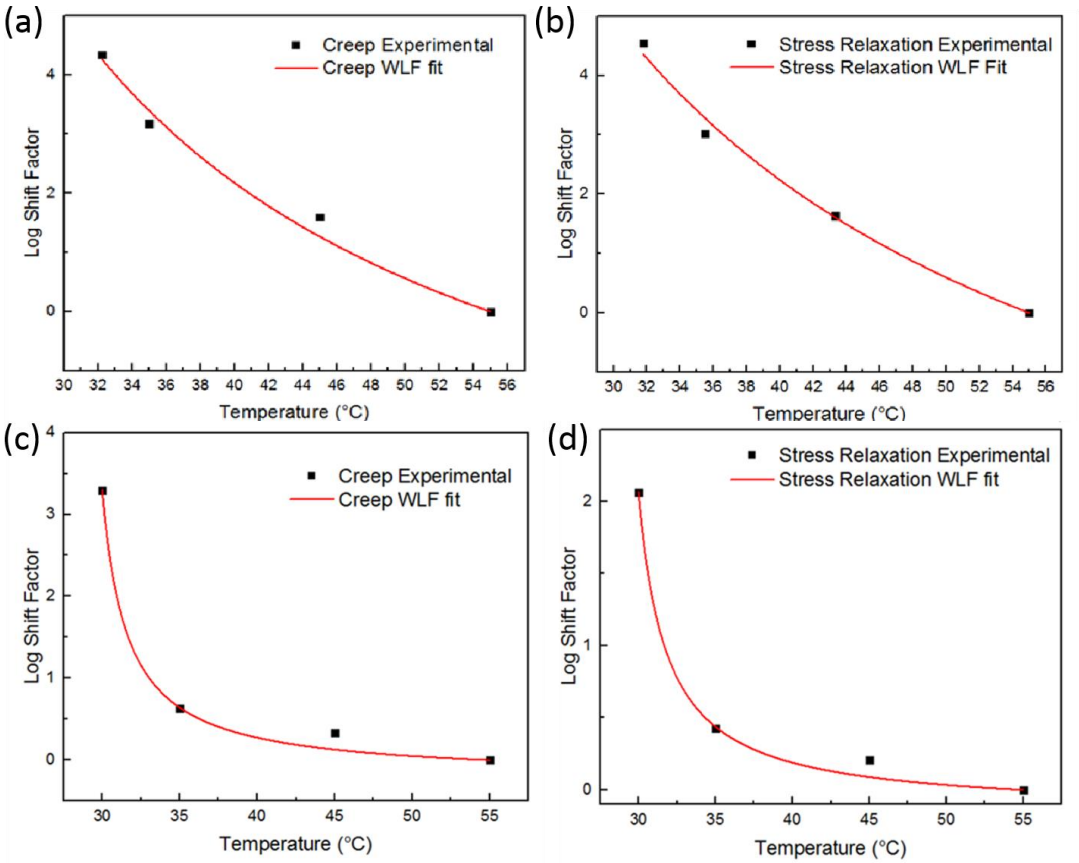


Figure 4.12 WLF fitting of the creep and stress relaxation shift factors. (a) Creep WLF fitting for PDMS. (b) Stress relaxation WLF fitting for PDMS. (d) Creep WLF fitting for CNT-PDMS Composites. (b) Stress relaxation WLF fitting for CNT-PDMS composites.

### 4.3.2 Dynamic mechanical analysis characterization

Out of all the tests used for viscoelastic characterization, the frequency dependent DMA is the most impactful in relating to the energy dissipation and damping performance in composite materials. In order to understand the dynamic response of PDMS and PDMS-CNT composites, DMA testing across the wide range frequency range was conducted. Performing tests from 0.1 Hz to 10 Hz at progressively increasing temperatures gives data that can be shifted ahead for a wide range of frequencies, with time temperature superposition. The temperature range is determined according to the previous static tests in order to keep consistent test condition.

The frequency-storage modulus data for the PDMS can be seen in Figure 4.13. The result shows temperature independent viscoelastic behavior with almost identical storage modulus in different temperature. Since the temperature range is within rubber plateau region, the storage modulus is almost identical or with slight increase as shown in Figure 4.13a. All the tests have the storage modulus around 1.5 MPa at 0.1 Hz and the storage modulus increases slightly up to 1.65 MPa when frequency is higher than 6 Hz, since the increase in rate of loading with frequency will essentially reduce the time dependent chemical bond movement and will stiffen the polymer somehow. On the other hand, the loss modulus of PDMS has temperature dependent behavior and were shifted by TTS in Figure 4.13b. The loss modulus increases from 0.017 MPa to 0.15 MPa. After 500 Hz the loss modulus increases sharply to its maximum value of 0.37 MPa. For each temperature setting, in low frequency region from 0.1Hz to 6Hz, the loss moduli have linear relation with frequency in log plot, following the power law relation, while a significant increase was observed in high frequency region due to the dramatic increased loading rate.

The DMA data for CNT-PDMS composite can be seen in Figure 4.13. The results also have temperature independent relationship between storage modulus and temperature. The storage modulus is almost around 20 MPa at 0.1 Hz and progressively increases up to 26 MPa. Like PDMS, all storage moduli in different temperature conditions show similar values and are very close to each other, while the absolute values of storage moduli are nearly 10 times higher than that of PDMS, which is consistent with the creep and relaxation test. Once again, this is another strong evidence of CNT's significant reinforcement in stiffness. As the frequency increases, the storage modulus of composite increases accordingly, which might be caused by the corresponding stiffening effect of polymer matrix and by the buckling or sliding between CNTs and matrix. The frequency-loss modulus for CNT-PDMS composite after being shifted by TTS is seen in Figure 4.13d, showing a temperature dependent behavior. The loss modulus increases from 1.6 MPa to 5 MPa with frequency from 0.1 Hz to 250Hz. For each temperature testing, the loss moduli between 1 Hz and 10 Hz have almost linear relation with frequency in log plot and follow the power law relation, while the loss moduli below 1 Hz only show a plateau region with only slight decrease. Compared with static viscoelastic tests, the temperature effect on the loss modulus of composite shows relative thermal stable properties.

WLF fitting was done on frequency-loss modulus of DMA data. By using shift factors, the curve fits well for all functions and the constants in the WLF equation were determined to be C1 = 4.26 and C2 = 210.4, with an R square value of 0.999 for PDMS, shown in Figure 4.14a. For CNT-PDMS composites, the experimental shift factors and WLF fit was shown in Figure 4.14b, with C1=4.89 and C2=228.9 and R square value of 0.999. The data showed reasonably good overlap for all DMA functions and the experimental shift factors also agree well with the WLF. This confirms the validity of TTS

when using it to model frequency dependent DMA behavior of PDMS and CNT-PDMS composite for a better prediction for wide frequency range.

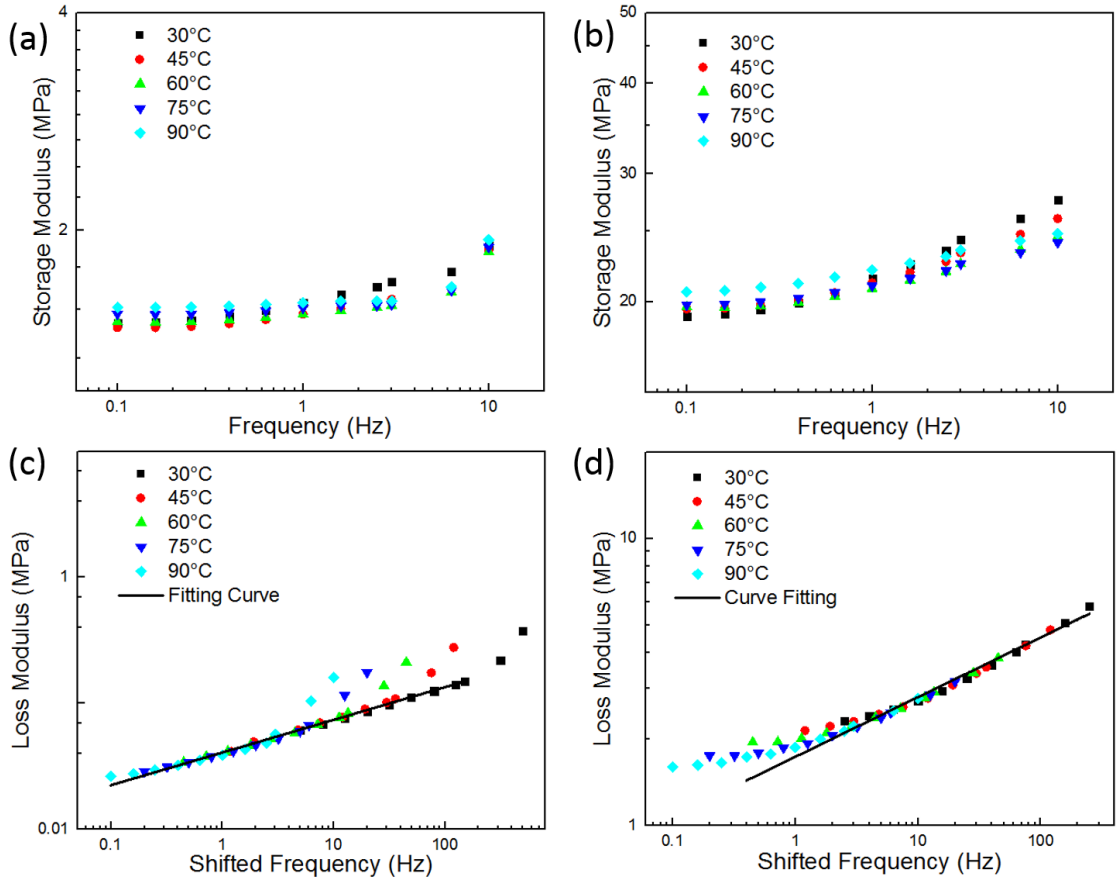


Figure 4.13 Frequency variation under different temperatures of PDMS and CNT-PDMS composite in DMA tests. (a) Storage modulus of PDMS. (b) Storage modulus of CNT-PDMS composite. (c) Loss modulus of PDMS. (d) Loss modulus of CNT-PDMS composite.

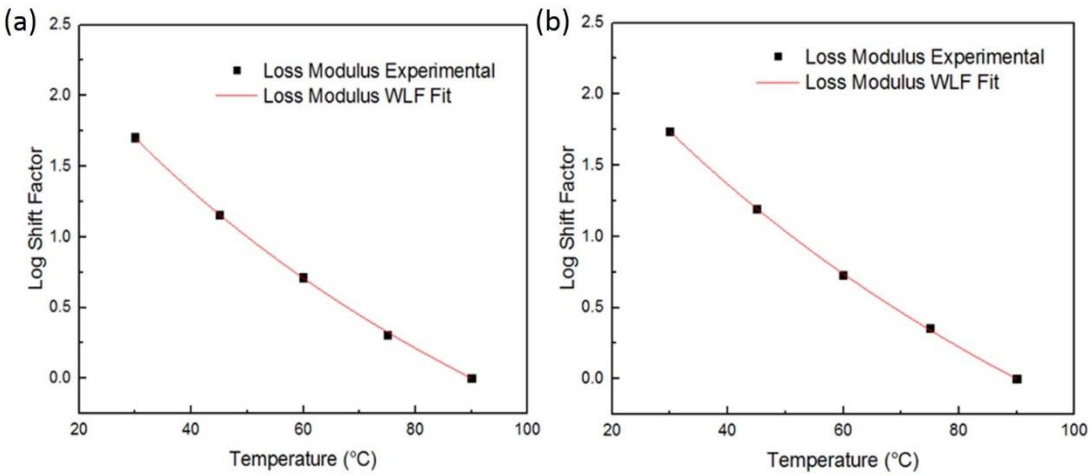

Figure 4.14 WLF fitting of the frequency dependent DMA shift factors for PDMS and CNT-PDMS composites. (a) PDMS. (b) CNT-PDMS composites.

## 4.4 Conclusions

In static viscoelastic tests, the stress variation of creep and strain variation of stress relaxation tests show the nonlinear viscoelastic behavior of PDMS and CNT-PDMS composite. CNT filling has a significant enhancement effect on elastic response with much higher relaxation modulus and much lower creep compliance, and the power-law characterization shows a different viscous response of stress/strain rate of composite samples, suggesting a considerable influence of CNT in viscoelasticity of composites.

The temperature effect on bother materials were also investigated. Both materials show almost constant or slightly increased elastic modulus as temperature increases, which was reported and explained as “rubbery plateau effect” in many studies. And the composite shows even better stability in temperature variation due to thermal insensitivity of CNTs. Furthermore, the temperature effect was tested to predict the viscoelastic response of PDMS and CNT-PDMS composite over a wide range of frequencies by WLF modeling. For DMA test results, as frequency increases, the storage modulus increases slightly and the loss modulus shows quasi-linear increase with frequency. The temperature

effect on both PDMS and CNT-PDMS composite can be neglected in storage modulus, while the loss modulus has moderate decrease with temperature. The WLF constants were solved for TTS and the loss modulus results can be shifted to any reference temperature to determine the damping response.

# Chapter 5

# ANISOTROPIC CHARACTERISTICS OF CNT REINFORCED POLYMER COMPOSITE

## 5.1 Background

Until now, we investigated the mechanical and viscoelastic properties of CNT-PDMS composite and found the remarkable influence of CNT as filler material. These one-dimensional nanostructures are shown to have highly anisotropic physical and chemical properties [131-133]. Therefore, the continuous CNTs have different material properties in longitudinal and radial directions, and corresponding CNT-PDMS composite will also have the anisotropic properties in longitudinal and transverse directions, which is interesting to be explored and is fundamental in engineering application.

To understand the anisotropic properties of CNT-PDMS composites, some previous studies have obtained fundamental data. Jin *et al.* [134] have reported the successful fabrication of aligned carbon nanotube composite by controlling the nanotube orientation and the degree of alignment. Likewise, a polyurethane/SWCNT composite with anisotropic structure is synthesized by two-step process with two-orthogonal-direction distributions of the SWCNTs in the matrix [135]. Further, the mechanical characterization on these continuous CNT reinforced composites were carried out. The stress-strain behaviors of continuous CNT composites were characterized and compared in compression [115] and show remarkable anisotropy between the longitudinal and transverse composites. The other studies on continuous CNT-PDMS composite [13] reported similar anisotropic behavior in compression and damping capacity in DMA tests.

For theoretical models, there are some recent studies [136, 137] which have shown the anisotropic mechanical property prediction of polymer and polymer related composite materials.

However, the anisotropic properties of CNT polymer composite are not fully understood, especially for viscoelastic properties. And there is no quantitative analysis for the viscoelasticity of CNT reinforced composites in terms of anisotropic characterization. Therefore, it is imperative and meaningful to investigate the anisotropic properties of CNT-reinforced composites with experimental and analytical approach. In our work, the CNT-PDMS composites were fabricated first with longitudinal, transverse and random samples. And the compressive characterization on these samples along with pure PDMS were conducted, including quasi-static compression, creep, stress relaxation and dynamic mechanical analysis. Then, two linear viscoelastic models were employed to explain and compare the static viscoelastic data quantitatively and distinguished the anisotropic properties of CNT reinforced composites.

## 5.2 Methods and Materials

### 5.2.1 Random CNT-PDMS composite fabrication

Like the continuous VACNT-PDMS fabrication, the random composite was made by direct infiltration as shown in Figure 5.1. Firstly, the VACNT samples was dispersed by using ultra-sonication in organic solution like ethanol or acetone. And the paste of CNTs was filtrated and put into a plastic model to make it a block shape and was dried after then. After drying, we can get a block of random nanotube structure. Then, the

PDMS (a mixture of resin and hardener at a volume ratio of 10:1) was put in vacuum chamber to get rid of air bubbles. And the random CNT block was set on a stage connected to vacuum pump, and the droplets of PDMS were delivered to the CNT top surface one by one, and each droplet was sucked into the random CNT block within several to tens of minutes. The infiltration became slower as more PDMS droplets were delivered until saturation. After the infiltration process was completed, the sample was put in a vacuum chamber to further get rid of air bubbles within the PDMS. Then the composite sample was placed in an oven at 100°C overnight to allow full curing.

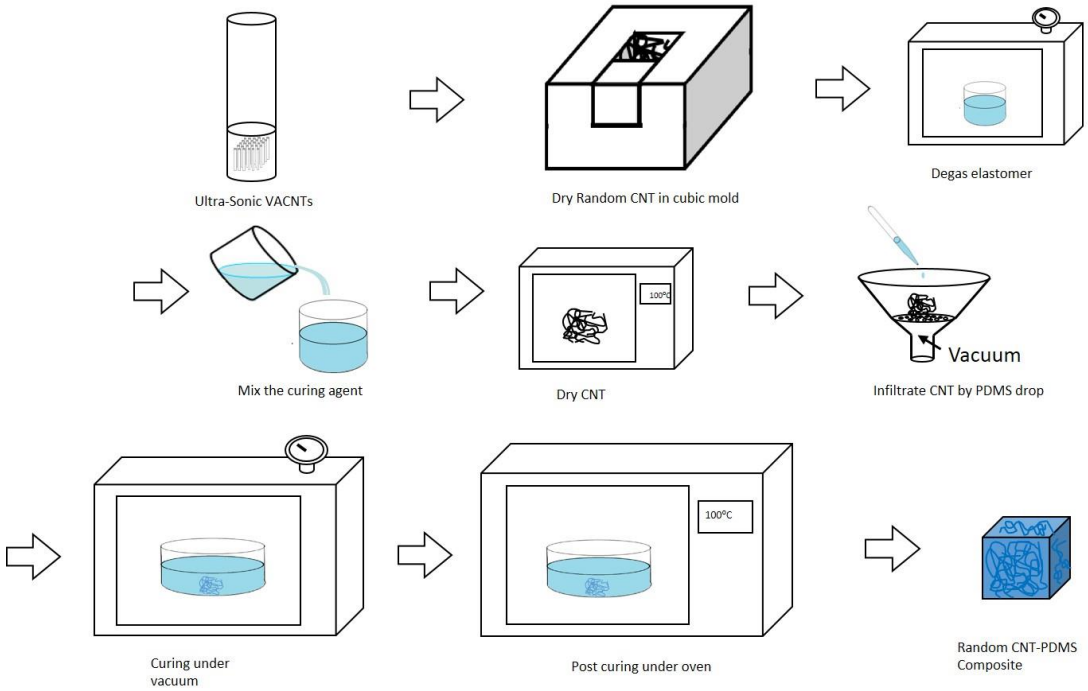


Figure 5.1 Schematic of CNT-DPMS fabrication process, including random CNT preparation, degasing, mixing solvent, infiltrating CNTs, curing and post curing.

The resultant composites consist of CNTs and PDMS as matrix in a cubic block shape (~1.5×1.5×1.5mm$^3$) as shown in Figure 5.2. And the weight fraction of

CNT is around 10.03wt% and the volume fraction was estimated by 4.5%. They are comparable with the VACNT-PDMS composites. The calculated value of void fraction is around 3.72%, showing that the infiltration degree is pretty high and even better than VACNT composites due to the random distribution of CNTs.

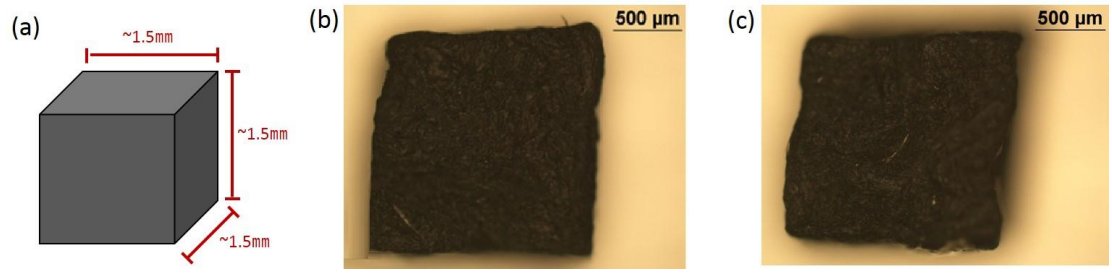

Figure 5.2 Fabricated random CNT-PDMS composite samples. (a) Schematic of cubic composite samples. (b,c) Optical images of composite sample.

### 5.2.2 Quasi-static compression

During quasi-static testing, the sample was compressed up to 60% strain at room temperature with a constant loading speed of 100 μm/min. The quasi-static testing was used to determine the stress-strain response among samples. And the boundaries for the linear regions of compression of the materials would be considered when performing viscoelastic tests. Five different kinds of samples were tested as shown in Figure 5.3, including longitudinal composite (parallel loading on continuous CNT-PDMS composite), transverse composite (normal direction loading on continuous CNT-PDMS composite), random composite, PDMS and VACNT arrays.

### 5.2.3 Creep and stress relaxation

Creep tests were performed at a constant load and room temperature, and the stress was held for 30 minutes and the deflection data was recorded. PDMS was tested

with the load of 0.12MPa, while all composites was tested with the load of 0.5MPa, and the deflection data was recorded. The tested loads were selected according to the corresponding strain, which approximately is around 4% strain to keep the stress levels placed on all materials in the linear viscoelastic region. Likewise, stress relaxation tests were performed at a constant strain and room temperature, and was held for 30 minutes and the loading data was recorded. PDMS and composites were tested with the strain at 4%, to elucidate the linear viscoelastic properties of both PDMS and CNT-PDMS composites.

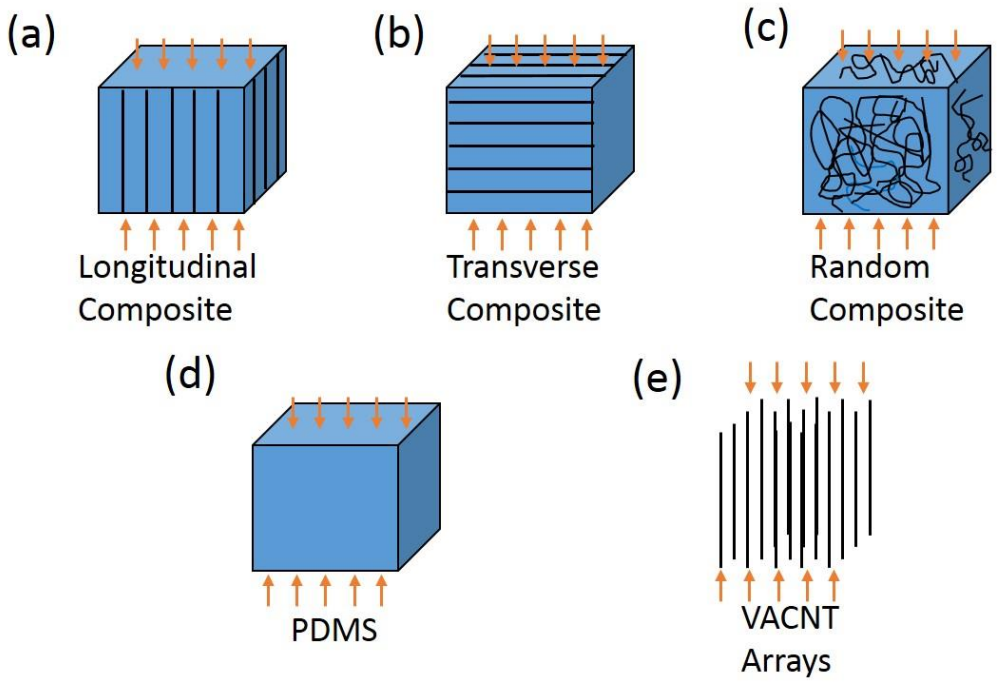


Figure 5.3 Schematics of different materials tested under compression. (a) Longitudinally loaded continuous CNT-PDMS composite (longitudinal composite). (b) Transversely loaded continuous CNT-PDMS composite (transverse composite). (c) Randomly dispersed CNT-PDMS composite (random composite). (d) Pure PDMS sample. (e) Vertically aligned MWNT arrays. All of the samples in compression test have almost identical dimension (~1.5mm ×1.5mm ×1.5mm)

### 5.2.4 Dynamic mechanical analysis

In order to characterize the dynamic viscoelastic properties of CNT reinforced composites in terms of anisotropy, DMA tests were employed. Before each test, the sample was placed in the compressive fixture at room temperature with a small preload to ensure fully contact, and then sample was compressed to a mean strain of 3% and the crosshead was oscillated in a sinusoidal pattern. The strain amplitude for the DMA tests was 0.5%, giving an oscillating strain range of 2.5% – 3.5%, which kept the strain in the linear viscoelastic region for both the PDMS and composites. DMA experimental data were recorded while varying frequency. A frequency sweep over a range from 0.1 Hz to 10 Hz was employed that had a frequency ramp rate of 1 octave/min. Six samples of each material were tested to determine an average response and reduce possible error from sample variation.

### 5.2.5 Linear viscoelastic models

To quantitatively characterize and analyze the static viscoelastic results of CNT polymer composite in different loading conditions, theoretical viscoelastic models were employed. These theoretical models can illustrate the general creep and stress-relaxation behavior of polymers and provide a useful method to describe or recall the interplay between viscous and elastic response, providing us a straightforward means of visualizing the viscoelastic properties.

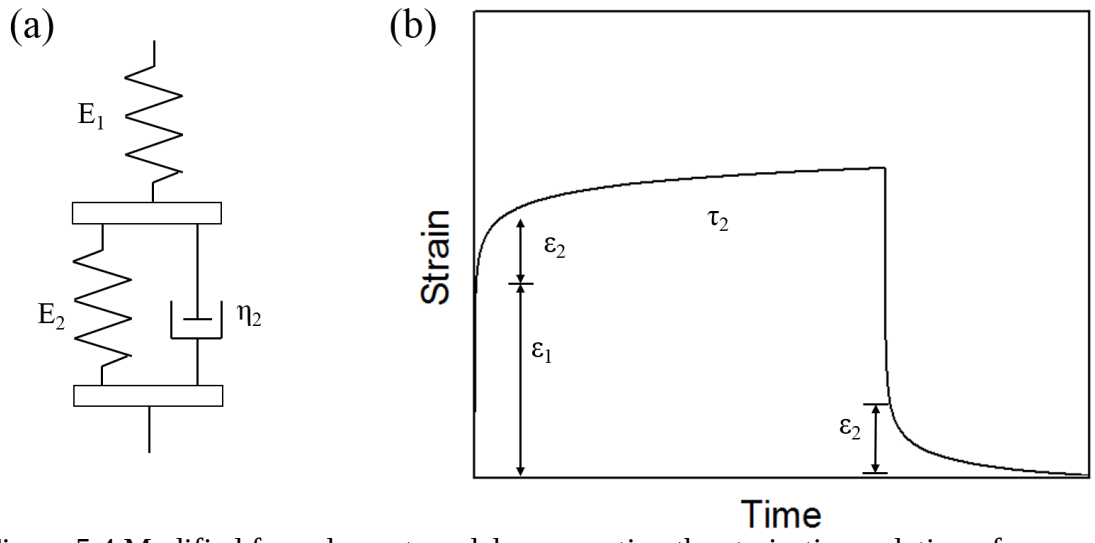


Figure 5.4 Modified four element model representing the strain-time relation of viscoelastic response in creep test. (a) Schematic of modified four element model with a combination of Maxwell model (spring $E_1$ and dashpot $\eta_3$) and Viogt model (spring $E_2$ and dashpot $\eta_2$ in parallel). (b) Interpretation of strain-time response corresponding to the modified four element model.

For the creep behavior, the modified four element model is adopted, as illustrated by Figure 5.4. The elastic spring $E_1$ is linearly connected with the parallel combination of spring $E_2$ and dashpot $\eta_2$. When a constant load is applied, the initial elastic deformation $\varepsilon_1$ comes from the instant response of spring $E_1$, then the later retarded deformation $\varepsilon_2$ comes from the spring-dashpot Voigt model ($E_2$, $\eta_2$), and the last deformation $\varepsilon_3$ is corresponding to the permanent viscous deformation, which is almost zero since the outstanding recoverability of CNT and PDMS. The value of the parameters $E_1$, $E_2$, and $\eta_2$ can be calculated by:

$$\varepsilon_1 = \sigma/E_1 \tag{5.10}$$

$$\varepsilon_2 = (\sigma/E_2)(1 - e^{-t/\tau_2}) \tag{5.11}$$

Where $\tau_2 = \eta_2/E_2$

$$\varepsilon_3 = \sigma/\eta_3\, t \approx 0 \tag{5.12}$$

Total deformation strain at time t is

$$\varepsilon = \sigma/E_1 + (\sigma/E_2)(1 - e^{-t/\tau_2}) \quad (5.13)$$

So, $E_1$ can be immediately determined from equation (5.10) and $E_2$ is determined from the extrapolated deformation $\varepsilon_2$ at infinite time, while $\tau_2$ can be determined from the slope of the plot of creep or recovery curves.

For stress relaxation, the corresponding model is the widely used standard linear solid (SLS) model to represent the viscoelastic properties in compression. As shown in Figure 5.5, SLS is a linear combination of springs and dashpots, representing elastic and viscous components, where the springs $E_1$ and $E_2$ ensure an instantaneous response to a step load and the dashpot $\eta_2$ ensures the time dependent delay to the step load. From Figure 5.5a, the relaxation time $\tau$, equilibrium modulus $E_1$ and viscosity $E_2$ can be derived with the formula:

$$\sigma_1 = E_1\varepsilon \quad (5.14)$$

$$\sigma_2 = (E_2\varepsilon)\, e^{-t/\tau} \quad (5.15)$$

Where $\tau = \eta_2/E_2$

$$\sigma(t) = \varepsilon\,(E_1 + E_2 e^{-t/\tau}) \quad (5.16)$$

Like four element model, $E_1$ and $E_2$ can be immediately determined by equation (5.14) and (5.15) from the relaxation stress and initial stress, and $\eta_2$ can be determined from equation (5.16) according to the relaxation time.

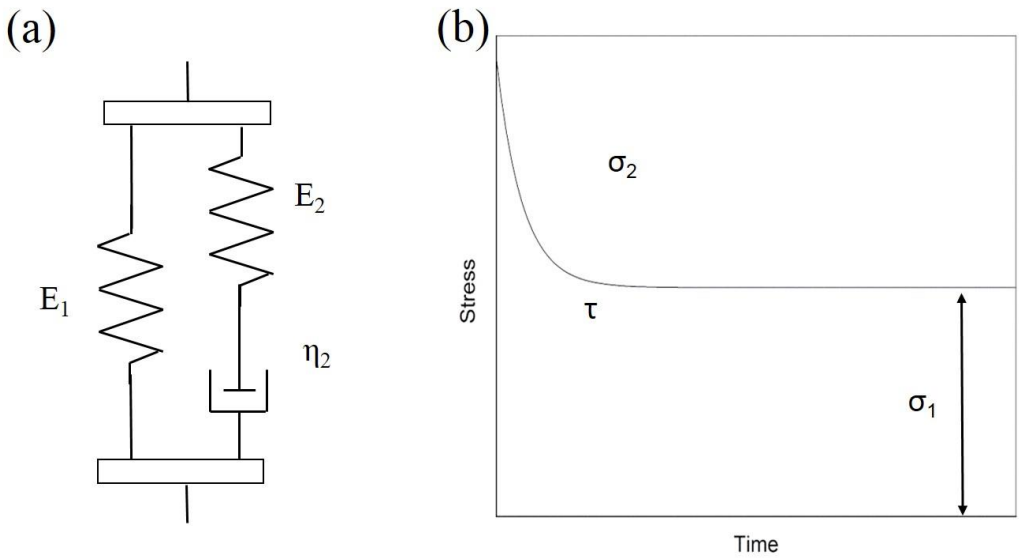


Figure 5.5 Standard linear solid model representing the stress-time relation of viscoelastic response in stress relaxation test. (a) Schematic of standard linear solid model with a combination of Maxwell model (spring $E_2$ and dashpot $\eta_2$) and spring $E_1$. (b) Interpretation of stress-time response corresponding to the standard linear solid.

## 5.3 Results and Discussion

### 5.3.1 Quasi-static compression

Compressive stress-strain characterization results for five different kinds of samples (longitudinal composite, transverse composite, random composite, PDMS and VACNT array) with almost identical dimension are compared in Figure 5.6. The continuous nanotube composite under longitudinal compression (longitudinal composite) exhibits significantly higher stress level in stiffness over the entire strain range. The longitudinal composite has the elastic modulus of ~13.31 MPa between 0 and 8% strain, while pure PDMS shows ~2.63 MPa and the nanotube array only exhibits ~0.41 MPa in

Figure 5.6b, showing a remarkable CNT reinforcement effect on composites in stiffness. Physically, it will be subjected to a much higher compressive stress in order to get deformed or buckled under compression, because CNTs are strongly supported from polymer matrix [7, 138, 139]. By taking full advantage of the high stiffness of continuous CNTs via the support force from matrix, CNT reinforced composites show an extraordinarily enhanced longitudinal modulus and strength as a result.

For the anisotropic properties, random composite exhibits only 6.75 MPa for elastic modulus and transverse composite has 6.26 MPa, which are close to each other but much lower than longitudinal modulus, suggesting that the reinforcement effect is not obvious in other loading conditions. Due to the intrinsic anisotropic property of nanotubes [32, 140], the CNT reinforced composites will only have enough improvement in stiffness by matrix support effect in the longitudinal loading condition, while the random and transverse composite simply have elastic densification and deformation of nanotubes and polymer under compression [12, 13], resulting in relatively lower elastic modulus improvement. All the stress strain curves of composites show plateau (10~50%) and densification (>50%) regions, like the typical compressive behavior in most polymer compression. However, there is no obvious transition between the initial elastic region and the plateau region in composites and PDMS compression, which is often observed in VACNTs due to nanotube buckling, suggesting that the buckling behavior of nanotube becomes weak in low strain condition.

In our experiments, there is no instability of the stress-strain curves in longitudinal composites, which was observed in our previous study [13]. As it was reported before, the instability is caused by the local buckling behavior of the continuous nanotubes [13, 141]. Due to better infiltration and good interfacial contact between nanotubes and matrix, the

longitudinal composite in our test show less nanotube buckling behavior during compression, so there is no obvious instability in the stress-strain response. And the composite loaded in longitudinal direction undergoes the same behavior like the composite loaded in transverse direction, but has better reinforcement effect with gradually increased modulus.

In order to quantitatively study the stress-strain response of composites, we also employed the strain energy density function (SED in Chapter 3). The shear modulus from SED model shows similar results as the stress-strain curves: the longitudinal composites have the highest value of 5.26 MPa, while the random and transverse composites have the moduli around 3.3 MPa, and the PDMS and VACNTs have much lower values below 2.2 MPa, suggesting a significant stiffness reinforcement in the longitudinal directions. And the Lam é constants are order of magnitude less than the shear modulus, with 5.9 kPa of longitudinal composites, ~4.5 kPa for random and transverse composites, around 1.6 kPa for PDMS, and only 0.91 kPa for VACNTs, respectively. The value of the Lam é constants show that the composites still are relatively easier to be shrink in volume in the longitudinal direction when compressed.

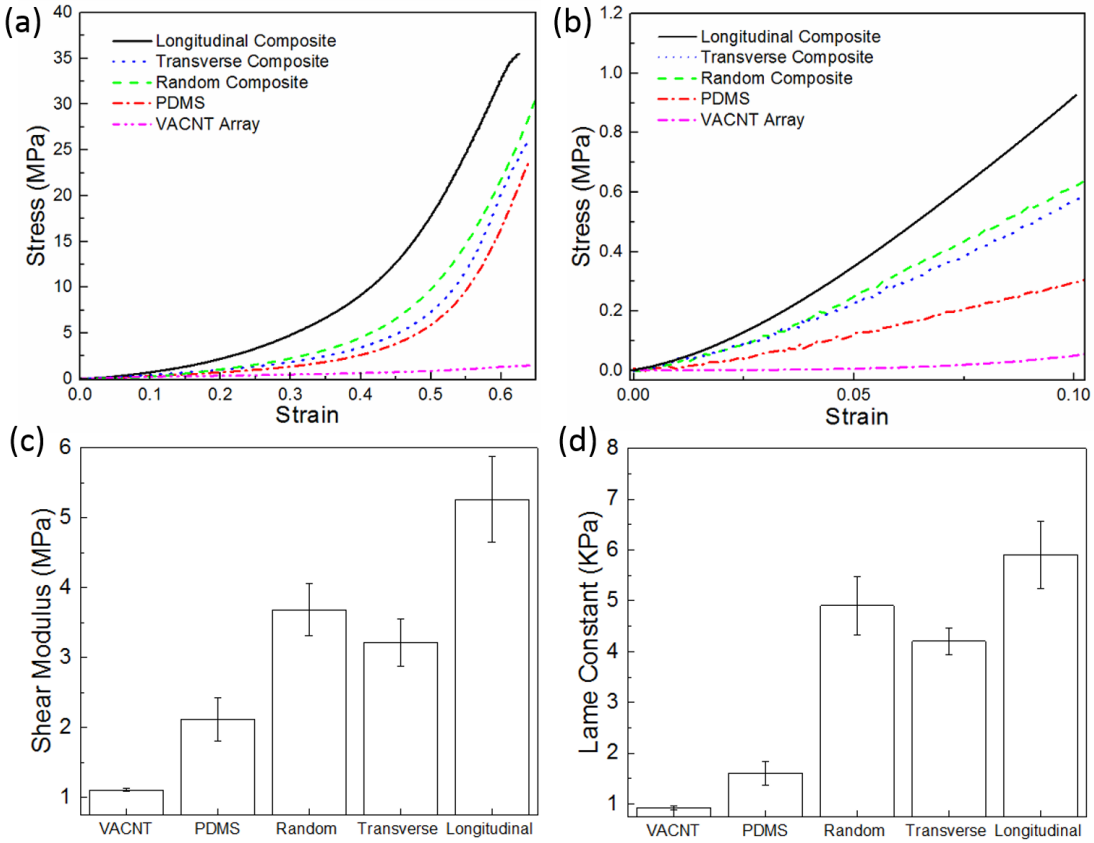


Figure 5.6 Quasi-static compressive stress-strain characterization. (a) Longitudinal composite, transverse composite, random composite, PDMS and VACNT array are compared for their monotonic compressive stress-strain behavior. (b) All samples are compared for the compressive stress-strain response in the low strain region. (c) Shear modulus of all samples from SED modeling. (d) Lam éconstant of all samples from SED modeling.

### 5.3.2 Creep and stress relaxation

The creep testing results are seen in Figure 5.7 with corresponding strain of PDMS and composites in different loading directions, while the stress relaxation testing results were shown corresponding stress of PDMS and composites in different loading conditions in Figure 5.8. Both strain/stress-time response of all samples could be divided into a short initial stage with sharp increase in strain (creep) or decrease in

stress (stress relaxation), and a long plateau stage in which the strain/stress keep constant as shown in Figure 5.7a and Figure 5.8a, respectively. The progressive decrease in stress and increase in strain confirm the time-dependent viscous behavior of viscoelastic materials.

Figure 5.7a shows the creep behavior of four different samples. For elastic response, the representative creep curves show much lower creep compliance of CNT in longitudinal direction than that of PDMS, and moderate creep compliance of random and transverse composites, which confirms the CNT reinforcement effect in longitudinal compression like previous stress-strain test. To understand the viscoelastic response in creep quantitatively, modified four element viscoelastic model was employed with elastic component $E_1$ and viscous component ($E_2$, $\eta_2$). Like the creep curves, the longitudinal composite shows much higher $E_1$ value of 14 MPa, while random and transverse composites show similar $E_1$ value around 3.75 MPa and the student t-test also shows they are not significant different, and PDMS has the lowest value of 2.2 MPa, indicating that the long-time creep response is consistent with the elastic behavior of the CNT composites in quasi-static compression due to gradually vanishing of time-dependent viscous response in a long time period. For the viscous response, PDMS and transverse composites show similar $E_2$ value around 35 MPa, while random composite has a bit lower value of 30 MPa, and all three samples have similar viscous behavior in terms of strain according to student t-test result. And the longitudinal composites have $E_2$ of 170MPa, which is much higher than all other samples, suggesting the remarkable reinforcing effect difference. According to the result of elastic and viscous components, $E_2$ is over order of magnitude higher than $E_1$, showing the viscous response (strain increase with time) is not very significant compared with elastic increase in strain of CNT

reinforced composite, since the strain is proportional to the reciprocal of $E_1$ and $E_2$, respectively. According to $E_2$ and $\eta_2$, retardation time can be calculated by $\tau = \eta_2/E_2$. Among all samples, random and transverse composites show similar retardation time around 59s, while longitudinal composite shows much higher retardation time of 132s, and PDMS has the value of 20s as the lowest viscous response time range. The retardation time has a less difference between longitudinal composites and the other samples. Note that, all samples in creep test can recover back to their original shape and show almost full recovery, so the $\eta_3$ in four element model, which is related to the permanent viscous deformation, can be ignored.

Along with creep, the stress relaxation for anisotropic behavior of CNT polymer composites is summarized in Figure 5.8. The representative stress relaxation curves in Figure 5.8a show that longitudinal composite has much higher relaxation modulus than all other composites, which is consistent with creep test observation, and transverse and random composites has similar relaxation behavior, showing moderate increase compared with PDMS. So, the stress relaxation results confirm that the CNT reinforcement is most effective in the longitudinal composites. In the SLS modeling, $E_1$ represents the elastic response of the viscoelastic behavior, while $E_2$ represents the viscous response. Like creep tests, the longitudinal composite has the highest $E_1$ of 15.5 MPa, while random and transverse composites are in the moderate level around 3.1 MPa and have no significant difference in student t-test, PDMS has the lowest value of 1.65 MPa, exhibiting the effective enhancement of CNT in elastic response. Compared with creep test, we can find the similar $E_1$ values among all tested samples, respectively, respectively, which are expected as $E_1$ represents the elastic response in both models. For viscous modulus $E_2$, longitudinal composite also has the highest

value of 2.3 MPa, while the random and transverse composites have much less modulus around 0.5 MPa, and PDMS has only 0.058 MPa viscous modulus, suggesting that pure PDMS almost has no obvious viscous behavior during stress relaxation and the adding of CNTs leads to remarkable change in viscous response. Further, with the comparison between $E_1$ and $E_2$, $E_2$ is order of magnitude less than $E_1$, which is opposite to the creep results. Since stress is proportional to $E_1$ and $E_2$ in stress relaxation, the viscous response of stress is much less than the elastic response according to $E_1$ and $E_2$, which is consistent with the conclusion on elastic and viscous response relationship in creep test. For relaxation time $\tau$, longitudinal composites have the highest value of 118s and transverse and random composite have the relaxation time of 100s and 80s, respectively, while PDMS has the lowest value around 32s. The composites have much longer relaxation time then pure PDMS, which is consistent with the viscous behavior in creep, while the relaxation time among composites are not significantly different according to student t-tests. In compression, due to the much higher stress level of composite at same strain, it need longer time to release the step load impact for CNTs and polymer within composites.

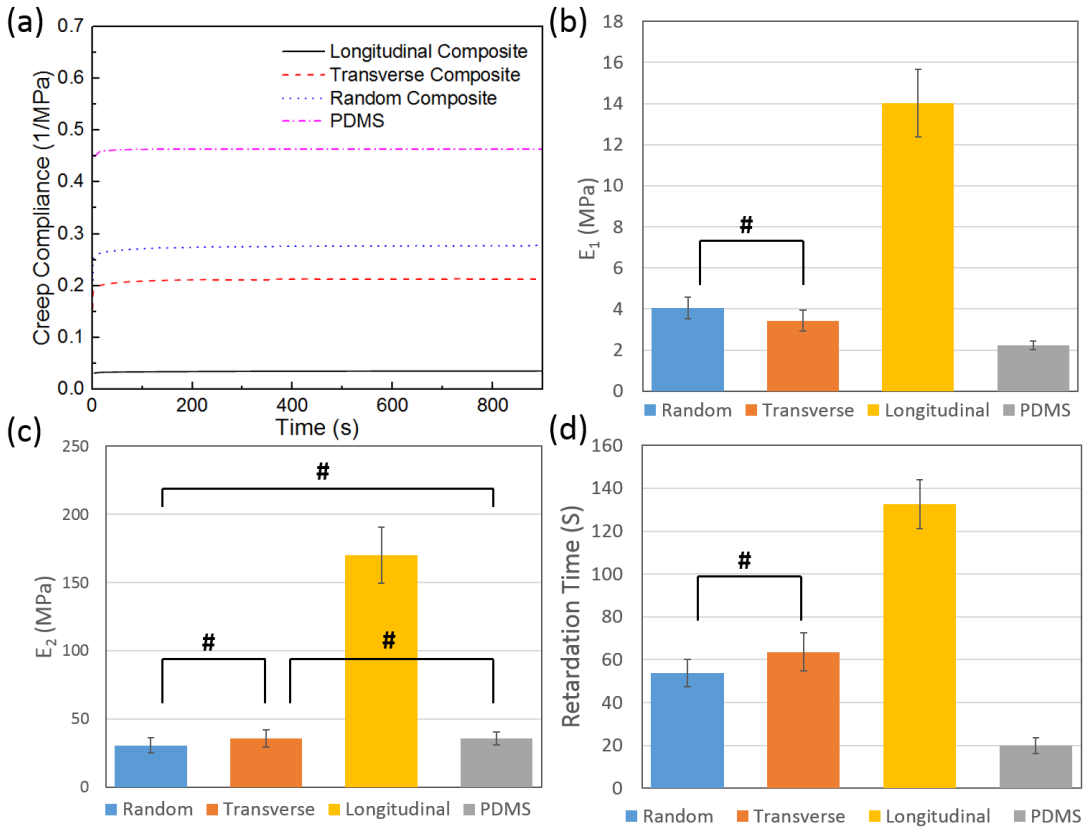


Figure 5.7 Modified four element model characterization on anisotropic creep behavior of PDMS and composites. (a) Strain plots over time in experiments for longitudinal composite, transverse composite, random composite, and PDMS. (b) Creep modulus $E_1$ of four samples in creep test. (c) Viscous modulus $E_2$ of four samples in creep test. (d) Retardation time of four samples in creep test. "#" indicates two tested groups are NOT significantly different in student T-tests ($P_{critical}$=0.05).

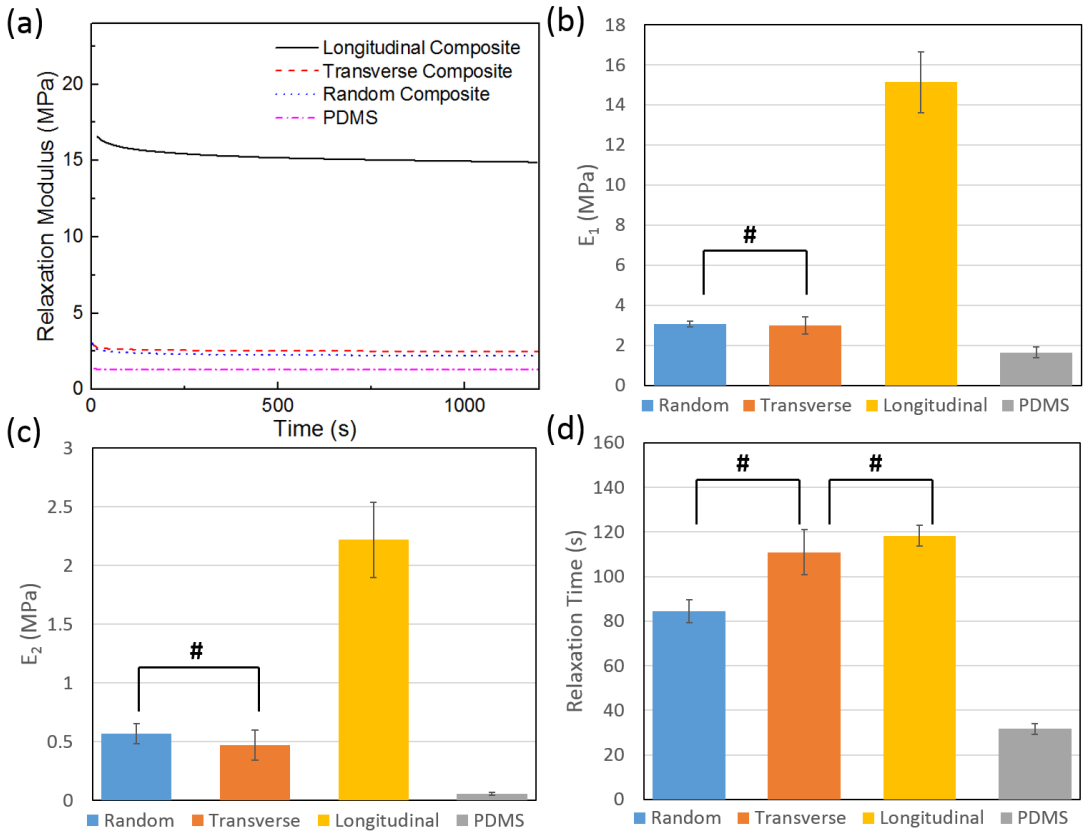


Figure 5.8 Standard linear solid model characterization on anisotropic stress relaxation behavior of PDMS and composites. (a) Stress plots over time in experiments for longitudinal composite, transverse composite, random composite, and PDMS. (b) Relaxation modulus $E_1$ of four samples in stress relaxation test. (c). Viscous modulus $E_2$ of four samples in stress relaxation test. (d) Relaxation time of four samples in stress relaxation test. "#" indicates two tested groups are NOT significantly different in student T-tests ($P_{critical}$=0.05).

### 5.3.3 Dynamic mechanical analysis

In order to understand the anisotropic damping and energy dissipation properties of CNT-PDMS composites, DMA testing across the wide range frequency from 0.1Hz to 10Hz was conducted on longitudinal composite, transverse composite, random composite and PDMS at room temperature. Among them, the storage modulus of longitudinal

composite shows highest value around 16 MPa at 0.1Hz and increases gradually to 20 MPa with frequency. Random composite exhibits similar storage modulus as transverse composite with the value from 2.8 MPa to 4.8 MPa and both of them have moderate increase with frequency, while PDMS shows lowest storage modulus around 2.0 MPa. Among the different samples, the longitudinal composite is order of magnitude higher in storage modulus than PDMS and transverse/random composites, indicating the effective reinforcement of CNT in material stiffness. While frequency increases from 0.1Hz to 10Hz, the storage moduli of all samples have slightly increased, showing frequency dependent behavior. The loss modulus of longitudinal composite has highest value between 2.06 MPa and 4.39 MPa among all samples, and shows moderate increase with frequency. Like storage modulus, the loss modulus of random composite is higher than transverse composite with the value from 0.45 MPa to 1.14 MPa, while the transverse composite has the value from 0.22 MPa to 0.47MPa. Loss moduli of all composite samples have linear increase relationship with frequency, while PDMS has sharp increase when frequency reaches 5Hz, exhibiting a dramatically increased damping capability in high frequency region. Since the storage modulus almost keeps constant during frequency variation, the tan has the same behavior as loss modulus. Among the tan deltas, the random composite shows the greatest tan delta between 0.15 and 0.23 during the compressive cycles, indicating substantial mechanical damping properties. The random composite exhibits up to 400% increase (at 0.1Hz) in the damping capability compared with the pure PDMS and more than 50% (at 0.1Hz) increase for longitudinal and transverse composites. This drastic improvement of damping property can be explained by the buckling and deformation of nanotubes within the composites and the interfacial sliding between nanotubes and matrix [13]. First, when

the composite is compressed, the nanotubes within the composites are buckled and deformed, and when the load is released, due to the resilience of CNT and the recoverability of PDMS, the CNT will rebound and recover back. Since the interaction between CNTs and polymer matrix is van der Waals force, the interfacial friction and slippage can happen, which will dissipate the kinetic energy as friction energy. During repeated loading-unloading process, the frictional energy is rapidly dissipated out of the composites due to the developed local buckling and deforming of nanotubes, and the kinetic energy can be dissipated in a form of heat (or thermal) along with the continuous CNT structure [142]. Therefore, with the superposition of the friction and heat energy dissipation, the CNT reinforced composites show remarkable enhancement in damping capability during compressive cycles. In contrast, the nanotubes in transverse composite only have elastic densification in their radial direction without obvious local buckling and deformation as the low compressive strain (~3%). And the CNTs in longitudinal composites are hard to buckle or deform, because of the exceptional reinforcement effect with better stability and higher resistance to buckling and deformation, which was confirmed by many previous experimental results.

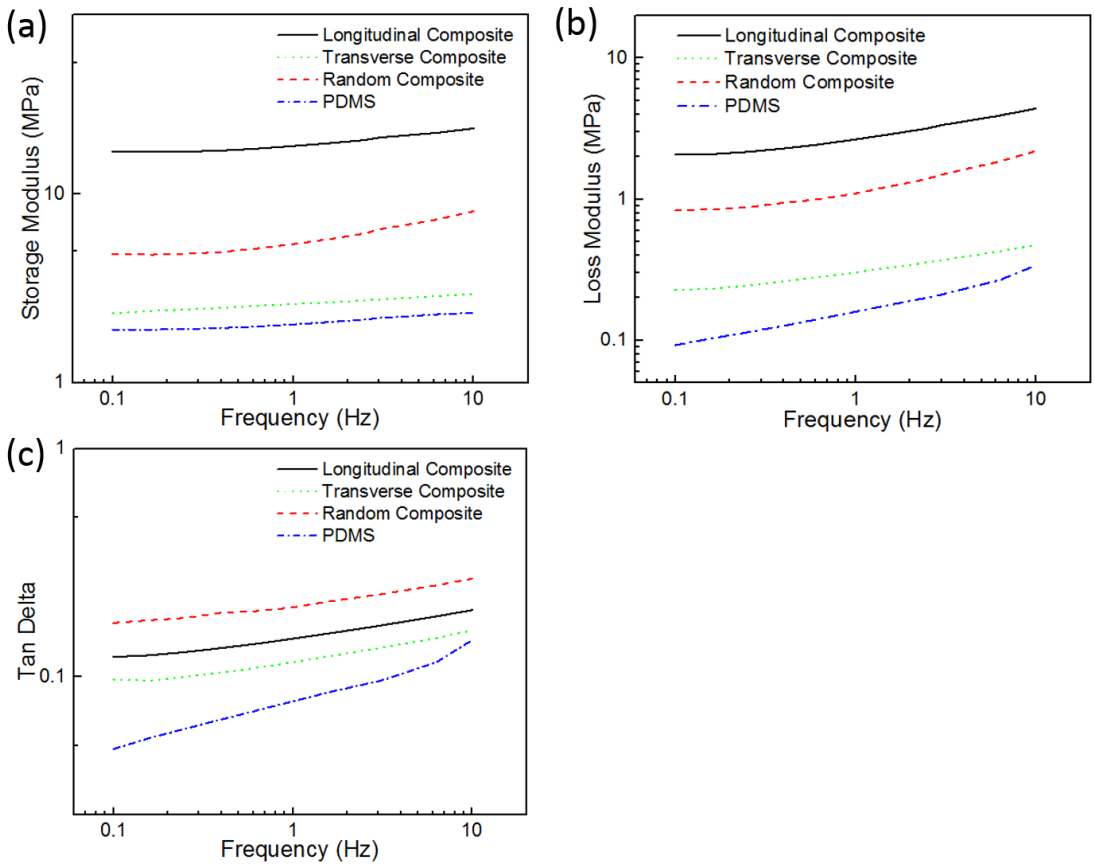


Figure 5.9 DMA characterization results of anisotropic properties of longitudinal composite, transverse composite, random composite, and PDMS. (a) Storage modulus of four samples in DMA compression. (b) Loss modulus of four samples in DMA compression. (c) Tan delta (δ) of four samples in DMA compression.

## 5.4 Conclusions

The anisotropic properties were investigated and compared in this paper, including longitudinal composites, transverse composites, random composites and PDMS. The monotonic compression shows strongly enhanced elastic modulus of longitudinal composites and moderately improved elastic modulus of transverse and random composites, which is the evidence of CNT reinforcement effect. The creep and stress

relaxation were analyzed by viscoelastic models, including modified four element model and standard linear solid model. The quantitative results show the enhancement effects of CNT in elastic component, especially in longitudinal composites, and the remarkable improvement on viscous component of composites. Then, the DMA tests on anisotropic properties were studied. The storage and loss modulus of composites are much higher than PDMS, and the damping effect of composites is significantly increased by the interfacial sliding between nanotubes and matrix and the energy dissipation in thermal transmission through nanotubes.

# Chapter 6

# FATIGUE CHARACTERISTICS OF CNT REINFORCED POLYMER COMPOSITE

## 6.1 Background

In previous studies, we unveiled the mechanical and viscoelastic properties of continuous CNT reinforced composites and investigated the anisotropic properties as well. And the enhancement of mechanical properties was also observed, such as elastic modulus [143], tensile strength and damping capability [144]. However, the performance in engineering application is also a matter of material's durability and the long-term performance. Especially, the fatigue properties of CNT reinforced composites are critically important in the future application, such as damping cushion and energy absorbing material. As it is known, fatigue is one of the primary reasons for failure in many structural materials under cyclic loading condition and the material will exhibit gradual degradation and decrease of their mechanical and structural properties as a result of damage and crack accumulation.

Recently, there are some preliminary research on the fatigue behavior of CNTs and CNT-polymer composites. For instance, the study [12] on fatigue resistance of continuous vertically aligned CNT arrays shows no fatigue failure at high strain amplitudes up to million cycles. The fatigue performance of CNT-PMMA/ABS composites were characterized and compared in tensile load [145] and the results show that significant increase in fatigue life of CNT reinforced composites may be attributed to the direct interaction mitigating micro-damage/crazing failure. Similar

improvement on high-cycle fatigue strength were observed in CNT glass fiber-epoxy composite experiment [146], and the reasons can be concluded as the creation of much more nucleation sites for fatigue crack as well as possible crack bridging by the CNTs. Also, the fatigue behavior of unidirectional SWCNT reinforced epoxy composite [147] shows much higher cyclic stress and indicates that the CNT ropes have good potential for fatigue resistant due to the good adhesion between nanotubes and polymer matrix. And the fatigue life was significantly extend with the incorporation of nanoclay to CFRP composite [148] since the interfacial bonds between nano-structure and matrix effectively suppressed the growth of damage crack area.

But, there are few studies which are devoted to the fracture and the long-term fatigue performance of continuous CNT reinforced composites under compression. So, an understanding of the fatigue resistance of continuous CNT reinforced composite will enable the potential of CNTs to be better realized for engineering structural and functional materials. In this study, the fatigue behavior of continuous VACNT polymer composite was investigated and compared with pure PDMS.

## 6.2 Methods and Materials

### 6.2.1 Continuous CNT-PDMS composite fabrication

Like section 4.2.1, the CNT-PDMS composite was made by direct infiltration method. The PDMS (a mixture of resin and hardener at a volume ratio of 10:1) was put in vacuum chamber first to get rid of air bubbles. The VACNT array sample was set on a stage connected to vacuum pump, and the droplets of PDMS were delivered to the top surface of VACNTs one by one, and each droplet was sucked into the VACNT arrays

within several to tens of minutes. The infiltration became slower as more PDMS droplets were delivered until saturation. After the infiltration process was completed, the sample was put in a vacuum chamber to further get rid of air bubbles within the PDMS. Then the composite sample was placed in an oven at 100°C overnight to allow full curing.

The resultant composites consist of continuous CNTs as reinforcement and the PDMS as matrix in a cubic block shape (~1.5×1.5×1.5mm$^3$). The content of CNT in composite was measured by micro-balance for the weight of CNT arrays and composite, respectively. The mass loading of CNTs in this composites was around 10.1wt%. Assuming the density of MWNT 2.2g/cm$^3$ [110], the estimated volume fraction of nanotube was around 4.9%.

### 6.2.2 Cyclic fatigue tests

The compressive cyclic fatigue tests were conducted according to the specification, ASTM D7791 and E606, on a universal testing machine (Instron E3000). The tests were conducted at room temperature on a displacement control mode with constant-amplitude sine-wave loading. To determine the fatigue properties, the maximum strain levels were kept at 25%, 35%, 45%, 55% and 65% strain of PDMS and then the corresponding stresses were calculated and the fatigue tests with identical stress were performed on CNT polymer composites, respectively. A test frequency of 1Hz was used which was low enough to minimize the effect of adiabatic heating.

The curve of strain versus number of cycles to failure (S-N) was used to examine fatigue resistance, in order to precisely define the fatigue life of the CNT reinforced composites in compression, a perceptible decrease (10%) of the measured

maximum stress was assumed to be a sign of fatigue failure according to ASTM D7791, which can be considered as an intrinsic property change. Typical fractured specimens were chosen and were sputter-coated with gold layer. Then, the scanning electron microscopy (SEM) was used to examine the surface morphologies of the specimens after fatigue to identify the failure mechanisms.

## 6.3 Results and Discussion

### 6.3.1 Cyclic stress-strain behavior

The cyclic stress responses were measured at a constant compressive strain level around ~40% of CNT-PDMS composites as a function of the number of cycles. The induced stress strain curves (Figure 6.1a) clearly show two distinct paths corresponding to the loading and unloading trace, generating hysteresis loops and indicating the potential damping capacity. Similar to the behavior observed in polymer material, hysteresis in the composites during compressive cycles could result from the interaction between nanotubes and polymer matrix [144] and also the polymer chain change of the matrix. During loading process, the continuous CNTs will deform and buckle to some extent along with the matrix deformation. Since the interaction between CNTs and polymer matrix is van der Waals force, the interfacial friction and slippage can happen with rapidly absorbing impact energy from polymer matrix through surrounding interfacial area. Then, on the unloading process, nanotubes recover back to their original position with outstanding resilience and the energy can be dissipated through nanotube structure by heat conduction. In addition, the feasible polymer chain change within PDMS during the cyclic loading can also contribute to

the hysteresis behavior [149, 150], while the energy is absorbed by the matrix when rearrange the molecular chain distribution. Therefore, this energy dissipation mechanism during loading and unloading process can result in the observed remarkably hysteresis loop.

In terms of time effects, a gradually decrease in maximum stress can be observed in Figure 6.1b. During the 1st cycles, the stress response was measured to be 7.64MPa, but the 10th cycle stress decreases down to 7.54MPa, and the stress of 100th cycle is only 7.40MPa, showing that the induced stress response has gradually decreased. The similar behavior was observed in our previous experiments on VACNTs [12], and this stress softening behavior is extensively observed in polymer material and rubber compression in many experiments and modeling [151-154], which is known as Mullins' effect [155], where the samples under cyclic strain controlled loading require a lower and lower load. And the further cycling load have continued softening behavior at a progressively slower rate and a steady state may be reached after then. This stress softening phenomenon is an important indication of the amount of energy that the material can continue to absorb and dissipate.

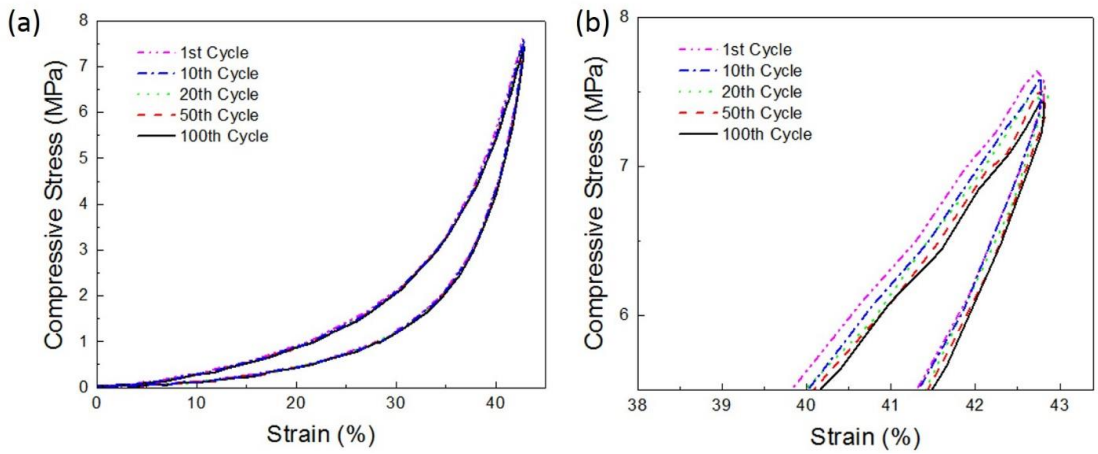


Figure 6.1 Hysteresis elastic behavior of CNT-PDMS composites. (a) Stress-strain curves under compression in different cycles. (b) Enlarged stress-strain curves in high strain region, elucidating the gradually decreased maximum stress level.

The stress softening effect may arise from the compound effects, including the polymer phase effect and the interaction between CNT and matrix. Firstly, the polymer matrix may change under repeated loading with relocating and reordering of polymer chains. Since the long feasible polymer chain within PDMS can freely translate and has good local mobility, the cyclic loading in compression can rearrange the initial polymer chain distribution, and the material reaches equilibrium conditions at the imposed loading condition with number of subsequent cycles. And there are many explanation [153, 154, 156-160] for Mullins effect according to the soft phase change, including the retarded response of network chains, the incomplete recovery of the cross-linked network to its initial random state, dissipative microstructures, such as clusters of chain molecules held together by interatomic forces and molecular chain entanglements, and so on. Another important aspect is the interaction between CNTs and polymer matrix. Like the hysteresis behavior, the interfacial connection between nanotubes and polymer matrix is critical in compressive response during cyclic load. In compression, the cracks on interface between CNTs and matrix can accumulate

with repeated loading and result in fracture of weak bonds between the polymer and nanotubes, and then the detachment of elastomer matrix and CNTs. Without the strength of matrix support, the compressive resistance will become weak and the compressive stress will decrease gradually. From the observations above, it can be conjecture that crack and damage accumulation along the PDMS/CNT interface is also responsible for the stress softening effect. So, a stronger bonding between the polymer and nanotube in the interfacial region would lead to a higher compressive stress, and such interfacial condition would account for the sample's compressive resistance and fatigue behavior under dynamically loads.

### 6.3.2 Fatigue life

Fatigue life data for CNT-PDMS composites under longitudinal loading (longitudinal composite) and transverse loading (transverse composite) and pure PDMS samples are shown in Figure 6.2. With applied stress increases, the alternating fatigue life decreases appreciably from $10^5$ to $10^3$ in all tested samples, suggesting that the composite and PDMS resistance to applied loading will degrade as a result of fatigue. Among the different tested samples, a significant increase in the number of load cycles to failure for each loading condition was observed for the CNT-reinforced composite, especially at high cycle regime (low strain level). For instance, the transverse composite didn't show stress degrade until $2.6\times10^5$ cycles at the stress around ~3.15 MPa, while the PDMS only shows $1.4\times10^5$ cycles for fatigue life, and the longitudinal composite samples do not showed any significant decrease in maximum stress up to $5\times10^5$ cycles, which is the highest number of cycles for our test. These show significant improvements in the high-cycle fatigue life of CNT polymer

composites, with more than 1.8 times of fatigue life increase and provide an opportunity to utilize polymer composites in high-cycle fatigue applications by adding CNTs as reinforcement. In low-cycle regime with high applied stress, all materials show order of magnitude decrease in fatigue life from $10^5$ down to $10^3$. The cycles of failure of both longitudinal and transverse composites in low-cycle regime (at ~13.7 MPa) are remarkably limited around $5 \times 10^3$ cycles, which are only around $1 \times 10^3$ cycles higher than the fatigue life of PDMS, indicating that at low cycle regime (high stress level) the CNTs are less effective in suppressing the rapidly propagating damages and cracks. The transverse composites show an improved fatigue resistance than PDMS, which comes from the CNT enhancement in elastic modulus and the nanotube obstacle on the fatigue crack nucleation and propagation in the composites. Compared with transverse composite, CNTs in longitudinal composite can more effectively hinder the crack propagation, which generally develops in the transverse direction (perpendicular to the loading direction) in longitudinal composite, so the improvement in fatigue resistance of longitudinal composite is expected to be better than transverse composite.

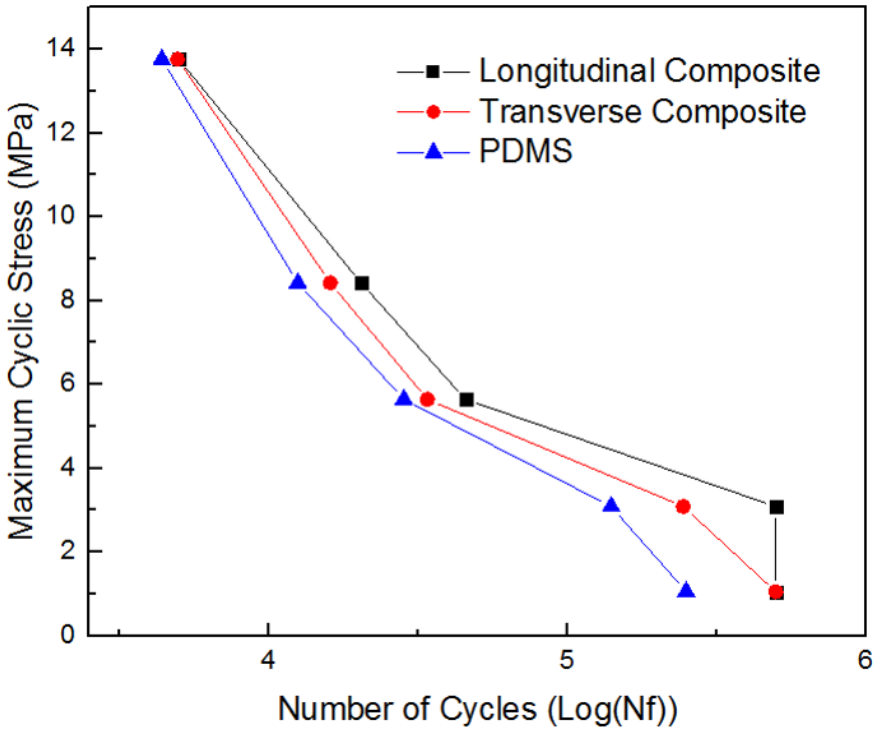


Figure 6.2 Applied cyclic stress versus number of cycles to failure of longitudinal, transverse composite and PDMS.

From the previous S-N curves, the difference between high and low cycle regime fatigue behaviors need further investigation, and an instantaneous stress-number of cycle curves at low and high stress levels can provide much clear detail for the difference. As shown in Figure 6.3, the stress response at low cycle regime decrease much faster than the high cycle regime stress, and the high cycle curves can reach equilibrium condition after tens of thousands cycles, while the low cycle curves keep decreasing during the same cycle period. The different enhancement effects of CNTs on fatigue life between low and high cyclic stress levels may be explained by considering the failure mechanisms in polymer first. According to the classical fatigue theory [161], the fatigue failure of material is related to the nucleation and growth of

damage or crack in the polymer matrix, and that damage in the matrix was found to be an accurate measure [146, 162-164] of the fatigue strength of the composite. With cyclic loadings, polymer matrix damage is created in the initial stage within a few cycles. Then, as cyclic stress continuous, the damage in the form of closely spaced cracks, propagates on several fronts until structural failure happens. The damage crazes significantly and extensively with rapid speed at high stress level, while at low stress levels, the damage and cracks in the matrix are pretty limited and widely propagate slowly until failure occurs. So, there will be remarkable difference in the S-N response between low and high stress loading conditions.

In CNT polymer composite, by associating with the stress softening effect in previous section, the damage and crack nucleating and propagating in the interface area between nanotubes and polymer matrix could be the priority for final fatigue failure. With repeated cyclic compression, the damages on interface can create easily and accumulate rapidly, which in long term will result in the debonding of the polymer and nanotubes and then the structural collapse and fracture in bulk CNT polymer composite. With the combination of interfacial debonding and the fatigue failure mechanisms described above [146, 161], the different effectiveness of CNTs at low and high cyclic stress levels can be explained properly. At high stress levels, the damage and cracks occur at several fronts and at a rapid rate, especially in the CNT-polymer interface area. During this process, the CNTs in the path of the crack propagation cannot slow down the crack developing remarkably, since the high stress intensities at the crack tips can overcome these obstacles in a few cycles. At low stress levels, however, the damages and cracks took significantly longer time to coalesce and propagate to form big enough critical fracture, and the CNTs effectively enhanced the

crack growth resistance by their continuous structure and the obstacle in the crack propagation path.

In addition, the CNT reinforced composites have higher elastic modulus and consequently will undergo lower strain at same stress level. From previous stress-strain tests of CNT reinforced composites, the longitudinal composite has the highest stiffness in all strain region and the transverse composite has a moderate increase in stiffness, while the pure polymer matrix has much lower value. So, this stiffness enhancement effect could also result in relatively lower compressive amplitude for composites and could increase the fatigue life significantly in longitudinal composite and moderately in transverse composite. Note that at low stress level, CNT reinforcement is even more significant than that at high stress level, causing better improvement in fatigue life at low stress level. Also, for a given level of strain energy (a given cyclic load amplitude), a larger density of nano-scale cracks in composite containing CNTs will grow more slowly than the lower density in pure polymer [146], due to the conservation of energy, which will lead to an increase in the number of cycles required for initiation, growth, and coalescence of cracks and damages, resulting in the enhancement of high-cycle fatigue life.

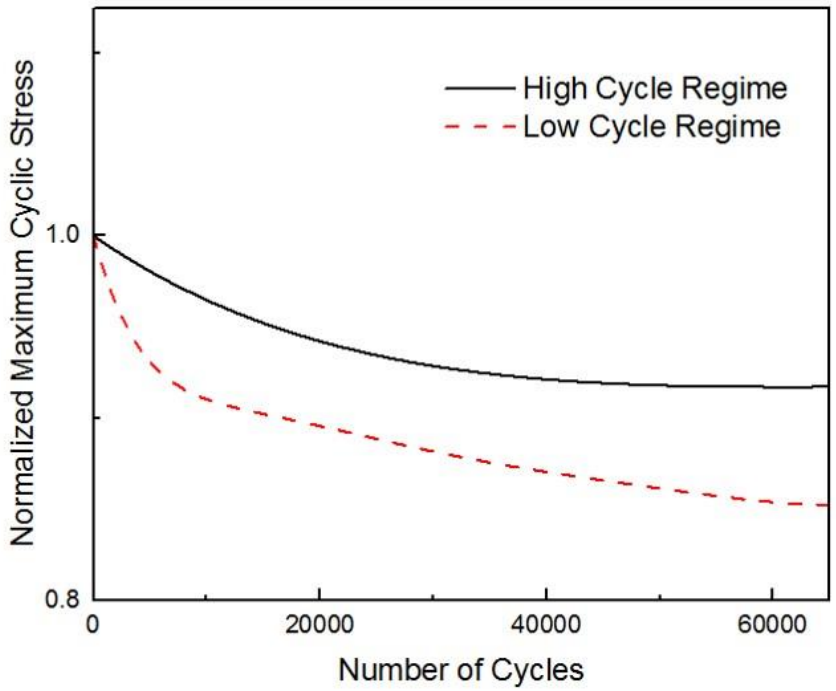


Figure 6.3 Compressive stress response at a constant strain amplitude with respect to number of cycles. S-N response of high cycle regime (low stress level) and low cycle regime (high stress level).

### 6.3.3 Surface analysis after fatigue test

The SEM characterization was used to investigate the fatigue failure mechanism after cyclic compression test. Not like the fracture results in most tensile fatigue tests, most of the composite and PDMS samples under compression don't fracture or collapse after long time cyclic loadings, especially in low stress compression. Because the fatigue failure criteria is 10% decrease in stress level, there are only some samples show significant fracture and structural collapse in high stress level (corresponding to 65% strain in PDMS). High-resolution SEM of the intersecting surface of longitudinal composites are shown in Figure 6.4a-b. SEM image shows the buckling and deformation of nanotube polymer bundles under longitudinal

compression, resulting in the detachment between CNT bundles and polymer matrix. In Figure 6.4b, the continuous CNT bucking and debonding were observed within the bundles in high resolution images, serving to dissipate strain energy, and the numerous continuous nanotube structures can effectively blunt and delay the crack tips, which develop in transverse direction. During cyclic compression, CNTs can mitigate crack growth by slowing craze coalescence prior to crack propagation, while the nanotube bundle can potentially slow crack growth and absorb strain energy by debonding from the surrounding matrix, which confirms the analysis in previous section. In transverse composite fatigue test, there is only elastic compression of nanotube and matrix in longitudinal direction (loading direction), so no significant buckling behavior was observed in Figure 6.4c-d. The microscopic images show only interfacial fracture for the whole region in transverse direction and the nanotube bundles don't show significant detachment or deformation. Note that the nanotube polymer bundles have certain downward plastic deformation as shown in Figure 6.4d, resulted from large compressive deformation during the repeated loading and unloading process. There are also numerous small buckling half waves in transverse direction in Figure 6.4d, caused by the repeated transverse shrink and expansion of composites due to the Poisson effect, which could transform the longitudinal compression into transverse expansion. Some cracks can be seen among nanotube polymer bundles and they propagated and developed along with the interval area among nanotube bundles in transverse direction. According to the crack nucleation and development mechanism [161], the transverse distributed continuous CNT structure cannot efficiently hinder the damage or crack developing, which develop transversely in matrix regions among the nanotube bundles. So, this makes transverse composite fatigue as similar as

polymer fatigue and results in a lower increase in fatigue life. In addition, due to the moderate stiffness reinforcement, the cyclic amplitude of transverse composites is much higher than longitudinal composite to reach same stress level, leading to lower fatigue resistance life consequently.

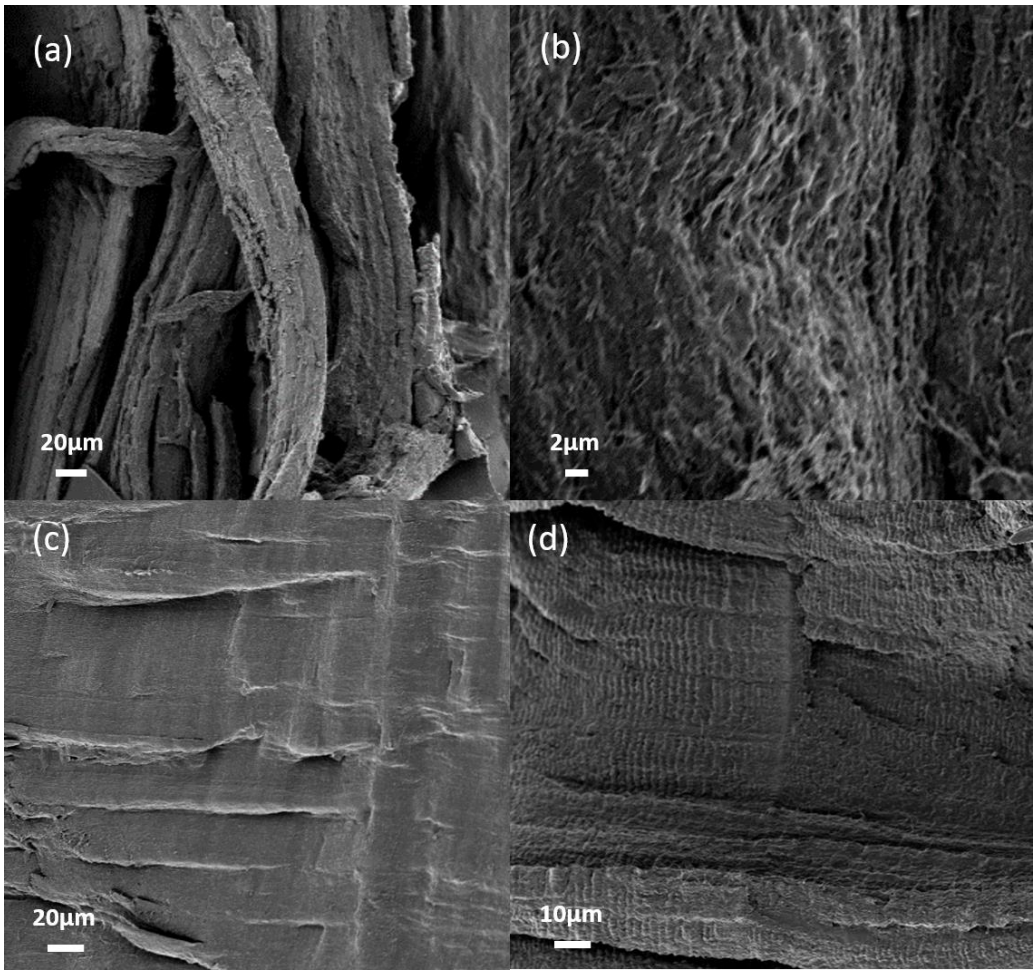


Figure 6.4 SEM images of CNT-PDMS composite fracture surface after fatigue test. (a) SEM image of longitudinal composites with fracture and debonding of nanotube polymer bundles. (b) The high resolution SEM on the interfacial region between CNT and polymer matrix of longitudinal composites. (c) SEM image of transverse composites with fracture surface and the interface of nanotube polymer matrix. (d) The high resolution SEM image

of the interfacial region between CNT and polymer matrix of transverse composites.

## 6.4 Conclusions

The fatigue resistance of CNT-PDMS composites were investigated and compared in this chapter. The adding of CNT to the polymer matrix improved their fatigue life considerably, especially in high-cycle fatigue strength. During cyclic compression, both PDMS and composite show stress softening response, which could be the underlying reason for further fatigue failure. And the composites showed energy-absorbing mechanisms that may be another aspect for the increase in the fatigue life, including the hindering of crack propagation and the CNT-matrix interfacial debonding, along with the CNT reinforcement effect in stiffness. Also, the anisotropic fatigue properties of CNT polymer composites were investigated with longitudinal and transverse composites, showing different fatigue resistance and different fracture and crack mechanism. These results indicate a significant increase in crack energy absorption during crack initiation, coalescence, and propagation, resulting in the observed increase in the fatigue life when CNTs are added, making CNT polymer composites more durable in applications involving damping and energy absorption.

# Chapter 7

## CONCLUDING REMARKS AND FUTURE WORK

In this thesis, contributions have been made to advance the evaluation of mechanical characteristic of CNTs and CNT polymer composites:

1. Compressive characteristic: The local buckling behavior of VACNT arrays was characterized experimentally and interpreted properly by employing the lateral support by van der Waals interaction between nanotubes. Likewise, the intrinsic CNT property effects on mechanical properties of VACNT arrays under compression were characterized by experiments and analyzed by employing the SED function model with statistical method.

2. Viscoelastic characteristic: Creep and stress relaxation tests with stress and strain variation were conducted and power law viscoelastic models were employed to quantify the viscoelastic material properties. Then, the dynamic viscoelastic properties were characterized by DMA test with frequency variation. Also, the temperature effects on the viscoelastic properties were investigated by employing time-temperature superposition (TTS) approach.

3. Anisotropic characteristic: The quasi-static compression and viscoelastic characterization, including creep, stress relaxation and DMA, were conducted on longitudinal, transverse and random composites and PDMS for comparison. By employing linear viscoelastic models, viscoelastic material constants were derived and compared with each other for static viscoelastic properties and storage/loss modulus were analyzed for dynamic viscoelastic properties.

4. Fatigue characteristic: The cyclic compressive fatigue tests on longitudinal, transverse CNT reinforced composites and PDMS were performed and the stress-number of cycle's data was obtained. The stress softening behavior was observed and analyzed by considering polymer matrix change and nanotube-matrix interaction. Furthermore, the fatigue failure mechanism was investigated and analyzed with interface debonding between nanotubes and matrix according to SEM characterization.

## 7.1 Concluding remarks

Some of the key observations from this work are as follows:

**Compressive properties of VACNT arrays**

The local high-mode buckling behavior of VACNT arrays under compression was characterized experimentally and interpreted properly by employing the van der Waals interaction between VACNTs as lateral support. With the lateral support of van der Waals interaction, the buckling of VACNTs becomes local buckling with many half buckling waves and the propagation of such buckling waves starts from the bottom of the nanotube arrays. And developing mechanism of buckling follows the wave damping effect, which is widely observed in shell buckling.

Furthermore, the structure and morphology of VACNTs were characterized by SEM, TEM and Raman spectrum and the stress-strain behavior of VACNT arrays has been quantified by strain energy density function. In order to study the influence of CNT intrinsic properties on mechanical properties, the material constants from modeling were statistically analyzed by taking the structural and morphological properties into account. And the results show that the effects of structure and morphology of VACNTs on the mechanical properties are significant in compression and density and defect degree have the most important effect on material properties.

**Viscoelastic properties of CNT reinforced polymer composites**

The static and dynamic viscoelastic characterization were conducted on CNT reinforcement composites and PDMS, respectively. The stress variation of creep and strain variation of stress relaxation show the nonlinear viscoelastic behavior of PDMS and CNT-PDMS composite, and the mathematical power-law modeling provides mathematical qualification for the nonlinear viscoelasticity. The results indicate that the CNTs have effective enhancement in elastic response in creep and stress relaxation tests, and shows different response of stress/strain rate of two materials, suggesting the influence of CNTs in changing the viscosity of the composite.

The temperature effects were then investigated. As temperature increases, both materials show almost constant elastic modulus or slightly stiffening modulus, which is observed and explained as "rubbery plateau region". And the composite shows much better stability in temperature variation due to CNT filling. Also, the WLF constants were solved so that the results can be shifted to any desirable temperature according to time-temperature superposition. Furthermore, the frequency-temperature response of CNT-PDMS composite and PDMS was investigated in DMA tests. As frequency increases, the storage modulus increases slightly and the loss modulus showed quasi-linear increase with frequency. And the temperature effect on both PDMS and CNT-PDMS composite can be neglected in storage modulus, while the loss modulus has moderate decrease with temperature. The WLF constants were solved so the results can be shifted to any reference temperature to determine the dynamic viscoelastic response.

### Anisotropic Properties

The anisotropic properties of CNT polymer composites were investigated and compared, including longitudinal composites, transverse composites, random composites,

VACNT arrays and neat PDMS. The monotonic compression shows very high elastic modulus of longitudinal composites and moderate elastic modulus of transverse and random composites, which was evidence of CNT reinforcement effect. The creep and stress relaxation were characterized by linear viscoelastic models, including modified four element model and standard linear solid model, and the results show the enhancement in elastic behavior of CNT as filling material, especially in longitudinal composites, and the influence of CNT in changing the viscous response of composites.

The DMA test on anisotropic properties were also investigated. The storage and loss modulus of composites are much higher than PDMS, and the damping effect of composites is significantly higher than PDMS. According to tan delta of composites, the difference among longitudinal, transverse and random composites can be explained by the interfacial sliding between nanotubes and matrix and the energy dissipation in thermal transmission through nanotubes.

### Fatigue

The fatigue resistance of CNT reinforced composites and PDMS was investigated and compared. The adding of CNT to the polymer matrix improved the fatigue life considerably, especially in high-cycle fatigue behavior. The results indicate a significant increase in crack energy absorption during fatigue crack initiation, coalescence, and propagation. During cyclic compression, both PDMS and composite show stress softening response, which could be the underlying reason for further fatigue failure. And the other important aspect is the interaction between nanotubes and polymer matrix, including the hindering of crack propagation from dense nanotubes and the energy-absorbing from CNT-matrix interface debonding. And the anisotropic fatigue properties of CNT polymer

composites were investigated with longitudinal and transverse composites, showing different fatigue resistance and different fracture and crack mechanism.

## 7.2 Suggested future work

This dissertation covered several novel aspects of CNTs and CNT reinforced composites, including fabrication, characterization and analysis. Even though they are presented as individual chapter, in a higher horizon, all are inter-related when it comes to the applications of the CNTs and CNT composites. Depending on the type of applications, appropriate CNT synthesis technique should be employed and all necessary nanotube properties have to be characterized and analyzed. Therefore, the full understanding of the mechanical characteristics of CNTs and CNT polymer composites will enable us to further fabricate and utilize new nanotube hierarchical structures so as to establish novel solutions to ultimately create bio-mimicking artificial skins.

For CNT and CNT arrays research, the continuous CNT synthesis is critical and the access of ultra-long vertically aligned or spinning nanotube structure is desired for numerous engineering applications. Therefore, the techniques to synthesize nanotube with longer length and less defects have to be investigated. Suitable growth techniques with proper fabrication parameters have to be developed, including the substrate, carbon source and hydrogen speed ratio, reaction temperature and so on. The experimental specific parameters could lead to different CNT properties and provide insight into the relevant excitations.

For CNT polymer composite research, one important aspect is the interaction between nanotube and matrix. In this dissertation, the polymer was infiltrated into nanotube by in situ polymerization process and the connection between nanotube and matrix is van der Waals force. Thus, further work can be focused on covalent functionalization and surface chemistry of nanotube. Chemical functionalization of the nanotube surface is expected to resolve the lack of interfacial bonding problems. But, with the covalent chemical bonding, the mechanical properties of CNT may be reduced, which should be considered and compromised in order to achieve the optimization of mechanical property of CNT polymer composites.

In terms of CNT and composite mechanical properties, especially the viscoelastic properties, our work is mainly based on experimental characterization and analytical modeling. Since analytical studies on the mechanism of load transfer between the matrix and nanotubes are not enough, the corresponding finite element modeling analysis can be utilized for the viscoelastic behavior of nanotube/polymer composites under compression. And the interfacial boundary condition between nanotube and matrix can be altered and simulated according to the CNT and matrix connection.

To explore the composites with continuous nanotube reinforcement for potential use as artificial skins in engineering applications, the further study on the similarity and compatibility between bio-skin (e.g. dolphin skin) and CNT polymer composite are necessary and imperative, especially on the mechanism of viscoelasticity for viscous damping and friction reduction. Since the proposed artificial nanotube reinforced skin can offer excellent passive damping, friction drag reduction and energy efficiency, the further study on CNT reinforced polymer composites as

damping materials will substantially contribute to the field of new material in energy efficiency.

## 7.3 Summary

The work presented in this dissertation expands the scope of understanding of CNT arrays and CNT reinforced polymer composites in determining the mechanical properties for a wider range of future applications. Furthermore, it provides predictions and guidelines to the experimentalists regarding proper utilization of the future CNT filling composite materials.

The work opens up opportunities for future researchers to expand the utility of CNT and CNT based material for engineering application of a wide expansion of material systems.

## REFERENCES


[1] Iijima. helical microtubules for graphitic carbon. Nature. 1991;354:2.
[2] Ajayan P, Lijima S. Smallest carbon nanotube. Nature. 1992;358:23.
[3] Ajayan P. Nanotubes from carbon. Chemical reviews. 1999;99(7):1787-800.
[4] Waters JF, Riester L, Jouzi M, Guduru PR, Xu JM. Buckling instabilities in multiwalled carbon nanotubes under uniaxial compression. Applied Physics Letters. 2004;85(10):1787.
[5] Yap HW LR, Carpick RW. Negative stiffness and enhanced damping of individual multiwalled carbon nanotubes. Phys Rev B. 2008;77:6.
[6] Yu MF LO, Dyer MJ, Moloni K, Kelly TF, Ruoff RS. Strength and breaking mechanism of multiwalled carbon nanotubes under tensile load. Science. 2000;287:4.
[7] Thostenson ET, Chou T-W. Nanotube buckling in aligned multi-wall carbon nanotube composites. Carbon. 2004;42(14):3015-8.
[8] Moniruzzaman M WK. Polymer nanocomposites containing carbon nanotubes. Macromolecules. 2006;39:11.
[9] Ajayan PM SJ, Koratkar N. Utilizing interfaces in carbon nanotube reinforced polymer composites for structural damping. J Mater Sci. 2006;41:5.
[10] Thostenson E, Li C, Chou T. Nanocomposites in context. Composites Science and Technology. 2005;65(3-4):491-516.
[11] Collins PG AP. Nanotubes for electronics. Scient Am. 2000;283(6):7.
[12] Suhr J, Victor P, Ci L, Sreekala S, Zhang X, Nalamasu O, et al. Fatigue resistance of aligned carbon nanotube arrays under cyclic compression. Nature nanotechnology. 2007;2(7):417-21.
[13] L. Ci JS, V. Pushparaj, X. Zhang, P.M. Ajayan. Continuous carbon nanotube reinforced composites. Nano Letter. 2008;8:4.
[14] Cao A, Dickrell PL, Sawyer WG, Ghasemi-Nejhad MN, Ajayan PM. Super-compressible foamlike carbon nanotube films. Science. 2005;310(5752):1307-10.
[15] Wei BQ, Vajtai R, Ajayan PM. Reliability and current carrying capacity of carbon nanotubes. Applied Physics Letters. 2001;79(8):1172.
[16] Pushparaj VL, Ci L, Sreekala S, Kumar A, Kesapragada S, Gall D, et al. Effects of compressive strains on electrical conductivities of a macroscale carbon nanotube block. Applied Physics Letters. 2007;91(15):153116.
[17] A. Misra JRR, L. De Nardo, A.E. Craig, C. Daraio. Synthesis and characterization of carbon nanotube multilayer structures. ACS Nano. 2011;5(10):8.
[18] Yunus EM SS, McBride JW. Investigation of gold sputter coated vertically aligned multi-walled carbon nanotubes for RF MEMS contact surfaces. In Microelectromechanical Systems-Materials and Devices II. 2009.

[19] Ebbesen T, Ajayan P. Large-scale synthesis of carbon nanotubes. Nature. 1992;358(6383):220-2.
[20] Carbon Nanotube Structure Retrived from https://www.google.com/search?q=carbon+nanotubes&rlz=1C1CHFX_enUS605US608&espv=2&biw=1920&bih=911&source=lnms&tbm=isch&sa=X&ved=0ahUKEwjXypXMvb_MAhWilYMKHfwTCrsQ_AUIBygC#imgrc=-njj0njGdVwVMM%3A.
[21] Andrei Eliseev, Lada Yashina, Marianna Kharlamova and Nikolay Kiselev (2011). One-Dimensional Crystals inside Single-Walled Carbon Nanotubes: Growth, Structure and Electronic Properties, Electronic Properties of Carbon Nanotubes, Prof. Jose Mauricio Marulanda (Ed.), InTech, DOI: 10.5772/19060.
[22] Carbon Nanotube TEM Images Retrived from http://cnx.org/contents/1096167b-8518-4159-a88d-3b2ae4df6645@9.4:51/Chemistry_of_Electronic_Materi.
[23] Puretzky A, Geohegan D, Fan X, Pennycook S. In situ imaging and spectroscopy of single-wall carbon nanotube synthesis by laser vaporization. Applied Physics Letters. 2000;76(2):182-4.
[24] Ren Z, Huang Z, Xu J, Wang J, Bush P, Siegal M, et al. Synthesis of large arrays of well-aligned carbon nanotubes on glass. Science. 1998;282(5391):1105-7.
[25] Che G, Lakshmi B, Martin C, Fisher E, Ruoff RS. Chemical vapor deposition based synthesis of carbon nanotubes and nanofibers using a template method. Chemistry of Materials. 1998;10(1):260-7.
[26] Endo M, Takeuchi K, Kobori K, Takahashi K, Kroto HW, Sarkar A. Pyrolytic carbon nanotubes from vapor-grown carbon fibers. Carbon. 1995;33(7):873-81.
[27] Treacy M, Ebbesen T, Gibson J. Exceptionally high Young's modulus observed for individual carbon nanotubes. Nature. 1996;381:678-80.
[28] Overney G, Zhong W, Tomanek D. Structural rigidity and low frequency vibrational modes of long carbon tubules. Zeitschrift für Physik D Atoms, Molecules and Clusters. 1993;27(1):93-6.
[29] Wong EW, Sheehan PE, Lieber CM. Nanobeam mechanics: elasticity, strength, and toughness of nanorods and nanotubes. Science. 1997;277(5334):1971-5.
[30] Yu M-F, Lourie O, Dyer MJ, Moloni K, Kelly TF, Ruoff RS. Strength and breaking mechanism of multiwalled carbon nanotubes under tensile load. Science. 2000;287(5453):637-40.
[31] Yu M-F, Files BS, Arepalli S, Ruoff RS. Tensile loading of ropes of single wall carbon nanotubes and their mechanical properties. Physical review letters. 2000;84(24):5552.
[32] Salvetat J-P, Kulik AJ, Bonard J-M, Briggs GAD, Stöckli T, Metenier K, et al. Elastic modulus of ordered and disordered multiwalled carbon nanotubes. Advanced Materials. 1999;11(2):161-5.
[33] Tong T, Zhao Y, Delzeit L, Kashani A, Meyyappan M, Majumdar A. Height independent compressive modulus of vertically aligned carbon nanotube arrays. Nano letters. 2008;8(2):511-5.

[34] Deck CP, Flowers J, McKee GSB, Vecchio K. Mechanical behavior of ultralong multiwalled carbon nanotube mats. Journal of Applied Physics. 2007;101(2):023512.
[35] Coleman JN, Khan U, Blau WJ, Gun'ko YK. Small but strong: A review of the mechanical properties of carbon nanotube–polymer composites. Carbon. 2006;44(9):1624-52.
[36] Dufresne A, Paillet M, Putaux J, Canet R, Carmona F, Delhaes P, et al. Processing and characterization of carbon nanotube/poly (styrene-co-butyl acrylate) nanocomposites. Journal of materials science. 2002;37(18):3915-23.
[37] Probst O, Moore EM, Resasco DE, Grady BP. Nucleation of polyvinyl alcohol crystallization by single-walled carbon nanotubes. Polymer. 2004;45(13):4437-43.
[38] Safadi B, Andrews R, Grulke E. Multiwalled carbon nanotube polymer composites: synthesis and characterization of thin films. Journal of applied polymer science. 2002;84(14):2660-9.
[39] Pötschke P, Bhattacharyya AR, Janke A, Goering H. Melt mixing of polycarbonate/multi-wall carbon nanotube composites. Composite Interfaces. 2003;10(4-5):389-404.
[40] Banerjee S, Hemraj-Benny T, Wong SS. Covalent surface chemistry of single-walled carbon nanotubes. Advanced Materials. 2005;17(1):17-29.
[41] Shaffer MS, Windle AH. Fabrication and characterization of carbon nanotube/poly (vinyl alcohol) composites. Advanced Materials. 1999;11(11):937-41.
[42] Qian D, Dickey EC, Andrews R, Rantell T. Load transfer and deformation mechanisms in carbon nanotube-polystyrene composites. Applied physics letters. 2000;76(20):2868-70.
[43] Gong X, Liu J, Baskaran S, Voise RD, Young JS. Surfactant-assisted processing of carbon nanotube/polymer composites. Chemistry of Materials. 2000;12(4):1049-52.
[44] Tai N-H, Yeh M-K, Liu J-H. Enhancement of the mechanical properties of carbon nanotube/phenolic composites using a carbon nanotube network as the reinforcement. Carbon. 2004;42(12):2774-7.
[45] Ogasawara T, Ishida Y, Ishikawa T, Yokota R. Characterization of multi-walled carbon nanotube/phenylethynyl terminated polyimide composites. Composites Part A: applied science and manufacturing. 2004;35(1):67-74.
[46] Frogley MD, Ravich D, Wagner HD. Mechanical properties of carbon nanoparticle-reinforced elastomers. Composites Science and technology. 2003;63(11):1647-54.
[47] Wang Z, Liang Z, Wang B, Zhang C, Kramer L. Processing and property investigation of single-walled carbon nanotube (SWNT) buckypaper/epoxy resin matrix nanocomposites. Composites Part A: applied science and manufacturing. 2004;35(10):1225-32.
[48] Coleman J, Blau W, Dalton A. EM noz, S. Collins, BG Kim, J. Razal, M. Selvidge, G. Vieiro, and RH Baughman. Appl Phys Lett. 2003;82:1682.

[49] Johnson RD BD, Richards CD, Richards RF, McClain D, Green D, Jiao J. Thermocompression bonding of vertically aligned carbon nanotube turfs to metalized substrates. Nanotechnology. 2009;20.
[50] Cao A, Veedu VP, Li X, Yao Z, Ghasemi-Nejhad MN, Ajayan PM. Multifunctional brushes made from carbon nanotubes. Nature materials. 2005;4(7):540-5.
[51] Y Zeng LC, BJ Carey, R Vajtai, PM Ajayan. Design and Reinforcement: Vertically Aligned Carbon Nanotube-Based Sandwich Composites. ACS Nano. 2010;4:6.
[52] Cao C, Reiner A, Chung C, Chang S-H, Kao I, Kukta RV, et al. Buckling initiation and displacement dependence in compression of vertically aligned carbon nanotube arrays. Carbon. 2011;49(10):3190-9.
[53] Zbib AA, Mesarovic S, Lilleodden ET, McClain D, Jiao J, Bahr DF. The coordinated buckling of carbon nanotube turfs under uniform compression. Nanotechnology. 2008;19(17):175704.
[54] Bradford PD, Wang X, Zhao H, Zhu YT. Tuning the compressive mechanical properties of carbon nanotube foam. Carbon. 2011;49(8):2834-41.
[55] Pathak S, Cambaz ZG, Kalidindi SR, Swadener JG, Gogotsi Y. Viscoelasticity and high buckling stress of dense carbon nanotube brushes. Carbon. 2009;47(8):1969-76.
[56] Hutchens SB, Hall LJ, Greer JR. In situ Mechanical Testing Reveals Periodic Buckle Nucleation and Propagation in Carbon Nanotube Bundles. Advanced Functional Materials. 2010;20(14):2338-46.
[57] Buehler MJ, Kong Y, Gao H. Deformation Mechanisms of Very Long Single-Wall Carbon Nanotubes Subject to Compressive Loading. Journal of Engineering Materials and Technology. 2004;126(3):245.
[58] Ru C. Effective bending stiffness of carbon nanotubes. Physical Review B. 2000;62(15):9973.
[59] Timoshenko SP, Gere JM. Theory of elastic stability: Courier Dover Publications; 2009.
[60] Wu J, Hwang K, Huang Y. An atomistic-based finite-deformation shell theory for single-wall carbon nanotubes. Journal of the Mechanics and Physics of Solids. 2008;56(1):279-92.
[61] Sears A, Batra R. Macroscopic properties of carbon nanotubes from molecular-mechanics simulations. Physical Review B. 2004;69(23):235406.
[62] Ru C. Column buckling of multiwalled carbon nanotubes with interlayer radial displacements. Physical Review B. 2000;62(24):16962.
[63] Ru C. Degraded axial buckling strain of multiwalled carbon nanotubes due to interlayer slips. Journal of Applied Physics. 2001;89(6):3426-33.
[64] Yakobson BI, Brabec C, Bernholc J. Nanomechanics of carbon tubes: instabilities beyond linear response. Physical review letters. 1996;76(14):2511.
[65] Qi HJ, Teo KBK, Lau KKS, Boyce MC, Milne WI, Robertson J, et al. Determination of mechanical properties of carbon nanotubes and vertically aligned

carbon nanotube forests using nanoindentation. Journal of the Mechanics and Physics of Solids. 2003;51(11-12):2213-37.
[66] Poggi MA, Boyles JS, Bottomley LA, McFarland AW, Colton JS, Nguyen CV, et al. Measuring the compression of a carbon nanospring. Nano Letters. 2004;4(6):1009-16.
[67] Falvo M, Clary G, Taylor R, Chi V, Brooks F, Washburn S, et al. Bending and buckling of carbon nanotubes under large strain. Nature. 1997;389(6651):582-4.
[68] Pogorelov EG, Zhbanov AI, Chang Y-C, Yang S. Universal curves for the van der waals interaction between single-walled carbon nanotubes. Langmuir : the ACS journal of surfaces and colloids. 2011;28(2):1276-82.
[69] Popescu A, Woods L, Bondarev I. Simple model of van der Waals interactions between two radially deformed single-wall carbon nanotubes. Physical Review B. 2008;77(11).
[70] Sun C-H, Lu G-Q, Cheng H-M. Simple approach to estimating the van der Waals interaction between carbon nanotubes. Physical Review B. 2006;73(19).
[71] Zhbanov AI, Pogorelov EG, Chang Y-C. Van der Waals interaction between two crossed carbon nanotubes. Acs Nano. 2010;4(10):5937-45.
[72] Gao C, Jin YZ, Kong H, Whitby RL, Acquah SF, Chen G, et al. Polyurea-functionalized multiwalled carbon nanotubes: synthesis, morphology, and Raman spectroscopy. The Journal of Physical Chemistry B. 2005;109(24):11925-32.
[73] Girifalco LA, Lad RA. Energy of Cohesion, Compressibility, and the Potential Energy Functions of the Graphite System. The Journal of Chemical Physics. 1956;25(4):693.
[74] Lourie O, Cox D, Wagner H. Buckling and collapse of embedded carbon nanotubes. Physical Review Letters. 1998;81(8):1638.
[75] Kim H, Chun K-Y, Choi J, Kim Y, Baik S. Effects of Catalyst on the Super-Growth of Multi-Walled Carbon Nanotubes. Journal of nanoscience and nanotechnology. 2010;10(5):3362-5.
[76] Kim SM, Pint CL, Amama PB, Zakharov DN, Hauge RH, Maruyama B, et al. Evolution in catalyst morphology leads to carbon nanotube growth termination. The Journal of Physical Chemistry Letters. 2010;1(6):918-22.
[77] Jaunky N, Knight Jr NF. An assessment of shell theories for buckling ofcircular cylindrical laminated composite panels loaded inaxial compression. International journal of solids and structures. 1999;36(25):3799-820.
[78] Karagiozova D, Jones N. Dynamic effects on buckling and energy absorption of cylindrical shells under axial impact. Thin-Walled Structures. 2001;39(7):583-610.
[79] Karagiozova D, Alves M, Jones N. Inertia effects in axisymmetrically deformed cylindrical shells under axial impact. International Journal of Impact Engineering. 2000;24(10):1083-115.
[80] Bisagni C. Numerical analysis and experimental correlation of composite shell buckling and post-buckling. Composites Part B: Engineering. 2000;31(8):655-67.
[81] Chai H. The post-buckling response of a bi-laterally constrained column. Journal of the Mechanics and Physics of Solids. 1998;46(7):1155-81.

[82] Pogorelov EG, Zhbanov AI, Chang YC, Yang S. Universal curves for the van der Waals interaction between single-walled carbon nanotubes. Langmuir : the ACS journal of surfaces and colloids. 2011;28(2):1276-82.
[83] Lourie O CD, and Wagner HD. Buckling and Collapse of Embedded Carbon Nanotubes. Phys Rev Lett. 1998;81:3.
[84] Ru CQ. Axially compressed buckling of a doublewalled carbon nanotube embedded in an elastic medium. Mechanics and Physics of Solids. 2001;49(6):14.
[85] Kitipornchai S, He XQ, Liew KM. Buckling analysis of triple-walled carbon nanotubes embedded in an elastic matrix. Journal of Applied Physics. 2005;97(11):114318.
[86] Cao A, Dickrell PL, Sawyer WG, Ghasemi-Nejhad MN, Ajayan PM. Super-compressible foamlike carbon nanotube films. Science. 2005;310(5752):1307-10.
[87] Zhang Q, Lu YC, Du F, Dai L, Baur J, Foster DC. Viscoelastic creep of vertically aligned carbon nanotubes. Journal of Physics D: Applied Physics. 2010;43(31):315401.
[88] Collins PG, Avouris P. Nanotubes for electronics. Scientific American. 2000;283(6):62-9.
[89] McCarter CM, Richards RF, Mesarovic SD, Richards CD, Bahr DF, McClain D, et al. Mechanical compliance of photolithographically defined vertically aligned carbon nanotube turf. Journal of Materials Science. 2006;41(23):7872-8.
[90] Mesarovic SD, McCarter CM, Bahr DF, Radhakrishnan H, Richards RF, Richards CD, et al. Mechanical behavior of a carbon nanotube turf. Scripta Materialia. 2007;56(2):157-60.
[91] Yaglioglu O, Cao A, Hart AJ, Martens R, Slocum A. Wide range control of microstructure and mechanical properties of carbon nanotube forests: a comparison between fixed and floating catalyst CVD techniques. Advanced Functional Materials. 2012;22(23):5028-37.
[92] Presser V, Heon M, Gogotsi Y. Carbide-Derived Carbons–From Porous Networks to Nanotubes and Graphene. Advanced Functional Materials. 2011;21(5):810-33.
[93] Bedewy M, Meshot ER, Guo H, Verploegen EA, Lu W, Hart AJ. Collective mechanism for the evolution and self-termination of vertically aligned carbon nanotube growth. The Journal of Physical Chemistry C. 2009;113(48):20576-82.
[94] Bedewy M, Meshot ER, Reinker MJ, Hart AJ. Population growth dynamics of carbon nanotubes. Acs Nano. 2011;5(11):8974-89.
[95] Hutchens SB, Needleman A, Greer JR. Analysis of uniaxial compression of vertically aligned carbon nanotubes. Journal of the Mechanics and Physics of Solids. 2011;59(10):2227-37.
[96] Åström J, Krasheninnikov A, Nordlund K. Carbon Nanotube Mats and Fibers with Irradiation-Improved Mechanical Characteristics: A Theoretical Model. Physical Review Letters. 2004;93(21).

[97] Antunes EF, Lobo AO, Corat EJ, Trava-Airoldi VJ, Martin AA, Ver ́ssimo C. Comparative study of first- and second-order Raman spectra of MWCNT at visible and infrared laser excitation. Carbon. 2006;44(11):2202-11.
[98] Antunes EF, Lobo AO, Corat EJ, Trava-Airoldi VJ. Influence of diameter in the Raman spectra of aligned multi-walled carbon nanotubes. Carbon. 2007;45(5):913-21.
[99] Attard MM, Hunt GW. Hyperelastic constitutive modeling under finite strain. International Journal of Solids and Structures. 2004;41(18-19):5327-50.
[100] Zheng F, Liang L, Gao Y, Sukamto JH, Aardahl CL. Carbon nanotube synthesis using mesoporous silica templates. Nano Letters. 2002;2(7):729-32.
[101] Ogden R. Large deformation isotropic elasticity-on the correlation of theory and experiment for incompressible rubberlike solids. Proceedings of the Royal Society of London A Mathematical and Physical Sciences. 1972;326(1567):565-84.
[102] Gendy A, Saleeb A. Nonlinear material parameter estimation for characterizing hyper elastic large strain models. Computational mechanics. 2000;25(1):66-77.
[103] Itskov M, Ehret A, Mavrilas D. A polyconvex anisotropic strain–energy function for soft collagenous tissues. Biomechanics and modeling in mechanobiology. 2006;5(1):17-26.
[104] Pathak S, Mohan N, Decolvenaere E, Needleman A, Bedewy M, Hart AJ, et al. Local relative density modulates failure and strength in vertically aligned carbon nanotubes. ACS nano. 2013;7(10):8593-604.
[105] Gibson LJ, Ashby MF, Harley BA. Cellular materials in nature and medicine: Cambridge University Press; 2010.
[106] Gibson LJ, Ashby MF. Cellular solids: structure and properties: Cambridge university press; 1999.
[107] Lourie O, Wagner H. Evaluation of Young's modulus of carbon nanotubes by micro-Raman spectroscopy. Journal of Materials Research. 1998;13(09):2418-22.
[108] Cooper C, Young R, Halsall M. Investigation into the deformation of carbon nanotubes and their composites through the use of Raman spectroscopy. Composites Part A: Applied Science and Manufacturing. 2001;32(3):401-11.
[109] Chou T-W, Gao L, Thostenson ET, Zhang Z, Byun J-H. An assessment of the science and technology of carbon nanotube-based fibers and composites. Composites Science and Technology. 2010;70(1):1-19.
[110] Thostenson ET, Ren Z, Chou T-W. Advances in the science and technology of carbon nanotubes and their composites: a review. Composites science and technology. 2001;61(13):1899-912.
[111] Schadler LS, Giannaris SC, Ajayan PM. Load transfer in carbon nanotube epoxy composites. Applied Physics Letters. 1998;73(26):3842.
[112] Ajayan PM, Schadler LS, Giannaris C, Rubio A. Single-walled carbon nanotube–polymer composites: strength and weakness. Advanced Materials. 2000;12(10):750-3.
[113] Ajayan PM, Tour JM. Materials science: nanotube composites. Nature. 2007;447(7148):1066-8.

[114] Ajayan P, Charlier J-C, Rinzler A. Carbon nanotubes: From macromolecules to nanotechnology. Proceedings of the National Academy of Sciences. 1999;96(25):14199-200.
[115] Zeng Y, Ci L, Carey BJ, Vajtai R, Ajayan PM. Design and reinforcement: vertically aligned carbon nanotube-based sandwich composites. ACS nano. 2010;4(11):6798-804.
[116] Carey BJ, Patra PK, Ci L, Silva GG, Ajayan PM. Observation of dynamic strain hardening in polymer nanocomposites. ACS nano. 2011;5(4):2715-22.
[117] Ma W, Liu L, Zhang Z, Yang R, Liu G, Zhang T, et al. High-strength composite fibers: realizing true potential of carbon nanotubes in polymer matrix through continuous reticulate architecture and molecular level couplings. Nano letters. 2009;9(8):2855-61.
[118] Suhr J, Koratkar N, Keblinski P, Ajayan P. Viscoelasticity in carbon nanotube composites. Nature materials. 2005;4(2):134-7.
[119] Lattanzi L, Raney JR, De Nardo L, Misra A, Daraio C. Nonlinear viscoelasticity of freestanding and polymer-anchored vertically aligned carbon nanotube foams. Journal of Applied Physics. 2012;111(7):074314.
[120] Nielsen LE. Mechanical properties of polymers: Van Nostrand Reinhold; 1962.
[121] Findley WN, Davis FA. Creep and relaxation of nonlinear viscoelastic materials: Courier Dover Publications; 2013.
[122] Ferry JD. Viscoelastic properties of polymers: John Wiley & Sons; 1980.
[123] 5.3 Dynamic mechanical properties https://moodle.fp.tul.cz/mod/page/view.php?id=11743.
[124] Physical Properties of Polymers. (n.d.). Retrieved from http://dspace.jorum.ac.uk/xmlui/bitstream/handle/10949/1033/Items/T838_1_section23.html.
[125] Hadid M, Rechak S, Tati A. Long-term bending creep behavior prediction of injection molded composite using stress–time correspondence principle. Materials Science and Engineering: A. 2004;385(1-2):54-8.
[126] Alonso B, Maquet J, Viana B. Hybrid organic-inorganic polydimethylsiloxane–vanadium–oxo materials crosslinked at the molecular level. New J Chem. 1998;22(9):935-9.
[127] Huang HH, Orler B, Wilkes GL. Structure-property behavior of new hybrid materials incorporating oligomeric species into sol-gel glasses. 3. Effect of acid content, tetraethoxysilane content, and molecular weight of poly (dimethylsiloxane). Macromolecules. 1987;20(6):1322-30.
[128] Huang H-H, Wilkes GL, Carlson JG. Structure-property behaviour of hybrid materials incorporating tetraethoxysilane with multifunctional poly (tetramethylene oxide). Polymer. 1989;30(11):2001-12.
[129] Brennan A, Wilkes G. Structure-property behaviour of sol-gel derived hybrid materials: effect of a polymeric acid catalyst. Polymer. 1991;32(4):733-9.

[130] Lötters J, Olthuis W, Veltink P, Bergveld P. The mechanical properties of the rubber elastic polymer polydimethylsiloxane for sensor applications. Journal of Micromechanics and Microengineering. 1997;7(3):145.
[131] Yakobson B, Smalley R. Fullerene Nanotubes: C 1,000,000 and Beyond Some unusual new molecules—long, hollow fibers with tantalizing electronic and mechanical properties—have joined diamonds and graphite in the carbon family. Am Scientist. 1997;85:324-37.
[132] Dresselhaus MS, Dresselhaus G, Eklund PC. Science of fullerenes and carbon nanotubes: their properties and applications: Academic press; 1996.
[133] Dekker C. Carbon nanotubes as molecular quantum wires. Physics today. 1999;52:22-30.
[134] Jin L, Bower C, Zhou O. Alignment of carbon nanotubes in a polymer matrix by mechanical stretching. Applied physics letters. 1998;73(9):1197-9.
[135] Xiong J, Zhou D, Zheng Z, Yang X, Wang X. Fabrication and distribution characteristics of polyurethane/single-walled carbon nanotube composite with anisotropic structure. Polymer. 2006;47(6):1763-6.
[136] Itskov M, Ehret AE, Mavrilas D. A polyconvex anisotropic strain-energy function for soft collagenous tissues. Biomechanics and modeling in mechanobiology. 2006;5(1):17-26.
[137] Sharda SC. A Strain Energy Density Function for Compressible Rubberlike Materials. Journal of Rheology. 1976;20(3):361.
[138] Yap HW, Lakes RS, Carpick RW. Mechanical instabilities of individual multiwalled carbon nanotubes under cyclic axial compression. Nano letters. 2007;7(5):1149-54.
[139] Enomoto K, Kitakata S, Yasuhara T, Ohtake N, Kuzumaki T, Mitsuda Y. Measurement of Young's modulus of carbon nanotubes by nanoprobe manipulation in a transmission electron microscope. Applied physics letters. 2006;88(15):153115.
[140] Lu JP. Elastic properties of carbon nanotubes and nanoropes. Physical Review Letters. 1997;79(7):1297.
[141] Misra A, Raney JR, De Nardo L, Craig AE, Daraio C. Synthesis and characterization of carbon nanotube–polymer multilayer structures. ACS nano. 2011;5(10):7713-21.
[142] Borca-Tasciuc T, Mazumder M, Son Y, Pal S, Schadler L, Ajayan P. Anisotropic thermal diffusivity characterization of aligned carbon nanotube-polymer composites. Journal of nanoscience and nanotechnology. 2007;7(4-5):1581-8.
[143] Thostenson ET, Li WZ, Wang DZ, Ren ZF, Chou TW. Carbon nanotube/carbon fiber hybrid multiscale composites. Journal of Applied Physics. 2002;91(9):6034.
[144] Ci L, Suhr J, Pushparaj V, Zhang X, Ajayan P. Continuous carbon nanotube reinforced composites. Nano letters. 2008;8(9):2762-6.
[145] Bortz DR, Weisenberger M, Marrs B, Andrews R. Fatigue performance of multiwall carbon nanotube composite PMMA and ABS. ASME 2008 International

Mechanical Engineering Congress and Exposition: American Society of Mechanical Engineers; p. 235-42.
[146] Grimmer CS, Dharan CKH. High-cycle fatigue of hybrid carbon nanotube/glass fiber/polymer composites. Journal of Materials Science. 2008;43(13):4487-92.
[147] Ren Y, Li F, Cheng H-M, Liao K. Tension–tension fatigue behavior of unidirectional single-walled carbon nanotube reinforced epoxy composite. Carbon. 2003;41(11):2177-9.
[148] Khan SU, Munir A, Hussain R, Kim J-K. Fatigue damage behaviors of carbon fiber-reinforced epoxy composites containing nanoclay. Composites Science and Technology. 2010;70(14):2077-85.
[149] Jones DS. Dynamic mechanical analysis of polymeric systems of pharmaceutical and biomedical significance. International journal of pharmaceutics. 1999;179(2):167-78.
[150] Chakravartula A, Komvopoulos K. Viscoelastic properties of polymer surfaces investigated by nanoscale dynamic mechanical analysis. Applied physics letters. 2006;88(13):131901--3.
[151] Shen Y, Golnaraghi F, Plumtree A. Modelling compressive cyclic stress–strain behaviour of structural foam. International Journal of Fatigue. 2001;23(6):491-7.
[152] Bergström J, Boyce M. Constitutive modeling of the large strain time-dependent behavior of elastomers. Journal of the Mechanics and Physics of Solids. 1998;46(5):931-54.
[153] Krzypow DJ, Rimnac CM. Cyclic steady state stress–strain behavior of UHMW polyethylene. Biomaterials. 2000;21(20):2081-7.
[154] Beatty MF, Krishnaswamy S. A theory of stress-softening in incompressible isotropic materials. Journal of the Mechanics and Physics of Solids. 2000;48(9):1931-65.
[155] Mullins L. Effect of stretching on the properties of rubber. Rubber Chemistry and Technology. 1948;21(2):281-300.
[156] Roland C. Network Recovery from Uniaxial Extension: II. The Origin of the Mullins Effect. Rubber chemistry and technology. 1989;62(5):880-95.
[157] Harwood J, Payne A. Stress softening in natural rubber vulcanizates. Part III. Carbon black-filled vulcanizates. Journal of Applied Polymer Science. 1966;10(2):315-24.
[158] Harwood J, Mullins L, Payne A. Stress softening in natural rubber vulcanizates. Part II. Stress softening effects in pure gum and filler loaded rubbers. Journal of Applied Polymer Science. 1965;9(9):3011-21.
[159] Lee MC, Williams MC. Application of a new structural theory to polymers. I. Uniaxial stress in crosslinked rubbers. Journal of Polymer Science: Polymer Physics Edition. 1985;23(11):2243-71.
[160] Govindjee S, Simo J. A micro-mechanically based continuum damage model for carbon black-filled rubbers incorporating Mullins' effect. Journal of the Mechanics and Physics of Solids. 1991;39(1):87-112.

[161] Anderson TL. Fracture mechanics: fundamentals and applications: CRC press; 2005.
[162] Reifsnider K, Talug A. Analysis of fatigue damage in composite laminates. International Journal of Fatigue. 1980;2(1):3-11.
[163] Wang S, Chim E-M. Fatigue damage and degradation in random short-fiber SMC composite. Journal of Composite Materials. 1983;17(2):114-34.
[164] Owen M, Howe R. The accumulation of damage in a glass-reinforced plastic under tensile and fatigue loading. Journal of Physics D: Applied Physics. 1972;5(9):1637.

# Appendix A

## COPYRIGHT & PERMISSION

Creative Commons

### Creative Commons License Deed

**Attribution-NonCommercial 3.0 Unported (CC BY-NC 3.0)**

This is a human-readable summary of (and not a substitute for) the license.
Disclaimer

**You are free to:**

**Share** — copy and redistribute the material in any medium or format

**Adapt** — remix, transform, and build upon the material

The licensor cannot revoke these freedoms as long as you follow the license terms.

**Under the following terms:**

**Attribution** — You must give appropriate credit, provide a link to the license, and indicate if changes were made. You may do so in any reasonable manner, but not in any way that suggests the licensor endorses you or your use.

**NonCommercial** — You may not use the material for commercial purposes.

**No additional restrictions** — You may not apply legal terms or technological measures that legally restrict others from doing anything the license permits.

**Notices:**

You do not have to comply with the license for elements of the material in the public domain or where your use is permitted by an applicable exception or limitation.

No warranties are given. The license may not give you all of the permissions necessary for your intended use. For example, other rights such as publicity, privacy, or moral rights may limit how you use the material.

This is a receipt to confirm that your permissions requests has been processed by PLSclear. A copy of your request appears below.

The publisher of the title will now correspond with you directly.

Please be aware that publishers do receive a large number of requests and processing them can be time consuming. Therefore response times can range between 1 and 12 weeks. If you do not hear from the publisher after 12 weeks, please contact plsclear@pls.org.uk quoting reference number (2516) and we will follow-up on your behalf.

Thank you for using PLSclear. If you have any feedback about the service, please contact PLS (plsclear@pls.org.uk)

---

## I am applying for permission for:

**NANOTECHNOLOGY** (09574484)

| | |
|---|---|
| A **article** extract | |
| year of publication: | **2015** |
| volume number: | **26** |
| title of article: | **Determination of material constants of vertically aligned carbon nanotube structures in compressions** |
| number of words: | **1000** |

---

## To be used in:

A **Book, Journal, Magazine or Academic Paper...**

| | |
|---|---|
| The **Thesis** details are | |
| type of document: | **Thesis** |
| publication title: | **MECHANICAL CHARACTERISTICS OF CONTINUOUS CARBON NANOTUBE AND CONTINUOUSLY REINFORCED CARBON NANOTUBE COMPOSITE** |

---